


Spring 2016

# Manufacturing polyacrylonitrile nanowires and nanofibers for sensing and energy storage applications

Juan Chen

Follow this and additional works at: <https://digitalcommons.latech.edu/dissertations>

 Part of the [Chemical Engineering Commons](#), and the [Nanoscience and Nanotechnology Commons](#)

---

**MANUFACTURING POLYACRYLONITRILE NANOWIRES  
AND NANOFIBERS FOR SENSING AND ENERGY  
STORAGE APPLICATIONS**

by

Juan Chen, B.S., M.S.

**A Dissertation Presented in Partial Fulfillment  
of the Requirements of the Degree  
Doctor of Philosophy**

**COLLEGE OF ENGINEERING AND SCIENCE  
LOUISIANA TECH UNIVERSITY**

**May 2016**

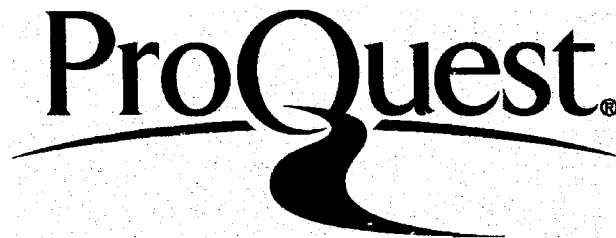
ProQuest Number: 10300723

All rights reserved

**INFORMATION TO ALL USERS**

The quality of this reproduction is dependent upon the quality of the copy submitted.

In the unlikely event that the author did not send a complete manuscript and there are missing pages, these will be noted. Also, if material had to be removed, a note will indicate the deletion.



ProQuest 10300723

Published by ProQuest LLC(2017). Copyright of the Dissertation is held by the Author.

All rights reserved.

This work is protected against unauthorized copying under Title 17, United States Code.  
Microform Edition © ProQuest LLC.

ProQuest LLC  
789 East Eisenhower Parkway  
P.O. Box 1346  
Ann Arbor, MI 48106-1346

LOUISIANA TECH UNIVERSITY

THE GRADUATE SCHOOL

FEBRUARY 18, 2016

Date

We hereby recommend that the thesis prepared under our supervision by  
Juan Chen, B.S., M.S.

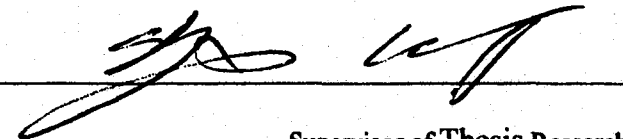
entitled MANUFACTURING POLYACRYLONITRILE NANOWIRES

AND NANOFIBERS FOR SENSING AND ENERGY

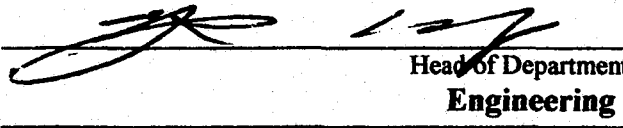
STORAGE APPLICATIONS

be accepted in partial fulfillment of the requirements for the Degree of

Doctor of Philosophy in Engineering



Supervisor of Thesis Research



Head of Department

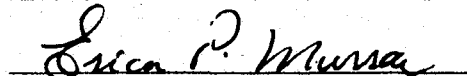
**Engineering**

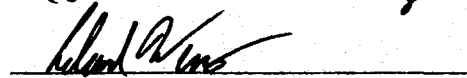
Department

Recommendation concurred in:



Prita Kamaichandran  
Yves LVO



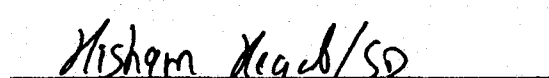


Advisory Committee

Approved:



Director of Graduate Studies



Dean of the College

Approved:



Dean of the Graduate School

## **ABSTRACT**

A novel flow guided assembly approach is presented to well align and accurately position nanowire arrays in pre-defined locations with high throughput and large scale manufacturing capability. In this approach, polyacrylonitrile (PAN)/N, N-dimethylformamide (DMF) solution is first filled in an array of microfluidic channels. Then a gas flow is introduced to blow out most solutions while pushing a little leftover against the channel wall to assemble into polymer nanowires. In this way, highly-ordered nanowires are conveniently aligned in the flow direction and patterned along both sides of the microchannels. In this study, we demonstrated this flow-guided assembly process by producing millimeter-long nanowires across 5 mm × 12 mm area in the same orientation and with basic “I-shape”, “T-shape”, and “cross” patterns. The assembled polymer nanowires were further converted to conductive carbon nanowires through a standard carbonization process. After integrated into electronic sensors, high sensitivity was found in model protein sensing tests. This new nanowire manufacturing approach is anticipated to open new doors to the fabrication of nanowire-based sensing systems and serve as the Good Manufacturing Practices (GMP) (a system for ensuring that products are consistently produced and controlled according to quality standards) for its simplicity, low cost, alignment reliability, and high throughput.

By using the same polymer solution (polyacrylonitrile (PAN)/N, N-dimethylformamide (DMF) solution), a new, simple, and low-cost method has been

developed in the production of porous composite nanofibers via a one-step foaming and electrospinning process. Sublimable aluminum acetylacetonate (AACA) was dissolved into polyacrylonitrile (PAN)/N, N-dimethylformamide (DMF) solution as the foaming agent. Silicon nanoparticles were then added and the resulting suspension solution was further electrospun to produce PAN/silicon composite nanofibers. The PAN nanofibers were then foamed during a thermal stabilization treatment and further carbonized into carbon/silicon composite nanofibers. Such mesoporous composites nanofiber mats were explored as the anode material for lithium ion batteries. Within this composite of nanofiber electrode, carbon nanofibers serve as the conductive media, while silicon nanoparticles ensure high lithium ion capacity and electrical density. The inter-fiber macrovoids and intra-fiber mesopores provide the buffering space to accommodate the huge volume expansion and consequent stress in the composite anode during the alloying process to mitigate electrode pulverization. Its high surface-to-volume ratio helps facilitate lithium ion transport between electrolytes and the active materials. Our electrochemical tests demonstrated higher reversible capacity and better capacity retention with this porous carbon/silicon composite nanofiber anode when compared with that made of nonporous composite nanofibers and CNF alone with similar treatments.

## APPROVAL FOR SCHOLARLY DISSEMINATION

The author grants to the Prescott Memorial Library of Louisiana Tech University the right to reproduce, by appropriate methods, upon request, any or all portions of this Dissertation. It is understood that "proper request" consists of the agreement, on the part of the requesting party, that said reproduction is for his personal use and that subsequent reproduction will not occur without written approval of the author of this Dissertation. Further, any portions of the Dissertation used in books, papers, and other works must be appropriately referenced to this Dissertation.

Finally, the author of this Dissertation reserves the right to publish freely, in the literature, at any time, any or all portions of this Dissertation.

Author Juan Hernandez

Date 04/25/16

## **DEDICATION**

**This dissertation is dedicated to my family who has supported me during the past seven years of living and study in US.**



## TABLE OF CONTENTS

|  |     |
|--|-----|
| ABSTRACT .....                                   | iii |
| DEDICATION.....                                  | vi  |
| LIST OF TABLES.....                              | x   |
| LIST OF FIGURES .....                            | xi  |
| ACKNOWLEDGMENTS .....                            | xiv |
| CHAPTER 1 INTRODUCTION.....                      | 1   |
| 1.1 Motivation .....                             | 1   |
| 1.2 Objective.....                               | 3   |
| 1.3 Outline .....                                | 4   |
| CHAPTER 2 LITERATURE REVIEW.....                 | 5   |
| 2.1 Current Status in Nanowire Sensor .....      | 5   |
| 2.1.1 Nanowires Synthetic Method .....           | 7   |
| 2.1.2 Nanowire Alignment Method.....             | 7   |
| 2.1.2.1 Blown Bubble Film Method.....            | 8   |
| 2.1.2.2 Contact Printing Methods.....            | 9   |
| 2.1.2.3 Differential Roll Printing (DRP) .....   | 9   |
| 2.1.2.4 Micro Contact Printing.....              | 10  |
| 2.1.2.5 Langmuir-Blodgett (LB) Assembly.....     | 12  |
| 2.1.3 Gas Blow/ Flow Guided Assembly .....       | 14  |
| 2.1.3.1 Alignment on Patterned Substrates.....   | 16  |
| 2.1.3.2 Self Assembly of 1D Nanostructures ..... | 18  |

|   |   |    |
|---|---|----|
| 2.1.3.3   | Solvent Evaporation Technique.....  | 20 |
| 2.2   | Current Status of Electrospun Anode Material for Lithium Ion Batteries..... | 24 |
| 2.2.1   | Principles of LIB.....  | 26 |
| 2.2.2   | New Anode Materials of LIB .....  | 27 |
| 2.2.2.1   | Carbon Based LIB Anode.....   | 29 |
| 2.2.2.2   | Si Nanowires Based Anode .....  | 30 |
| 2.2.2.3   | Si Nanoparticles Based Anode .....  | 32 |
| 2.2.2.4   | Core-shell Si NWs .....   | 32 |
| 2.2.2.5   | Hollow Si Nanostructures.....   | 33 |
| 2.2.2.6   | Hollow Si Nanostructure with Clamping .....                                 | 34 |
| 2.2.2.7   | Silicon/Carbon Nanofiber Composite Anode.....                               | 35 |
| 2.2.3   | Electrospinning.....  | 36 |
| 2.2.4   | Other Methods for Improving LIB Properties .....                            | 37 |
| 2.2.5   | Improve Electrochemical Performance by Adding Binder Materials .....        | 38 |
| CHAPTER 3 FLOW GUIDED ASSEMBLY CARBON NANOWIRE SENSOR ..... |   | 40 |
| 3.1   | Introduction .....  | 40 |
| 3.2   | Experiment Methods.....   | 42 |
| 3.2.1   | Chemicals.....  | 42 |
| 3.2.2   | Polymer Solution Preparation.....   | 42 |
| 3.2.3   | Microfluidic Channel Template Fabrication of PAN Nanowire .....             | 42 |
| 3.2.4   | Gas Blowing-based Flow-Guided Assembly Process .....                        | 44 |
| 3.2.5   | Carbon Nanowire Production by Carbonation .....                             | 45 |
| 3.2.6   | Carbon Nanowire Sensor Testing .....  | 45 |
| 3.3   | Results and Discussion .....  | 45 |
| 3.3.1   | Characterizations of Nanowires.....   | 45 |

|   |   |           |
|---|---|-----------|
| 3.3.2   | Characterization of Carbon Nanowires .....                      | 52        |
| 3.3.3   | I-V Characteristic/ Sensor/ Conductivity Test.....              | 55        |
| 3.3.4   | Characterization of “T” Shape and “Cross” Shape Nanowire.....   | 58        |
| 3.3.5   | Conclusions.....  | 63        |
| <b>CHAPTER 4 ELECTROSPINNING/FOAMING PRODUCTION OF POROUS SILICON/CARBON NANOFIBERS ANODE FOR LIB .....</b> |   | <b>64</b> |
| 4.1   | Introduction .....  | 64        |
| 4.2   | Experimental Methods.....                                       | 66        |
| 4.2.1   | Chemicals .....   | 66        |
| 4.2.2   | Materials Preparation.....                                      | 66        |
| 4.2.3   | Characterization.....   | 67        |
| 4.2.4   | Electrochemical Evaluation.....                                 | 67        |
| 4.3   | Results and Discussion.....                                     | 68        |
| 4.3.1   | Characterization of Porous C/Si/AACA Composites Nanofibers..... | 68        |
| 4.3.2   | Electrochemical Performance.....                                | 75        |
| 4.3.3   | Measurement at Different Current Density .....                  | 83        |
| 4.4   | Conclusions .....   | 86        |
| <b>CHAPTER 5 CONCLUSIONS AND FUTURE WORK.....</b>   |   | <b>87</b> |
| 5.1   | Conclusions .....   | 87        |
| 5.2   | Future Work.....  | 88        |
| <b>BIBLIOGRAPHY.....</b>  |   | <b>91</b> |

## LIST OF TABLES

|   |           |
|---|-----------|
| <b>Table 4-1: The surface and pore structure parameters of porous C/Si/AACA composite nanofibers, nonporous C/Si composite nanofibers and pure CNF.....</b> | <b>72</b> |
|---|-----------|

## LIST OF FIGURES

|   |    |
|---|----|
| <b>Figure 2-1:</b> Schematic showing the alignment of nanomaterials using the blown bubble film method [27].  | 8  |
| <b>Figure 2-2:</b> Schematic of LB assembly [21].   | 13 |
| <b>Figure 2-3:</b> Schematic diagram of a conventional Li ion battery.  | 27 |
| <b>Figure 2-4:</b> Si electrode failure mechanisms: (a) material pulverization. (b) Morphology and volume change of the entire Si electrode.(c) Continuous SEI growth.  | 34 |
| <b>Figure 3-1:</b> Schematic of flow-guided assembly of polymer nanowire arrays via a microchannel-array template: (i) attach a PDMS microchannel template on a Si wafer; (ii) fill microchannels with a polymer solution; (iii) introduce a gas flow to blow away the most polymer solution in microchannels; (iv) dry up microchannels via continuously blowing; (v) remove the PDMS template to release polymer nanowires on the Si wafer. | 41 |
| <b>Figure 3-2:</b> Microchannel pattern design.   | 43 |
| <b>Figure 3-3:</b> An optical microscopy image of the fabricated micropatterns on a silicon wafer.  | 43 |
| <b>Figure 3-4:</b> SEM images of PDMS template with microchannel arrays.  | 44 |
| <b>Figure 3-5:</b> SEM image of the produced PAN nanowires on Si substrate.   | 46 |
| <b>Figure 3-6:</b> SEM image of the sharp end of PAN nanowires assembled with 2wt% PAN/DMF solution.  | 47 |
| <b>Figure 3-7a:</b> The assembly quality of nanowires with PAN solutions of various concentration: 0.1%, The N <sub>2</sub> gas flow was fixed at ~1.0 ml/h.  | 48 |
| <b>Figure 3-7b:</b> The assembly quality of nanowires with PAN solutions of various concentration: 0.5 %, The N <sub>2</sub> gas flow was fixed at ~1.0mh/h.  | 50 |

|   |    |
|---|----|
| <b>Figure 3-7c:</b> The assembly quality of nanowires with PAN solutions of various concentration: 1 %, The N <sub>2</sub> gas flow was fixed at ~1.0ml/h.....  | 51 |
| <b>Figure 3-7d:</b> The assembly quality of nanowires with PAN solutions of various concentration: 10 %, The N <sub>2</sub> gas flow was fixed at ~1.0ml/h.....   | 51 |
| <b>Figure 3-8:</b> (a) An AFM image of PAN nanowires on a Si wafer produced with 2.0 wt% solid content; (b) The height of PAN nanowires produced with various PAN solution concentrations.....                            | 41 |
| <b>Figure 3-9:</b> (a) A typical PAN carbonization procedure and involved structure evolution; (b) SEM image of carbon nanowires after single assembly.....   | 55 |
| <b>Figure 3-10:</b> AFM images of PAN after single-assembly.....  | 56 |
| <b>Figure 3-11:</b> AFM images of carbon nanowires after double assembly process.....   | 56 |
| <b>Figure 3-12:</b> The height shrinking percentage of nanowires before and after carbonization.....  | 57 |
| <b>Figure 3-13:</b> Schematic of the sensor integrated with the assembled carbon nanowires.....   | 58 |
| <b>Figure 3-14:</b> The conductance measurement of the produced nanowire sensors when adding BSA solutions of various concentrations.....   | 59 |
| <b>Figure 3-15:</b> The relationship of the conductance difference of nanowire sensor to the BSA concentration. A total of 35 nanowires patterned in parallel between two terminal electrodes were used in the tests..... | 59 |
| <b>Figure 3-16:</b> Schematic of double flow-guided assembly.....   | 61 |
| <b>Figure 3-17:</b> SEM images of produced polymer nanowires: “T” shape.....  | 62 |
| <b>Figure 3-18:</b> SEM images of produced polymer nanowires “cross” shape.....   | 63 |
| <b>Figure 3-19:</b> SEM images of (a) the cross-section of PDMS negative replica of a PAN nanowire; (b) intersection of cross nanowires.....  | 62 |
| <b>Figure 4-1:</b> Schematic of the one-step foaming/electrospinning process in the manufacture of mesoporous C/Si/AACA composite nanofiber.....  | 65 |
| <b>Figure 4-2:</b> Optical images of the C/Si/AACA composite nanofibers under mechanical deformation (folding and spiral-wound bending) and after bending.....  | 68 |

- Figure 4-3:** The SEM morphologies of porous C/Si/AACA composite nanofibers (a and b), nonporous C/Si composite nanofibers (c and d), pure CNFs (e and f), and PAN/Si/AACA composite nanofibers after the stabilization step (g and h) .....72
- Figure 4-4:** TGA results of PAN/Si/AACA composite nanofibers, nonporous PAN/Si/AACA composite nanofibers, and pure PAN nanofibers .....73
- Figure 4-5:** (a) XRD patterns of C/Si/AACA composite nanofibers along with nonporous C/Si composite nanofibers and pure CNFs; (b) EDS of porous C/Si/AACA composite nanofibers .....76
- Figure 4-6a:** The voltage profiles for the 1st, 2nd, 10th, and 20th galvanostatic charge–discharge cycles of porous C/Si/AACA composite nanofibers .....79
- Figure 4-6b:** The voltage profiles for the 1st, 2nd, 10th, and 20th galvanostatic charge–discharge cycles of nonporous C/Si composite nanofibers.....79
- Figure 4-6c:** The voltage profiles for the 1st, 2nd, 10th, and 20th galvanostatic charge–discharge cycles of porous pure CNFs.....80
- Figure 4-7:** (a) The cycling performances of porous C/Si/AACA composite nanofibers, nonporous C/Si composite nanofibers, and pure CNFs. (b) The Coulombic efficiency of porous C/Si/AACA composite nanofibers, nonporous C/Si composite nanofibers, and pure CNFs.....82
- Figure 4-8:** Accommodation mechanism of volume expansion and stress induction during Li ion insertion using incorporated mesopores .....84
- Figure 4-9:** (a) Voltage profiles for anodes made by composites nanofibers (C/Si/AACA nanofibers) at different current density; (b) The cycling performance of LIBs made of these nanofibers at different current density.....87

## ACKNOWLEDGMENTS

I cannot express enough thanks to my advisor Dr. Shengnian Wang for his continued support and encouragement. I sincerely appreciated the opportunities he provided.

Dr. Yuri Lvov, Dr. B. Ramu Ramachandran, Dr. Leland Weiss and Dr. Erica Murray, thank you for being my committee members. I am grateful for the time, suggestions, and positive comments you provided.

My completion of this project could not have been accomplished without the support of my group members, especially Dr. Yingbo Zu and Dr. Yuxin Wang. Thank you for the helpful discussion and advice on my research study. As a group member who is also my dearest friend, Dr. Shuyan Huang's encouragement and emotional support during the tough days are very much appreciated.

Dr. Fan Gao, thank you for taking time to provide those professional comments on my dissertation. I always appreciate our friendship for the past decades. As my only family members here in US, Uncle Tim and Aunt Helen, thank you for your care and help during those hard times.

At the end, thanks to my parents as well, Mr. and Mrs. Chen, my deepest gratitude for the unconditional love and care from you. Thank you for supporting me in my pursuit of my Ph.D.



# **CHAPTER 1**

## **INTRODUCTION**

### **1.1 Motivation**

As one-dimensional nanostructure, nanowires have been widely applied in chemical and biological sensing systems. To attain ultrahigh sensitivity, nanowire-based electronic sensors require nanowires to be aligned in parallel and well-patterned at the desired locations on the substrate where they stay. There have been many ways to improve the synthesis of the nanowires. Those direct synthesis approaches have advantages like low cost and high yield, but they suffer with dimension heterogeneity issue. Great improvements have been achieved on the dimension control of nanowires during their synthesis by utilizing some templates. However, the randomly orientated nanowire after removing the template easily leads to serious crosstalk issues when integrated into the sensors.

Various methods have been developed in the past decade to overcome such random alignment issues by assembling post-growth nanowires, while not yet convenient for their integration to a large scale manufacturing process. Therefore, one major task of my dissertation is to focus on developing new ways on the fabrication, alignment, patterning, integration, and manufacturing of polymer nanowires and eventually convert them into conductive carbon nanowires for sensing applications. Polymers are chosen as

the nanowire sensor materials because they are easy to integrate with both top-down and bottom-up fabrication processes, flexibility on altering surface physical and chemical properties, feasibility on becoming conductive (e.g., carbonization) or semi-conductive (e.g., hybrid conductive polymer). Polymer derivative carbon nanowires are favored in this project due to their excellent chemical and electrochemical stability when used in electrochemical sensors [1].

For the same reason, these polymer materials are also explored to their potential application as electrode materials in lithium ion batteries (LIBs). LIBs have been widely applied in powerful energy storage applications and tremendous efforts have been done on the search of appropriate anode materials for LIBs in the past decade. On the one hand, the current commonly used carbon-based anode of LIBs showed excellent stability, ductility, and conductivity, though only limited lithium storage capacity. On the other hand, some semi-conductive materials, silicon (Si) in particular, show ultrahigh theoretical lithium capacity, while their adoption is quite restricted due to their low conductivity and serious volume change issues during lithiation and delithiation. The adoption of Si/carbon composites naturally becomes the solution for their potential heritage of merits from both carbon and Si based materials. Adding carbon and/or introducing a porous structure have been adopted in composite anode to improve their electrochemical performance.

As a low cost and high throughput process in the production of carbon nanofibers (CNFs), electrospinning has also been adopted to provide the necessary carbon source for high conductivity and serve as a three-dimensional current collector. Some porous CNFs were produced by introducing pore generation agents, which require further removal by

wet etching process or extraction of some immiscible phase from the framework of CNFs. The demand for relatively cheap and scalable manufacturing processes to produce porous silicon/CNFs composites anode is still very challenging.

## 1.2 Objective

Based on past work, our group developed a new flow guided assembly approach to help align and position DNA nanowires on pre-defined micropatterns and locations, the same method are used here to synthesize, align, and pattern polymer nanowires in a reliable and efficient manner with a high throughput. Specifically, we combine this flow guided assembly approach with a gas blowing process to help align and pattern (polyacrylonitrile or PAN, one widely used polymer in the production of carbon fibers) along the walls of the microfluidic channels on both sides on a PDMS template. Our objective is to demonstrate this low-cost, scalable manufacturing approach in the production of nanowire-based sensors with well-patterned nanowire arrays for ultrahigh sensitivity.

Working with the same polymer solution (i.e., PAN), we also try to produce mesoporous C/Si composite nanofibers by first electrospinning to form PAN/silicon composite nanofibers. Aluminum acetylacetonate ( $\text{Al}(\text{C}_5\text{H}_7\text{O}_2)_3$ , AACA) is chosen to be the foaming agent which can be dissolved in the PAN solution, which is eventually sublimated to produce mesoporous composite nanofibers. The PAN nanofibers are then carbonized to obtain C/Si fibrous composites and used as LIBs anode to achieve high energy density and good cycling performance.

### 1.3 Outline

Chapter 1 is the introduction of this dissertation, including the motivation and objectives of the research work done in the past four years. The subject and content of each chapter has also been discussed.

Chapter 2 is a literature review of the pioneering research work. It covers two areas. One is the different fabricating process for nanowire based sensing system; the other is the development of new material and methods used for LIB anode.

Chapter 3 is the description of the project: “Manufacturing a nanowire-based sensing system via flow-guided assembly in a microchannel array template”; the steps of the experiment and the results of characterization and measurement were discussed and concluded.

Chapter 4 is the description of the project of “Foamed mesoporous carbon/silicon composite nanofiber anode for lithium ion batteries.” The steps of the experiment, results of characterization, and measurement were discussed and concluded.

Chapter 5 is a conclusion of the whole dissertation and some future work of this research was suggested to be continued.

## **CHAPTER 2**

### **LITERATURE REVIEW**

#### **2.1 Current Status in Nanowire Sensor**

Characterized by the small lateral size, high surface-to-volume ratio, and tuneable quantum confinement effect, nanowires made of metal, semiconductor, or conductive polymers hold tremendous potentials to build next-generation sensors, electronics, and optoelectronics [2-4]. They serve as interconnections or junctions on chemo-resistors, field-effect transistors (FETs) [5-7], or thermoelectronic devices (thermocouples or diodes) [8, 9] to enable rapid, real-time, and label-free monitoring of chemical [10] or biological molecules (e.g., DNA, proteins, virus, and pathogens) [11-13] with direct electrical readout. Compared to the thin film based planar counterparts, nanowire-based electronic sensing systems better define the accumulation or depletion of charge carriers to attain ultrahigh sensitivity [14].

However, their wide adoption is still seriously impeded by the lacking of low-cost ways on the fabrication, alignment, patterning, integration, and manufacturing of nanowires. The available direct synthesis approaches are versatile, low cost, and have high yield, but frequently suffer large variations on the dimensions and crystalline of synthesized nanowires [15, 16]. With the aid of nanoporous templates (e.g., anodic aluminium oxide membrane or AAO), great improvements have been achieved on the

dimension control of nanowires during their synthesis [17-19]. However their natural nest morphology between electronic contacts leads to serious crosstalk issues when integrated into the sensors, keeping them away from the anticipated superior sensitivity [20].

To overcome the random alignment issues in assembling post-growth nanowires, various methods have been developed in the past decade, including Langmuir-blodgett assembly [21], contact printing [22], electric or magnetic field assisted assembly [23-25], fluid flow [26-28], and nanocombing [29-32]. With these approaches, nanocombing and contact printing approaches in particular, high density, individually connected nanowire arrays were successfully aligned with a misalignment ratio as low as 1-5%. Some alignment variations and crossing defects, however, still exist, preventing their qualification to single-nanowire sensing applications. Moreover, as the synthesis and alignment of nanowires in these approaches were done in two separate processes, it is not yet convenient for their integration with the fabrication and manufacturing processes adopted in electronic sensor industry.

One dimensional nanostructure like nanotubes, nanorods, and nanowires has been widely applied in chemical and biological sensing area, which covers electronic device (e.g. LEDs, diodes and transistors), optical device (e.g. photon driven nanowire laser and photodetectors), data storage, and energy conversion. To get better properties on these devices, the nanowires have to be aligned or oriented on substrates when they are applied [33].

Orientation of these nanostructure alignments on the substrate could be either parallel or perpendicular. There are two methods to get the certain orientation: (1)

growing nanostructures onto the substrate oriented parallels or perpendicularly; (2) aligning the as-fabricated nanostructures on the substrates [34].

### 2.1.1 Nanowires Synthetic Method

When it comes to growing nanostructure onto the substrate, there are the template-assisted method and the template-free method. Template assisted growth works through electrodeposition into the pore of the anodic alumina membrane or polycarbonate membrane as hard templates. Besides anodic alumina and polycarbonate as the template, there are several soft templates such as mesoporous silica, surfactant liquid crystals, block copolymers and organic gels were used to synthesis NWs. In addition, bio cellulose, biomolecules such as DNA, viruses and bacteria could be used as templates, too. In addition to the template-assisted method, template-free methods include chemical vapor deposition, hydrothermal and seeded solution growth methods [34].

There are many techniques for orienting prefabricated 1D nanostructure, such as the use of electric field, magnetic field, blown bubble films, roll printing, contact printing, Langmuir-Blodgett (LB) and biomolecule assisted assembly.

### 2.1.2 Nanowire Alignment Method

#### 2.1.2.1 *Blown Bubble Films Method*

Lieber *et al.* firstly demonstrated the blown bubble films to align the nanowires and nanotubes. The process started by preparing the polymer solution containing the nanomaterial, then added it to a die and expanded to form a bubble. This happened at a controlled pressure and the expansion rate with a stable upward external vertical force by using a ring which rises the rising bubble and keeps the bubble centered over the die.

Schematic of alignment of nanomaterials using the blown bubble film method is shown in Figure 2-1.

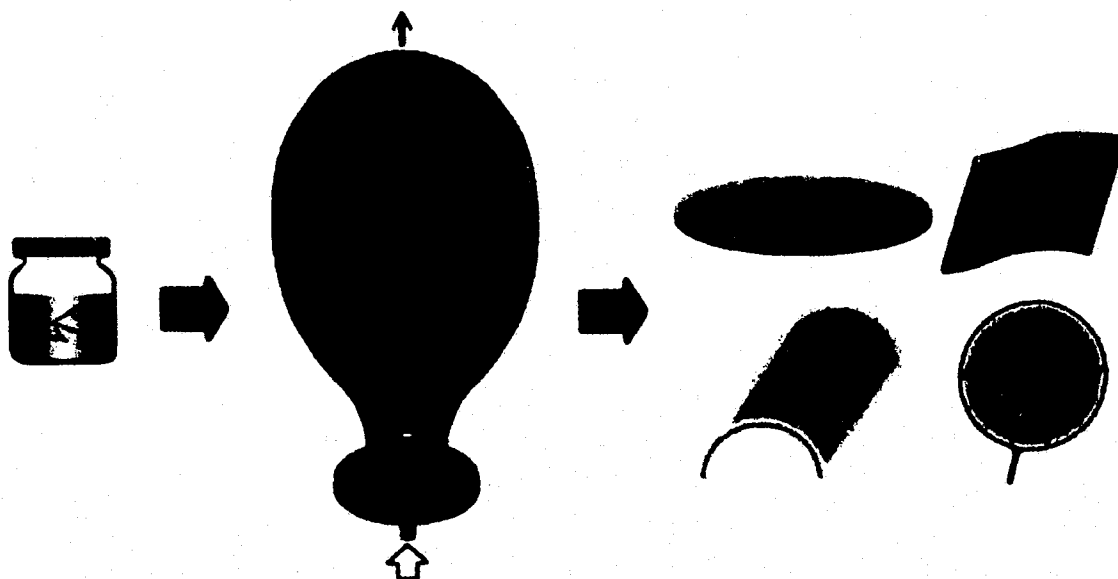


**Figure 2-1:** Schematic showing the alignment of nanomaterials using the blown bubble film method [27].

The final step to get an array of well aligned nanomaterials is transferring the bubble to the substrates. Arrays of silicon nanowires (SiNWs), single and multi-walled carbon nanotubes (SWNTs and MWNTs) and CdS nanowires (CdS NWs) were generated on silicon wafers varying in diameter from 75-200 mm. The application of well aligned Si NWs was demonstrated in making a Si NW field effect transistor (Si NW FET) [27]. The authors put forward the idea of aligning a variety of nanomaterials on a substrate by incorporating different polymers and nanomaterials into the bubble. The parameters could be optimized to align the nanomaterial on the substrates of different sizes and morphologies [35].



### 2.1.2.2 Contact Printing Methods

Contact printing methods have been used to align the nanowires on the substrates by printing patterns of chemical inks on the substrates (receiver) with a high resolution rubber stamp (donor) such as poly (dimethylsiloxane) (PDMS). This method can be applied with the varieties of substrates and inks, only if the ink has a higher affinity for the substrate than compared to the stamp. Generally, self-assembled monolayers (SAM) are produced using these methods. This method can achieve nanometer scale resolutions and generate large arrays of patterned surfaces. Both of the curved surfaces and flat stamp to align the nanowires by a roll printing procedure to generate patterns of 1D nanostructure have been investigated. The use of stamps of varying geometries has been demonstrated such as rolling cylindrical optical fibers over the inked stamp as rollers to print patterns on curved surfaces. They are the advantages of photolithography techniques that are capable of generating uniform patterns on curved surfaces and coating non-flat surfaces with uniform films of photoresists [36].

### 2.1.2.3 Differential Roll Printing (DRP)

Javey *et al.* have aligned GeNWs on a silicon substrate to fabricate FET device which delivered 700  $\mu\text{A}$  of a current for a parallel array of 700 nanowires [37] by using differential roll printing (DRP) method. Firstly, by using the vapor-liquid-solid process to grow nanowires on quartz or a glass tube, then the tube was attached to the rollers to transfer and align the nanowires on the substrate. Both the rolling velocity and the pressure applied from the roller to the receiver substrate both affect the quality of printing.

This method has been demonstrated to produce 30 inch graphene films for transparent electrodes which were incorporated into a fully functional touch screen panel

device. Generally, the chemical vapor deposition method was used to grow graphene films on copper substrates and then transferred to a polymer substrate by roll-to-roll printing, which can also be used to transfer the graphene film to the target substrate [38].

DRP method is beneficial for accomplishing printing on large substrates which only a small tangential area was in contact between the roller and the substrate [37].

#### 2.1.2.4 Micro Contact Printing

Javey *et al.* have assembled Ge nanowires (GeNWs) on a patterned substrate by micro contact printing. The quality of nanowire alignment can be affected by modifying the patterned substrate surface with various chemical compounds [8]. The printing method has been demonstrated to generate two-dimensional or crossed patterns. Firstly, a layer of PMMA resist was coated on the receiver substrate after the first printing, and before the second printing. Then mild O<sub>2</sub> plasma was used to etch away the PMMA layer. This printing method was able to selectively align the nanowires on patterned arrays of lines on a substrate for fabricating the FET device. A Schottky diode could be successfully fabricated on a flexible plastic substrate by using this printing method. In a further work, the group has used the contact printing method to fabricate CdSe nanowires which performed as photodetector and the Ge/Si nanowires performed as the transistor operations [39]. Both of these nanowires are assembled at their respective locations. There are studies on fabricating both single and parallel arrays of nanowires and observing the performance of the device [40].

Kim *et al.* have used patterned hydrophobic and hydrophilic stamps to generate V<sub>2</sub>O<sub>5</sub> nanowire patterns on (3-Aminopropyl) triethoxysilane (APTES) coated silicon substrate by micro-contact printing. The authors reported that the width of the nanowire

related to both the width of the recess areas and concentration of the nanowire solution. It was found that the width of the nanowire was equal to the pattern size in the case of hydrophilic stamps which the transfer occurred from the relief patterns. Further study observed less entanglement among the nanowires. The length of the nanowires was found to be equal to or smaller than the pattern size. The authors stated that this could happen before the contact printing. Air blowing removed those longer nanowires which were weakly attached to the stamp. In a further work, they have aligned the nanowires on APTES coated silicon substrates and bare silicon substrates by using micro-contact printing, and the nanowires were transferred by the edge transfer mechanism described in [41].

They also accomplished direct alignment from a solution of  $V_2O_5$  nanowires on the silicon substrate coated with APTES/octadecyltrichlorosilane (OTS) patterns. The results showed that the nanowires aggregated and only a single wire was observed, and the lengths of the nanowires were much shorter than they were in the solution [42].

Hannon *et al.* have aligned SWCNTs on  $HfO_2$  and  $Al_2O_3$  coated substrates by utilizing micro-contact printing followed by lithography and plasma [43]. Ahn *et al.* also used micro-contact printing to fabricate FETs device, thin film transistors (TFTs) and high electron mobility transistors (HEMTs) by assembling parallel, crossed and multilayer arrays of nanowires on polyimide substrates. The method of micro-contact printing was also be applied in transferring the nanowires of GaN, GaAs, Si, and SWNTs, which were grown from one substrate to the substrate of the device. In this case, the result of transferring SWNTs and GaAs nanowires was greater than 99%, whereas the yield was low for GaN and Si nanowires which was due to fracture and impartial transfer

[44]. In a study that Ge/Si nanowires were transferred from the growth substrate to the device substrate by micro-contact printing [45].

There are studies where multilayers of nanowires were obtained by repeating the printing procedure [45]. Javey *et al.* have aligned single and multilayers of Ge/Si nanowires to generate 3D arrays of nanowires. Ahn *et al.* achieved only 3 layers of nanowires. Up to 10 vertical layers of nanowires could be generated which improved the previous work [44].

#### 2.1.2.5 Langmuir-Blodgett (LB) Assembly

The LB method is a simple and robust technique which has been used to assemble the nanowires. The method starts with dispersing nanowires and surfactant in a LB trough to form a uniform monolayer nanowire film, followed by a computer controlled device to compress the monolayer and align the nanowires. The compression pressure could affect the density of the aligned nanowires. When dipping the substrate into the LB trough, the nanowires can be transferred to a planar substrate. The alignment of nanowires on the water-surfactant interface is used to transfer timber felled from the woods to the mills in North America [46].

Tao *et al.* have used the LB assembly to align poly (vinyl pyrrolidone) capped silver nanowires and used surface enhanced Raman spectroscopy for molecular sensing applications, the aligned nanowires exhibited large electromagnetic field enhancement [21]. The schematic of LB assembly is shown in Figure 2-2.

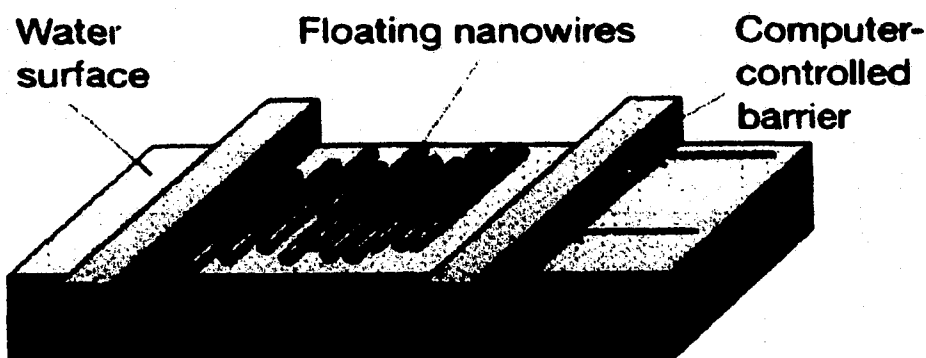


**Figure 2-2:** Schematic of LB assembly [21].

The Lieber group has used the LB method to assemble the nanowires in micrometer to centimeter scale. They used 1-octadecylamine as surfactant to assemble Si/SiO<sub>2</sub> core/shell nanowires suspended in organic solvents. The photolithography process well defined arrays were fabricated and used in nanoelectronic devices application. Furthermore, they fabricated a uniform coverage of crossed nanowires over a centimeter length scale by transferring the aligned nanowires in orthogonal directions and then repeated the patterning process [47]. In addition, fabrication of single silicon nanowire (Si NW) arrays using the LB method was achieved and the electrodes were defined by the microfabrication procedure. The device performed high reproducibility with different batches of nanowire arrays [48].

Dai *et al.* used chemical vapor deposition to synthesize Ge nanowires (GeNWs) on silica which was deposited with gold nanoparticles and modified by APTES. After then, the GeNWs were assembled by using the LB method [49]. The SWCNTs were aligned by the LB method to fabricate the devices, which CNT was used as the insulator rather than silicon [50]. Park *et al.* have aligned V<sub>2</sub>O<sub>5</sub> nanowires by the LB method, following with micro-contact printing ( $\mu$ CP). By using dioctadecyldimethylammonium

bromide (DODAB) surfactant, a nanowire film was formed in the water by LB compression. The NW film was transferred to a patterned PDMS stamp by using the Langmuir-Schaefer arm. The  $\mu$ CP was used to transfer  $V_2O_5$  nanowires onto the APTES modified  $SiO_2$  substrate. The  $V_2O_5$  nanowires films were also transferred to hydrophobic polycarbonate substrates easily by using  $\mu$ CP [51].

Kim *et al.* have studied the assembling of  $BaCrO_4$  nanorods and forming isotropic distribution of the nanowires in a monolayer at a low pressure and observing 2D nematic, 2D smectic, and 3D nematic liquid crystal phases at high pressure [52]. In addition, the group also demonstrated the LB assembly to form parallel 2D structure of the  $BaWO_4$  nanorods with a separation of 1-2 nm between individual nanowires.

### 2.1.3 Gas Blow/ Flow Guided Assembly

#### 2.1.3.1 Flow Guided Alignment

The flow of liquids and gases in the channels are used to align nanomaterials in the direction of the flow. Huang *et al.* have used fluid flow in PDMS microchannels which were coated with amine terminated monolayer to align GaP, InP and Si nanowires with rapid and strong attachments. Nanowires could be aligned to form crossed and triangular architectures by changing the flow direction. Multi-layers of nanowires can be formed by layer-by-layer assembly. By changing the solution concentration, the speed of the fluid flow and duration of the flow can control the average separation between the nanowires. The length of the aligned nanowires could be controlled from nanometer to micrometer scale with several square millimeters covering [26].

Messer *et al.* have utilized fluid flow to align the nanowires within the microfluidic channel by capillary force. They use this method to generate configurations

of parallel, crossed and multilayered  $[\text{Mo}_3\text{Se}_3]_\infty$  NWs on PDMS microchannels[53].

Wang *et al.* used flow-fluid method to align Ge nanowires which were synthesized by low pressure CVD (LPCVD). One end of the nanowires was fixed at the point of growth on the substrate and then used the flow of DI water to align the nanowires along the flow direction [54].

Xin and Woolley have aligned SWCNTs on poly-L-lysine coated silicon surface by flowing Ar gas in the direction of an 8 mm length of the substrate and forming crossed arrays in the perpendicular direction. During the Ar gas blowing, the droplet of the nanowire did not move but underwent a combination of recirculation, clockwise and counter-clockwise rotations while the silicon surface was placed at  $20^\circ$  horizontally. SWCNT alignment could not be observed on bare silicon or flow rates below 6 cm/s [55].

Meitl *et al.* have used the controlled flocculation method to align the SWCNTs on rotating the substrate. The surfactant coated SWCNTs were mixed with methanol, which has a high affinity for surfactant and easy releasing the nanotubes from the surfactant. Then the aligned nanotubes were transferred to various substrates such as APTES coated silicon or glass, untreated silicon, mica (APTES treated and untreated), Au, PDMS, PMMA, indium tin oxide (ITO) and polyimide with good coverage of nanotubes. The density of the nanotubes on the substrate was poor without methanol. Whether the nanotubes contacting each other or not before being deposited on the substrate decides they form bundles or as individual tubes after aligned in the radial direction on the substrate. Heating the substrate to  $65^\circ\text{C}$  could enhance the transfer. The resistivity of this aligned SWCNTs based TFT device in the direction of alignment of nanotubes was three times lower than in the direction perpendicular to the alignment [56].

### 2.1.3.1 Alignment on Patterned Substrates

The methods have been used to align different 1D nanostructured nanowires and nanotubes on patterned regions of substrates with varying properties and affinity and different functional groups.

Myung *et al.* have aligned  $V_2O_5$  nanowires and SWCNTs on gold substrates which are modified by self-assembled monolayers (SAM) with gradient molecular density, called “lens” effect. The patterns on the substrate guide the nanowires and align them at the center of the patterns, just like a lens guides the light to the center. Micro-contact printing was conducted to generate SAMs of amine treated cysteamine and 1-octadecanethiol (ODT) on a gold substrate. ODT patterns with gradient density can be generated by printing with longer contact times. Cysteamine SAM with gradient molecular density can be reached by printing cysteamine to fill the gradients. Both the nanowires and CNTs were attracted to the regions of positively charged amine regions and aligned at the centre of the mixed patterns with a higher density of cysteamine [57].

In contrast, due to Van der Waals interactions Mirkin and co-workers observed that the tubes and the  $-COOH$  featured SWCNTs are attracted and aligned on a  $-COOH$  SAMs modified surface which was coated with 16-mercaptohexadecanoic acid (MHA) passivated with ODT and methyl terminated SAMs uniformly. Various structures can be formed on the SAMs such as dots, rings, arcs, letter, thin films and continuous ropes [58]. Rao *et al.* have aligned the CNTs on the Polar Regions preferentially on a patterned substrate that has both polar and non-polar regions [59].

Kang *et al.* have aligned the ZnO nanowires on SAMs modified silicon and gold substrates by using a solution based direct transfer method. The ZnO nanowires were



performed on an Au substrate which was coated with MHA and ODT and driven by capillary force. By dipping the bare and octadecyltrimethoxysilane (OTMS) coated  $\text{SiO}_2$  substrates in the nanowire solution and pulling it out at a constant speed, the positively charged ZnO nanowires were attracted and aligned on the negatively charged MHA regions. A negative bias voltage applied to the substrates can enhance the adsorption rate of the nanowires. The alignment of the nanowires can be achieved by pulling the substrate along a desired direction [60].

Boote *et al.* have studied the assembly of thiolated gold nanowires on substrates which were patterned SAMs of various functionalities by microcontact printing. The nanowires were assembled in the hydrophilic regions of a substrate which was coated with both the hydrophilic and hydrophobic striped patterns. Most of the nanowires were assembled on carboxyl functionalized substrate via hydrogen bonding, compared to surfaces functionalized with carboxyl or salt of carboxyl group compounds and  $-\text{OH}$  terminated groups [61].

There are two substrates with different SAMs:  $-\text{OH}$  and  $-\text{COOH}$  terminated substrate. The pH set for complete deprotonation of acid was generated to study the assembly of the nanowires due to electrostatic interactions. It is observed that the nanowires were assembled on  $-\text{OH}$  patterned regions due to repulsion between  $-\text{COO}^-$  groups of MUA coated nanowires and the substrate. When the substrate coated with

$-\text{COOH}$  terminated and  $-\text{NH}_2$  terminated groups was used, the nanowires were assembled on amine patterns due to the electrostatic attractions. The nanowires were simply assembled or deposited on the patterns without specific alignment or orientation in all these studies [61].

Dip pen lithography can be used to study selective assembly of charged nanowires and carbon nanotubes on various substrates (glass, Si, Au, Al and SiO<sub>2</sub>) where were patterned with SAMs of various functionalities. The study shows that the negatively charged V<sub>2</sub>O<sub>5</sub> nanowires would not naturally assemble on surfaces, since it required an electric potential to assemble on bare regions of the substrate. However, the SWCNTs exhibited strong affinity to the bare regions due to the van der Waals interaction forces, other than the patterned regions of the substrate, which was attributed to the slight negative charges acquired by the SWCNTs during the purification process. This assembly process was applied on fabrication of devices based on assembled nanowires and nanotubes [62].

#### 2.1.3.2 Self Assembly of 1D Nanostructures

Self-assembly of 1D nanostructure is another useful technique which has been widely explored by various groups to generate, especially 2D and 3D assemblies of nanowires, nanorods and nanotubes. The self-assembly of gold nanorods was first studied both in the solution and on the substrates. Nanorods are one dimensional nanostructure with low aspect ratio (3-5) and their diameters are within 100 nm. Thomas *et al.* have aligned gold nanorods longitudinally via intermolecular hydrogen bonding of carboxyl groups by using thiolalkylcarboxylic acids, 3-mercaptopropionic acid (MPA) and 11-mercaptoundecanoic acid (MUA). Gold nanorods solution with MPA (MUA) shows random distribution and those without MPA (MUA) shows longitudinal self-assemblies respectively in TEM images. After mixing the gold nanorods with MPA (MUA), a red shift of the absorption spectra of the nanorods was observed [63].

Murphy and his co-workers have used biotin-streptavidin chemistry to achieve end-to-end alignment of gold nanorods or between the end of one nanorod and the side of another, due to the bilayer of surfactant cetyltrimethylammonium bromide (CTAB) which could stable nanowires and prevent them from agglomerating in the solution [64]. To improve this result, Gole and Murphy used Layer by Layer method to cover the entire CTAB coated gold nanorods surface with poly (acrylic acid) (PAA) to achieve 3D assembly of gold nanorods [65]. Nikoobakht and Al-Sayed showed the evidence of bilayer formation of cationic surfactants on gold nanorods [66]. The biotin molecules attached the entire surface of nanorods by the bonding between carboxylic group of PAA and amine group of biotin. Then streptavidin was added into biotinylated nanorod solution to join individual nanorod for obtaining 3D assembly [67]. The interaction of the nanorods and the 16-MHA SAM was due to electrostatic interactions [68].

Furthermore, CTAB coated gold nanorods can be self-assembled into ordered structures by using adipic acid. The pH dependent electrostatic interaction between the positive charged CTAB gold nanorods and the negative charged deprotonated adipic acid was the driven force of self-assembly. A link between CTAB bilayers on adjacent nanorods formed due to the two carboxyl groups of adipic acid, which leads to a parallel assembly of several nanorods. There were no parallel assemblies formed when two carboxyl groups with longer alkyl chain were used. It was discussed that because large alkyl groups have looped conformations which tended to bend and interact with the substrate [69].

Due to the electrostatic interactions between positively charged CTAB bilayer on the gold nanorods and the negative charge on the DNA backbone, Pan *et al.* have used

DNA to form 1D and 2D nanostructures with various aspect ratios of self-assembled gold nanorods. The concentration of DNA and the aspect ratio of nanorods determined the formation of 1D and 2D nanostructures [70]. Hu *et al.* assembled gold nanorods by thiol linking followed by intermolecular hydrogen bonding between cysteine molecules [71]. Due to gold-thiol linkage, the cysteine molecules, such as thiol, carboxylic and amine groups could attach to the ends of the gold nanorods. Longitudinal assembly of gold nanorods formed due to intermolecular hydrogen bonding. Longitudinal assembly was not observed with other amino acids such as alanine, valine and glycine. Parallel assembly of nanorods with adipic acid which was studied in [70] may not work, probably due to the presence of amine and thiol groups which prevent such interactions [71].

#### 2.1.3.3 Solvent Evaporation Technique

Li and Alivisatos used solvent evaporation on a substrate to obtain macroscopic alignment of CdSe nanorods in a nematic liquid crystalline phase. The convective flow produced by evaporation carries the nanorods from the bulk of the solution to the solid-liquid-air interface as nanorod crystallization occurs. Nanorods have been aligned from head to tail when a monolayer structure formed. The liquid crystalline phases could determine the superlattice crystal structures before the evaporation completed [72].

Nikoobakht *et al.* also studied 1, 2 and 3D structures of gold nanorods self-assembly by solvent evaporation method. The structure formation can be affected by the concentration of nanorod solution, concentration of surfactant, ionic strength and the substrate immersion method into the nanorod solution (partially or completely immersion). They have also achieved the optimum result of dense and well-ordered assemblies of nanorods with low concentration of surfactant (0.001 M) and NaCl (0.05 M)

by partial immersion of substrate into the nanorod solution. The assembly occurred at the solid-liquid-air interface due to the action of capillary forces and surface tension between the liquid and the substrate. The assembly of particles happened due to both the hydrodynamic pressure change between the particles (in the solution and the ones on the substrate) evaporation and the action of capillary forces [73].

Jana *et al.* have also achieved similar assembling of gold nanorods through the same method. However, they studied that the self-assembly was based on both the bilayer of CTAB surfactant which was coated gold nanorod and the action of capillary forces [74].

Guerrero-Martinez *et al.* got similar results by replacing CTAB with a cationic gemini surfactants to obtain 2D and 3D assembly of gold nanorods. The different structures of the micelles caused the differences in the superlattice structures from CTAB and gemini. The CTAB formed spherical micelles while the gemini surfactant formed worm-like micelles due to the presence of long ethylene oxide spacer molecules [75]. Chen *et al.* have used biotin and streptavidin to obtain the end-to-end self-assembly of Au/Ni/Au nanowires conjugated with n by the biotin-avidin linkage [76]. Besides gold, cobalt and CdSe nanorods have also been studied in achieving 3D assemblies on substrates after the drying of the solvent [77, 78]. The 2D net-like structures of CuO nanorods and curved 3D assemblies of Au-poly (pyrrole) heterogeneous nanorods have also been obtained [79, 80].

The researchers have obtained end-to-end assembly of silver nanorods in a three step process, involving approach, attraction and welding. The process was studied and concluded into the action of grown silver nanorods as seeds which attracted other silver

nanorods and silver particles from the solution. The welding occurred due to the attachment of silver nanoparticles from the solution [81].

Wang *et al.* have demonstrated assembly of 14 nm gold nanoparticles into nanochains at butanol/water interface based on a template free solution. The process happened by mixing Au nanoparticles solution and butanol for 1 to 10 days when the nanoparticles initially formed nanochains with some isolated particles to 14 nm diameter nanowires. The nanochains formed due to the aggregation of particles as asymmetric charge distribution. The transformation from nanochains to nanowires was due to Ostwald Ripening mechanism. It was studied that the surface area of the petridish could affect the dimensions of the nanochain and nanowire. Large surface area petridishes produced longer and more aggregated nanostructures. However, there is no change of the transformation from nanochain to nanowire and the length of NW when larger surface area petridishes were used [82].

Apart from the methods discussed above to align 1D nanostructure, some other methods are discussed here. There are studies of obtaining nanofilms from gold and SiO<sub>2</sub> nanoparticles at toluene-water interface by Li *et al.* [83]; peanut like nanostructure and nanowires at water/ethanol interface studied by Xie *et al.* [84]; gold nanorod layer at water-hexane interface studied by Yun *et al.* [85] and gold nanocrystal monolayer at water/oil interface by Reincke *et al.* [86].

Gold nanorods have also been studied and aligned in the bulk and surface of poly (vinyl alcohol) by using a stretch film method [87]. Correra-Duarte *et al.* have performed longitudinal alignment of gold nanorods by using MWCNTs as a template which was concluded due to the longitudinal plasmon coupling between nanorods [88].

Huang *et al.* have achieved nanowire alignment on silicon substrate by the dip coating procedure which was conducted by dipping the substrate into a nanowire solution and pulling out at a controlled speed. It was found that pulling speed, sticking time of the meniscus on the substrate and the slipping distance could determine the distance between adjacent arrays of nanowires. High density of assembled nanowires was decided by the higher sticking time of the meniscus. High pulling speed could deposit nanowires on desired locations. By using this method, they obtained parallel arrays of nanowires covering the entire 4 inch wafer and exhibited linear I-V characteristics [89].

McLean *et al.* introduced a solution based alignment method to obtain parallel alignment of DNA wrapped CNTs on the coated, hydrophilic silicon substrates at  $\text{pH} > 5$ , which was due to the formation of 2D nematic phase formed near the solution-substrate interactions [90].

Duggal *et al.* have generated sheets of single walled carbon nanotubes (SWCNTs) suspended in aqueous solutions by the drip drying method. Sodium dodecylsulfate (SDS) was used as a solvent in this method when the SWCNTs were deposited at the centre of the droplet and no crusting was observed. The pluronic solvent could form a mesh like network that was entrapping the SWCNTs and causing them to align at the periphery [91].

Shim and Kotov have demonstrated their work in aligning SWCNTs on silicon surface by Layer-by-layer (LbL) assembly followed by air blowing. Random deposition of SWCNTs with all the tubes oriented parallel to the substrate surface was done by LBL process. Alignment and stretching of SWCNTs were done by air blowing. This method achieved high efficiency of alignment with 80% of the nanotubes being aligned unidirectional with an angular variation less than  $5^\circ$  [92].

Ko and Tsukruk have aligned CNTs between gold electrodes on amine terminated SAMs for high performance thin film transistors (TFTs) fabrication by using the solvent evaporation technique [93].

Assembly methods for well aligned and assembled 1D nanostructures are useful for application in nanoelectronic, optoelectronic, energy conversion, chemical and biological sensing and data storage devices. These have been approved in concept by many researchers. However, there is still a long way to go before nanoelectronic devices can become commercially available and an intrinsic part of the common man's daily life.

## **2.2 Current Status of Electrospun Anode Material for Lithium Ion Batteries**

Because of their high energy density, long life cycle, and good power performance, lithium ion batteries (LIBs) have been widely used in portable electronic devices [94-97]. However, the theoretical energy density limit of current graphite-based anode (~372 mAh/g) cannot yet satisfy the increasing application demand of LIBs as other more powerful energy storage and renewable power sources [98-100]. Tremendous efforts have been made in the past decade on the search of new anode materials for LIBs, among which silicon (Si) is the most attractive candidate due to its highest theoretical lithium intercalation capacity (~4200 mAh/g) [101]. However, the pure Si anode, in the format of nanoparticles, nanowires, or membrane, still faces adverse issues on electrode pulverization and capacity loss due to dramatic volume change and stress induction during frequent charging/discharging cycles [102-106]. At the same time, non-graphitic carbon materials with nanofeatures, such as nanotubes, nanofibers, and graphene, were also explored as graphite replacement because of their excellent stability, ductility, and conductivity [107-111]. However, these carbon-based LIBs only showed limited



improvement on lithium storage capacity. The adoption of Si/carbon composites seems to be the natural solution for their potential heritage of merits from both carbon and Si based materials. The emerging composites electrodes indeed showed greatly improved electrochemical performance when compared to their carbon or Si counterparts [112]. However, their required material synthesis processes are relatively expensive and difficult for massive production in many cases.

By introducing appropriate carbon nanofiber (CNF) manufacturing approaches (i.e., electrospinning polymer nanofibers and then carbonized into CNFs), Ji *et al* successfully produced CNF-based LIBs electrodes with low-cost and high throughput [113-115]. These CNFs with one-dimensional nanostructure and interconnected network offer more surface area and space than graphite to allow quick lithium ion transport between electrolytes and the active materials so that high charging/discharging rates were attained [116, 117]. Li-active elements (e.g., Si, Ni, Cu, and Fe) were also conveniently introduced into CNFs in some of their work to promote Li insertion/extraction efficiency [118-120].

The common electrospun fibers showed smooth surface and low specific surface area [121], which is not favorable in LIBs as porous structures are believed to help effectively mitigate the stress-induced electrode pulverization during the charging/discharging processes to improve the cycling stability [122]. Porous CNFs could be generated by introducing pore generation agents during nanofiber synthesis, such as physical blending of the electrospinning polymer solution with immiscible polymer (e.g., poly-L-lactic-acid, polymethyl methacrylate, or polyethylene) or some solid nanoparticles (e.g., GaCl<sub>3</sub>, CaCO<sub>3</sub>, or SiO<sub>2</sub>). During or after nanofiber synthesis, pores

were created when thermally decomposing the sacrificial polymer materials or chemically removing nanoparticles by wet etching processes [123-126]. However, this often leads to nanofiber processing challenges (due to the increased fluid viscosity), collapsed nanofibers or nanofibers with reduced mechanical strength.

Lithium primary cells have been on the market for more than 30 years. Sony introduced the commercial lithium-ion secondary cell to the market in 1992. When compared to other battery technologies, Lithium-ion batteries have been an important new generation power sources due to its light weight, cheaper price, higher energy density, less charge lost, no memory effect, longer service-life, higher number of charge/discharge cycles, environmental friendliness, and higher safety. Hence, they can be widely used for portable electronics from digital cameras to notebooks, music players and cell phones. They are also excellent energy-storage systems for vehicles if they can be produced in a smaller sized with higher energy storage capacities [127].

### 2.2.1 Principles of LIB

The anode, cathode, and electrolyte are the three primary functional components of a Li ion battery. Both the anode and cathode are materials which the ionized Li ion are inserted and extracted while electrochemical intercalation changes in the crystallographic and electronic structures. The charging works when Li ions are extracted from the cathode, transported through the Li ion conducting electrolyte, are finally inserted into the anode. While in discharging, the Li ions move oppositely under an opposite electrochemical potential gradient. The terms of charging capacity per unit weight of the materials comprising the electrode usually can be quantified as performance of the anode

and cathode [128]. A schematic diagram of a conventional Li ion battery is shown in Figure 2-3.

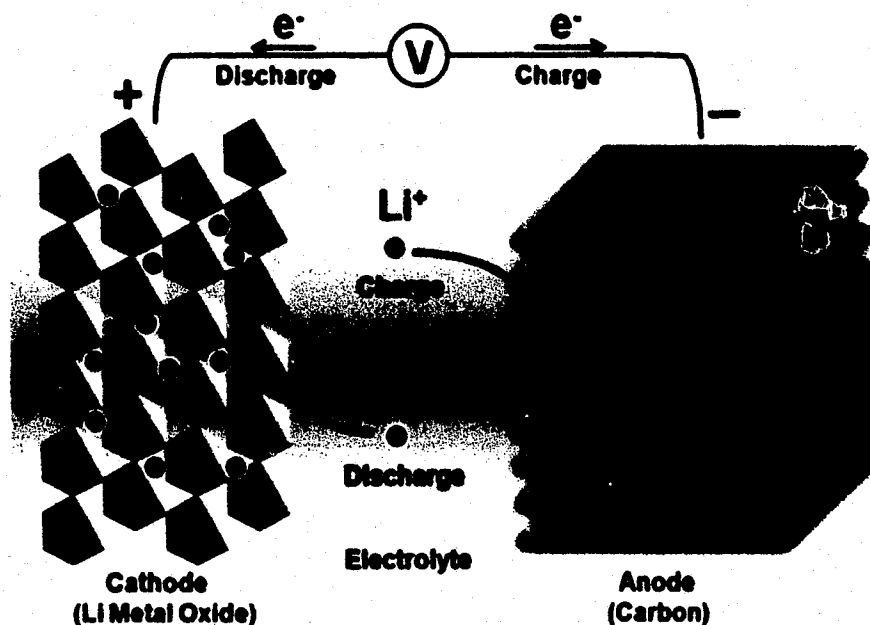


Figure 2-3: Schematic diagram of a conventional Li ion battery [128].

In general, there are three categories of the cathode: layered oxides, transition metal phosphates, and spinels. Solid lithium-salt in an organic solvent could be liquid electrolytes in Li ion batteries. The standards for choosing materials for anode, cathode, and electrolyte are combining effects from physical, chemical, electronic and electrochemical which relate to voltage, capacity, life and safety of a Li ion battery together [128].

### 2.2.2 New Anode Materials of LIB

Rechargeable lithium ion battery has been a type of battery which has the best energy to weight ratio. There are neither memory effects nor discharge rate lost when it is not in use. In this high demanded information and mobile society, LIB has applied on

various areas, such as wireless communication devices, plug in hybrid electric vehicles, stationary storage batteries, microchips, defense application, and electric vehicles.

Compared to most other types of rechargeable battery, LIBs have a higher energy density. At the same size and weight, LIBs can store more energy because Li is one of the lightest electrochemically active metal and the most electropositive elements. Besides this, Li also has many other advantages such as operating at higher voltages, and lower self-discharge rate. At the same time, due to the complicated system of anode and cathode and the need for functioning in non-aqueous electrolytes, LIBs are hard to fabricate and cost more than other batteries which have similar capacity [128].

By improving electrode materials for LIB to reach higher energy capacity and longer cycle life, silicon has been chosen to be one of the most promising anodes because of its highest theoretical charge capacity and its abundance. Due to its huge volume change during the insertion and extraction of lithium, silicon anodes were limited in applications, such as the loss of electrical contact and eventual fading of capacity due to cracking and pulverization. The volume changes can be accommodated by using nanostructure silicon anodes which has the potential to enable a new generation of lithium ion batteries. Porous nanowire/nanorod architecture is one of the approaches to enhance the stress resiliency of Si anodes. Starting by using VLS process to produce Si nanowires, OAD are used to grow Si nanorods to nanometer-scale wall thickness 3D porous Si particles. Getting a thicker Si films is another idea to work on the structure to slow the stress built from inception and harden the surface which could keep from delaminating buckling [128].

All these approaches are going to improve the properties of Si anodes in Li ion batteries before this technology can be commercialized. There are several critical scientific issues that must be addressed. Many things need to be understood, such as the mechanism of stress build-up in the nanostructure during lithiation, relaxation during the rest period, and the correlation of the stress generated with phase transitions during the alloying and reverse de-alloying processes, which are essential to predict how the fracture of the active material can be minimized and completely avoided in the nanostructures. Establishing the capacity dependency and the transportation of electronic and lithium ion on the charge and discharge rates is also crucial. In summary, it is necessary to estimate the irreversible loss and columbic efficiency. By using known cathode material systems with significant cycles to evaluate half cells and full cells is also necessary. To demonstrate commercial viability by extending cycling of the electrode under realistic condition is also required [128].

#### 2.1.2.1 Carbon Based LIB Anode

Among these materials which have been used, graphite or carbon is the most popular material for the anode. Ji *et al.* have studied the fabrication of porous carbon nanofibers by electrospinning and carbonizing PAN/SiO<sub>2</sub> composite nanofibers, with HF acid to remove SiO<sub>2</sub> nanoparticles [129].

They have also prepared porous MnO<sub>x</sub> /PCNFs carbon nanofibers by the electrospinning of a bi-component polymer solution without adding any polymer binder or electronic conductor, followed by thermal treatments under different atmospheres. These porous carbon nanofibers have very high surface area to volume ratio which work as a good material for rechargeable LIB anode to get high reversible capacity and good

cycle stability, not to mention that carbon is an electronic conductor itself. The porous structure and nanometer size of this composite fiber could prevent the  $\text{MnO}_x$  from aggregating and also provide a large contact area for ion and electron transportation [123].

Ji *et al.* reported the preparation of porous carbon manganese oxide composite nanofibers from ultrathin PAN nanofibers by using electrospinning and thermal treatment. These transition metal oxide-load CNFs have many advantages such as developing higher internal surface area, large pore volume and long fiber length, which make lithium ions easily enter into the inner sites of anodes entirely, shorten lithium-ion diffuse distance, and highly improve the rate of electron transport [130].

Ji *et al.* has studied the electrochemically-inert Ni nanoparticles in carbon nanofibers used as LIB anode. They studied how the content of Ni nanoparticles affect the final electrochemical performance. When those composite nanofibers used as anodes without adding binder, high reversible capacities measured at a certain contents of Ni, when the Ni content is too low or too high, low reversible capacities measured with good reversibility and rate performance [102].

#### 2.2.2.2 Si Nanowires Based Anode

Ruffo *et al.* have achieved some good results by using NW electrode in his previous work, but the correlation between chemical performances is still not solved. He has recently developed a way that can accommodate the large volume change and to avoid capacity loss during cycling by attaching nanowires and core-shell NWs to the current collector, which saves using electrode additives such as the binding polymer and conducting carbon. There is another research which is similar to his work [104].

Chan *et al.* have studied Si nanowires whose geometry has several advantages to improve the electrochemical performance when used as oxide cathode materials. The large volume changes due to Si occurs in bulk, or micron-sized materials can be accommodated by the small NW diameter which particles do not fracture further because of the dependent terminal particle size. The direct one-dimensional electronic pathway of silicon nanowires can improve charging efficiency than it is when electrode microstructures based on the particles which electronic charge carriers must move through small inter-particle contact areas. This kind of Si nanowires can be directly produced onto stainless steel current collectors as silicon electrode so there is no need to use binders or conducting carbon, and also all the nanowires can contribute to the capacity [105].

Wu *et al.* examined the nano-size effect and mechanical properties of Si nanowire by comparing the morphology before and after lithiation. The Si NWs remain in contact with the current collector with the large volume change and little fading over 10 cycles which can still achieve the theoretical charge capacity of Si and maintain a discharge capacity close to 75% of this maximum. There were many other related methods for rational Si NW design. For example, good performance of Si NWs can be prepared and coated with carbon by a scalable supercritical fluid-liquid-solid method [131].

The fabrication of Si nanowire anode by metal-induced chemical etching of Si wafers which has the advantage for controlling the crystal orientation and doping was reported. The Zhu's group reported the method of synthesizing carbon-coated Si NW array films, which the Si wafer substrates were completely transformed into Si NWs that prepared by metal catalytic etching of Si and hydrolyzing of a carbon aerogel and the

capacities of the films were from the carbon-coated Si NWs exclusively. The electrochemical performance was enhanced due to the carbon coating which contributed to the capacities of the films.

#### 2.2.2.3 Si Nanoparticles Based Anode

Si nanoparticles have smaller diameters than NWs which also can be considered to replace NWs therefore avoiding mechanical fracture during the volume change. Here, the issue of Si nanoparticles is the loss of electrical contact in Si particle anodes. This happens during other conventional slurry methods which its connection to the current collector is hard to operate and fix during the inevitably volume changes. Wu's group developed a method to prepare Si particle anodes by deposition amorphous Si on the electrode structures. In this method, all the particles can be glued together and bind onto the current collector by amorphous Si as an inorganic glue. Both nanoparticles and micro particles can be successfully cycled by using this method. Hui Wu's group also used the CVD-deposited inorganic glue to connect Si nanoparticles to Si NWs physically and electrically in another study. CVD deposition method takes a longer time, but the real capacity was increased a lot when compared to the bare SiNW anodes [131].

#### 2.2.2.4 Core-shell Si NWs

By studying the methods to synthesize Si NWs, an important principle is to keep electrical connection without pulverization. This introduces the concept of core-shell NW. The active Si is used as the shell material for storage of lithium ions which the core material has a stable structure and is conductive. Hui Wu *et al.*'s group first brought up core-shell NW concept by developing crystalline-amorphous core-shell Si NWs, which has obviously improvement of cycle life and power rate. Compared to C-Si, the Si



reacting with lithium has a higher potential. In order to keep the mechanical support and transportation efficiency from the crystalline core, the charging potential needs to be controlled to remain above the C-Si amorphization potential of 120 mV compared to Li/Li<sup>+</sup>, which can say that only the amorphous Si shell is lithiated. The good part about this method is that the crystalline and amorphous regions of this core-shell Si NWs can be grown without changing the growth temperature. The core-shell concept can be extended by synthesizing carbon-Si core-shell NWs, which is fabricated by the CVD of amorphous Si onto carbon nanofibers [132].

#### 2.2.2.5 Hollow Si Nanostructures

Wu *et al.* have studied Si electrodes of three different nanostructure designs, including encompassing solid, hollow, and clamped hollow nanostructures. Compared to previous studies, they improved performance through developing new designs that successfully address these challenges.

The empty interior space of hollow structures can not only accommodate the volume expansion, but also bring us plenty of advantages, such as lowering the diffusion-induced stress. Here, they studied a finite element model to calculate the diffusion induced stress during lithiation of hollow Si nano sphere, which is five times lower compared to a solid sphere with an equal volume of Si. The significant difference here proves that a hollow structure has a special advantage of readily less fracture. They experimentally exhibit hollow Si nanostructures that have better cycling stability and good performance on electrochemical characteristics have also been explored and proven on hollow Si tubes. Cho's group developed a method by reductive decomposition of Si precursor inside anodic alumina templates to fabricate novel Si nanotube structures. The

advantage of using Si nanotubes here is the lithium ions can intercalate from both sides of the nanotubes due to the surface area could have more access to the electrolyte [132].

#### 2.2.2.6 Hollow Si Nanostructure with Clamping

Several nanostructures had been explored here from solid nanowires to nanoparticles, to hollow spheres and tubes. All of these nanostructures were studied to effectively overcome the pulverization problem of Si electrodes without fracture. However, the unstable SEI has been a big issue that is not solved by using these nanostructures, which is shown in Figure 2-4.

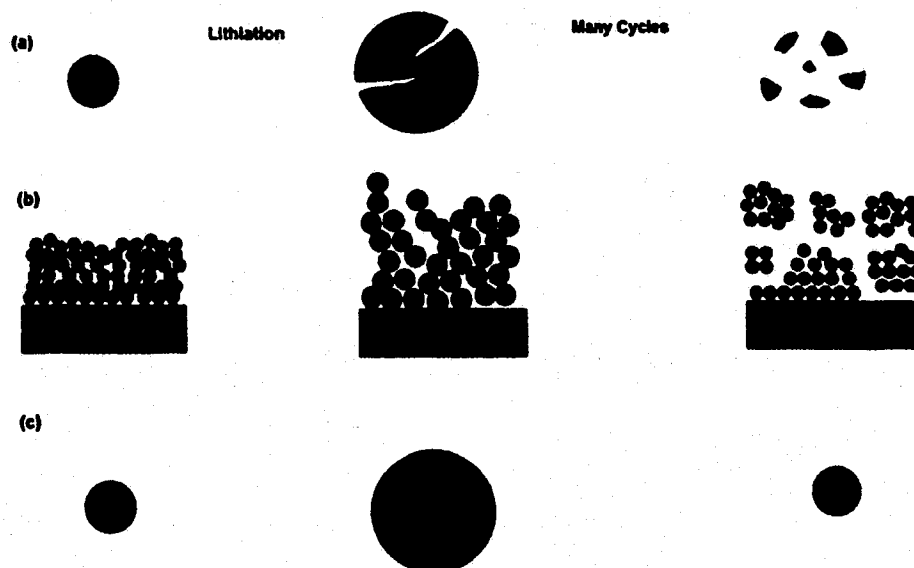


**Figure 2-4:** Si electrode failure mechanisms: (a) material pulverization. (b) Morphology and volume change of the entire Si electrode. (c) Continuous SEI growth [131].

When brought to the whole electrode level, these materials still expand towards the outside and get through volume changes when lithiated. In order to gain a long cycle life in Si anodes and other battery electrode materials which has the same issue of volume changes, it is key to form a stable SEI. In summary, specialized nanostructure design of

Si or Si-based composite electrodes provides an exciting opportunity to study to overcome the unstable SEI formation problem by understanding the SEI formation mechanisms during electrochemical reactions[131].

Wu *et al.* have designed a DWSiNT structure to resolve the silicon material and SEI stability issues, which can be used as a high-performance anode with a long cycle life, high specific charge capacity and fast charge/discharge rates. In this nano-structure design, the oxide shell can help the silicon nanotube from expanding. At the same time, the inner surface is not exposed to the electrolyte which developed a stable solid-electrolyte interphase which could improve the life cycle [133].

#### 2.2.2.7 Silicon/Carbon Nanofiber Composite Anode

Compared to the low theoretical capacity of graphitic carbon as LIB anode, researchers start to use metals, metal oxides, or metal hydrides as new electrodes to get better energy density and lifetime cycle. Silicon-based electrode with its high theoretical capacity is taken as a potential material. When preparing Si electrodes with nanostructures like nanocrystals, nanoparticles, nanowires, and nanotubes, which are expected to get high capacity due to enough surface area to react with Li-ions, carbon nanocomposites have also been emerged with pure Si nanostructures to improve the properties of Si anodes [120].

Ji *et al.* had proposed a strategy to use carbon as the host matrix to prepare different Silicon particle dispersed composites. Carbon was chosen because it works as a cushion for volume change and it also has a good electrical contact during Li insertion and extraction. Recent work proved this kind of Si/carbon composite could show both of their advantages improved the electrochemical performance compared when they work

separately. This method without introducing an additional polymer binder or conductive material, not like the other ones before which complicated and used toxic chemicals [134].

Kim *et al.* have fabricated hybrid carbon nanofibers with over 65wt% high loading of Si by water based electrospinning of PVA (polyvinyl alcohol/Si nanoparticle (NP) solutions for LIB anode. The carbon can not only avoid the unstable electrolyte which interface with the silicon surface, but also reduce the volume change of the silicon. The electrode properties can be improved by combining C and Si in the nanofibers [120].

Ji *et al.* have introduced fabrication of C/Si composite nanofibers by electrospinning and followed with thermal treatments, and how the particle size of Si affects the electrochemical performance. Here, it is found that the effect of volume change can be reduced when Si nanoparticle which is well dispersed in carbon fibers when Si content is not too high. Si nanoparticles are easy to agglomerate in carbon nanofibers when Si contents are higher (30% and 50%). However, the electrochemical performance of Si/C composites is still better compared with pure Si anodes [135].

### 2.2.3 Electrospinning

Electrospinning has its special capabilities of producing fibers from nano-size to micro-size by using polymer solutions under different spinning conditions. The electrospinning process formed a non-woven mat on a metal sheet after the deposition of dry or semi-dry nanofibers. This technique is hard to get aligned nanofibers because of the randomly coiled paths of jets when the polymer jet is ejected at the tip of the cone [136]. Schulz *et al.* demonstrated the electrospinning method to synthesize Si nanofiber as anode with relatively high and stable capacities by using  $\text{Si}_6\text{H}_{12}$  as the Si precursor in a polymer carrier.

Ji *et al.* have prepared Si nanoparticle-incorporated PAN fibers by utilizing the electrospinning followed with a heat treatment. This combination contributes a high reversible capacity and good capacity retention when tested as anodes in LIBs. The volume change caused by silicon during lithium insertion/extraction can be avoided by reducing the Si particle size to the nanoscale, but mechanical failure still happens which caused a limited life cycle. The carbon matrix has offered mechanical stability which prevents the deterioration of Si material and preserve the integrity of the anode, as well as excellent electronically conductive with a long life cycle [137].

#### 2.2.4 Other Methods for Improving LIB Properties

Yao *et al.* have used crab shell as a bio-template to prepare hollow carbon nanofibers encapsulated with sulfur and silicon to form nanostructured electrodes with high specific capacities and excellent cycling performance for LIB [138].

Peresin *et al.* have currently used the materials from renewable resources as reinforcement agents in nanocomposites. Cellulose nanocrystal has been utilized as a material to reinforce polymer matrices because of its renewability, biodegradability, and spectacular mechanical properties. She described the manufacture of electrospun materials based on PVA mats reinforced with CNs [139].

Zhang has used lithium iron phosphate (LiFePO<sub>4</sub>) powders as a cathode material for lithium-ion batteries. For this huge demand of high-performance LiFePO<sub>4</sub> cathodes, it has many advantages from cost to electrochemical properties, and stability to safety. It also has some limitations like poor rate capability caused by low electronic conductivity need to be fixed by using an electronic conductor to enhance the conductivity. After many different methods such as doping with metals, coating with carbon, and reducing

the particle size of  $\text{LiFePO}_4$ , they have been used to reach conductivity-enhancement. In this report, they synthesize  $\text{LiFePO}_4/\text{C}$  composite nanofibers by using electrospinning and sol-gel techniques [127].

Liang *et al.* used electrospinning to fabricate a liquid electrolyte-soaked LLTO/PAN composite fiber-based membrane which has good compatibility and a stable cycle performance with lithium electrode. The average fiber diameter of LLTO/PAN fibers decreased slightly with LLTO content increasing. The membrane shows a high ionic conductivity at room temperature when 15wt% LLTO particles were added. This LLTO/PAN composite fiber-based membrane compared to pure PAN fiber membrane has lower interfacial resistance, higher electrolyte uptake, and higher electrochemical stability [140].

Jung *et al.* have prepared various fibrous  $\text{SiO}_2/\text{PAN}$  composite membranes by electrospinning the composite solutions. They obtained the average fiber diameter reduced by increasing the disperse ability of  $\text{SiO}_2$  particles in the solutions. The fiber diameter related to the stability of  $\text{SiO}_2$  particles. In this study, when  $\text{SiO}_2/\text{PAN}$  composite electrolyte membrane is 12wt%, it shows the best electrochemical performance [141].

#### 2.2.5 Improve Electrochemical Performance by Adding Binder Materials

Szczeczek *et al.* studied a survey on the performance of nanostructured silicon with different morphology from thin film, nanowires/nanotubes, and nanoparticles to mesoporous materials and their nanocomposites. They also examined solvent composition, additives, binders and substrates, which can be considered as other factors affecting the performance of nanostructured silicon anodes. Their study summarized the

achievement and future challenges to silicon nanostructure-anode in large scale application [103]. Finding new polymer binder materials is another way to improve the electrochemical cycling performance of Si nanoparticle electrodes. Wu *et al.* listed two examples here. Liu *et al.* developed a new conductive binder to address the volume change problems in Si through experimentally synthesizing advance materials, analyzing spectroscopic, and simulating theoretically. Both the experimental and theoretical results show much improvement on electronic conductivity. The mechanical force from the binder can both keep the electrical connectivity and avoid the volume change by Si at the same time. All good performances like high capacity, long-term cycling, low over potential between charge and discharge, and rate can be attained by using composite electrodes based on Si particles and the PFFOMB binder without any conductive additive [124].

Yushin *et al.* introduced a new high performance binder called alginate, which is a natural polysaccharide extracted from brown algae. It can be mixed with Si nanoparticles to apply as a stable Si nanoparticle anode. This is very attractive because of its low-cost and compatibility with current slurry manufacturing. Igor Kovalenko *et al.* prepared a stable battery anode by mixing Si nanopowder with a natural polysaccharide extracted from brown algae which has eight times higher reversible capacity compared to graphitic anodes [142].

## **CHAPTER 3**

### **FLOW GUIDED ASSEMBLY CARBON NANOWIRE SENSOR**

#### **3.1 Introduction**

This chapter is based on our published paper: “Manufacturing Nanowire-Based Sensing System via Flow Guided Assembly in Microchannel Array Template,” *Nanotechnology*, 2015. In this chapter, a new flow guided assembly approach is presented to facilitate the formation, alignment, and patterning of nanowires to the desired locations with a microchannel-array based template assembly process. The production and assembly of the nanowires was done simultaneously with zero misalignment. As schematically shown in Figure 3-1, a gas blowing process is adopted to drive a polymer solution along the walls of the microfluidic channels on both sides of a PDMS template. With a trace amount of polymer solution pushed against the wall of these microchannels and dried, highly ordered polymer nanowires with each centimeter long and of a tunable size, were successfully produced in arrays or the lattice format. Unlike in other template synthesis processes where nanowires are randomly distributed or aligned with crossing defects on the substrate, our approach can simultaneously form, position, and pattern nanowires at the desired locations with perfect alignment between contact micropads to facilitate low-cost, scalable production of nanowire-based sensors.



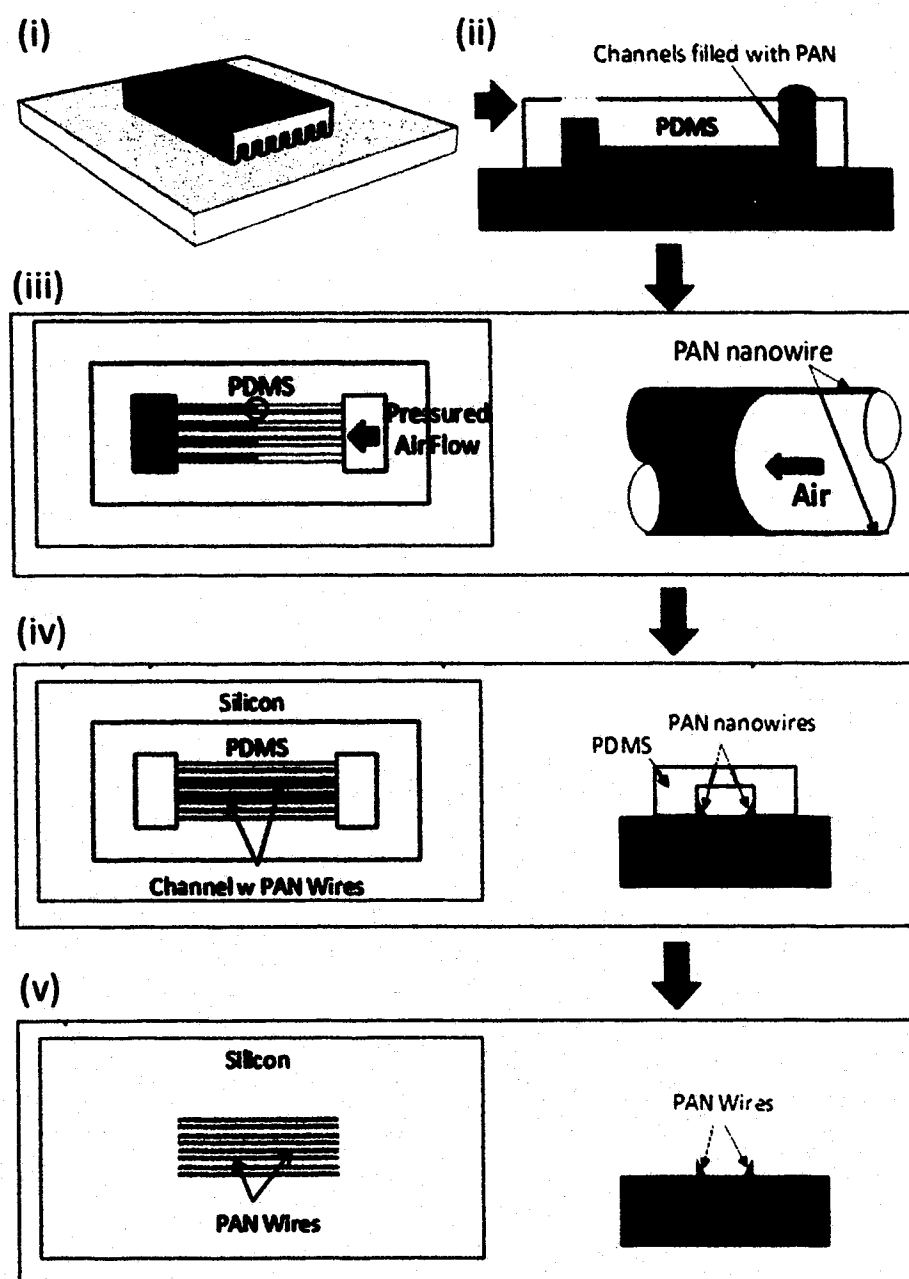


**Figure 3-1:** Schematic of flow-guided assembly of polymer nanowire arrays via a microchannel-array template: (i) attach a PDMS microchannel template on a Si wafer; (ii) fill the microchannels with a polymer solution; (iii) introduce a gas flow to blow away the most polymer solution in the microchannels; (iv) dry the microchannels via continuously blowing; (v) remove the PDMS template to release the polymer nanowires on the Si wafer.

## 3.2 Experiment Methods

### 3.2.1 Chemicals

Polyacrylonitrile (PAN, average MW 150,000), N, N-dimethylformamide (DMF, 99.8%), Bovine serum albumin proteins (BSA), were purchased from Sigma-Aldrich (St. Louis, MO). The PDMS precursor and curing agent kits (Sylgard 184) were purchased from Dow Corning. Phosphate buffer solution (PBS, pH = 7.4) was obtained from Life Technologies, Inc. (Carlsbad, CA) and used to prepare the BSA solutions with different concentrations.

### 3.2.2 Polymer Solution Preparation

Because it is insoluble in water, the PAN solution needs to be prepared with DMF as the solvent. Then the solution is left in the oven at 60 °C overnight to let the PAN dispersed in DMF evenly. The PAN in the DMF solution was prepared with different concentrations, such as 0.1 wt%, 0.5 wt%, 1 wt%, 2 wt%, 4 wt%, and 10 wt%. The color of the solutions turns from light to yellow as the concentration increases. The BSA solutions are prepared with DI water. The concentrations are 1 pg/ $\mu$ l, 2 pg/ $\mu$ l, 4 pg/ $\mu$ l, 10 pg/ $\mu$ l, 25 pg/ $\mu$ l, 50 pg/ $\mu$ l, 75 pg/ $\mu$ l, 100 pg/ $\mu$ l.

### 3.2.3 Microfluidic Channel Template Fabrication of PAN Nanowire

The microfluidic channel template was fabricated by soft lithography. Micropatterns were first fabricated on a silicon wafer by photolithography and dry etching process. Briefly, a Si (100) wafer was patterned with photoresist (PR), and the pattern was then transferred onto the Si substrate via deep reactive ion etching (DRIE). The DRIE etching step was performed through a Bosch process with a gas mixture of SF<sub>6</sub> and C<sub>4</sub>F<sub>8</sub>. As for demonstration, the microchannel array template has 200 microchannels,

each  $30\ \mu\text{m}$  wide,  $5\ \text{mm}$  long, and separated by a gap of  $30\ \mu\text{m}$  (Figure 3-2). This gives a total of  $12\ \text{mm} \times 5\ \text{mm}$  microchannel pattern. Figure 3-3 shows the image of the microchannel array fabricated on a silicon wafer.

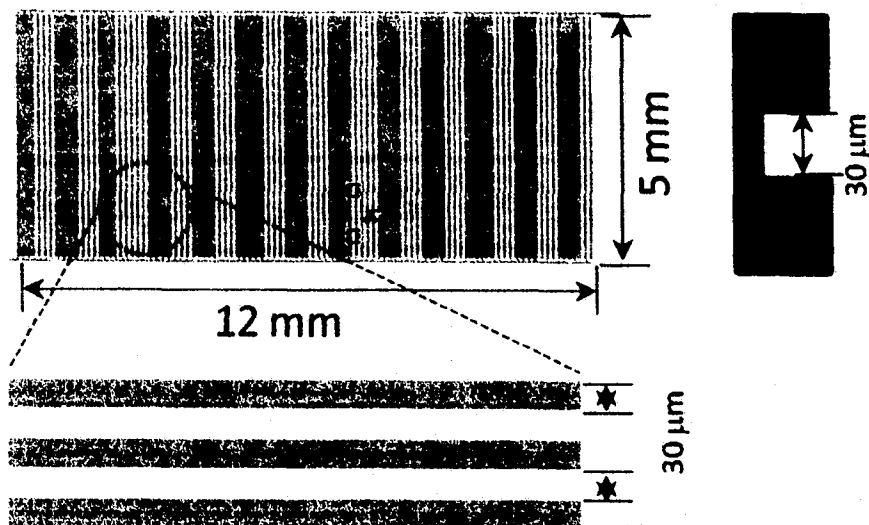


**Figure 3-2:** Microchannel pattern design.



**Figure 3-3:** An optical microscopy image of the fabricated micropatterns on a silicon wafer.

The PDMS precursor and curing agent are mixed at ration 10:1. After stirring it completely, put it in the vacuum to remove those bubbles. The produced micropattern was then transferred to a PDMS template by negative replication molding (Figure 3-4).

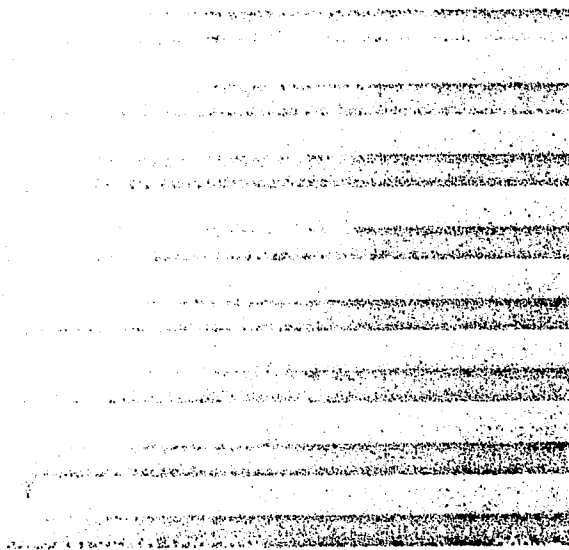


**Figure 3-4:** SEM images of PDMS template with microchannel arrays.

After pouring the PDMS solution on the wafer substrate (pattern) evenly, use a syringe tip to remove the bubble caused during pouring. Place the substrate on a hotplate at 60 °C for 4 hours or more to cure. Liquid receiving wells were punched on both ends of the microchannels with a biopsy puncher (5 mm) prior to sealing to another piece of clean Si wafer (with a thin oxide layer coated on the top) via conformal contact.

#### 3.2.4 Gas Blowing-based Flow-Guided Assembly Process

The workflow of this gas flow guided assembly process is schematically shown in Figure 3-1. One drop (2  $\mu$ L) of a polymer solution (e.g., PAN in DMF) is loaded in the receiving reservoir of the microfluidic channels on one end, allowing filling the entire channel by capillary forces automatically. If the solution has a very high solid content and too viscous to flow without extra pressure, forced filling with vacuum suction from

the other side of microchannels is applied. Then the filled microchannels are introduced a gentle N<sub>2</sub> gas flow (~10 ml/h or above) from the liquid loading side to blow out most of the polymer solution from the other open end. The gas blowing process continues for an additional 30 sec to ensure complete drying of all the microchannels. A residual amount of polymer accumulates along the side wall of these microchannels. After removing the PDMS template, PAN strands of nanometer size are left on the Si substrate with their position and orientation pre-defined by the microchannel pattern.

### 3.2.5 Carbon Nanowire Production by Carbonation

To make nanowires conductive, the assembled PAN nanowires were first stabilized in a furnace filled with air at 280°C for 6 h at a heating rate of 5°C /min. The resulting nanowires were further carbonized at 700°C for 1 h in nitrogen gas with a heating rate of 2°C min<sup>-1</sup>, following a common protocol. The produced carbon nanowire array was then integrated into the sensors by connecting their far ends together with carbon-based conductive paste to form electronic contacts.

### 3.2.6 Carbon Nanowire Sensor Testing

I-V characteristic for each nanowire sensor was measured on a Keithley 4200 Semiconductor Characterization System (SCS) coupled with a CASCADE Microtech probe station. The electrical current was measured when a constant voltage of 0.7 V was applied across the nanowire array.

## 3.3 Results and Discussion

### 3.3.1 Characterizations of Nanowires

After removing the PDMS template, PAN strands of nanometer size are left on the Si substrate with their position and orientation pre-defined by the microchannel

pattern, as shown in Figure 3-5. Figure 3-5 shows the SEM images of the formed PAN nanowires after gas blowing a 2% PAN/DMF solution. PAN nanowires with a width of 100-150 nm on the top end (see supplemental Figure 3-6), each a centimeter long, were successfully produced in a large array.

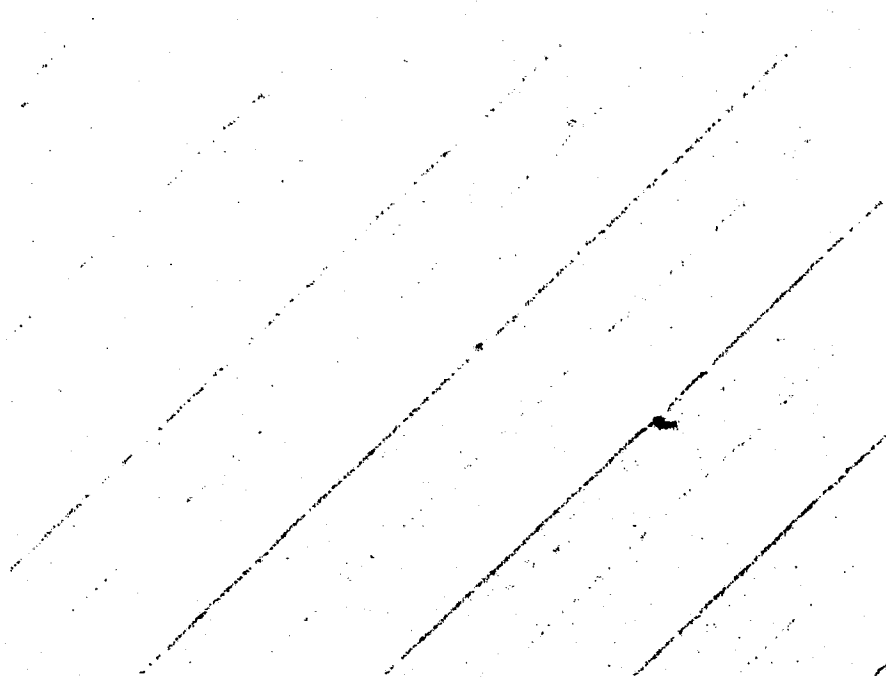


**Figure 3-5:** SEM image of the produced PAN nanowires on Si substrate.

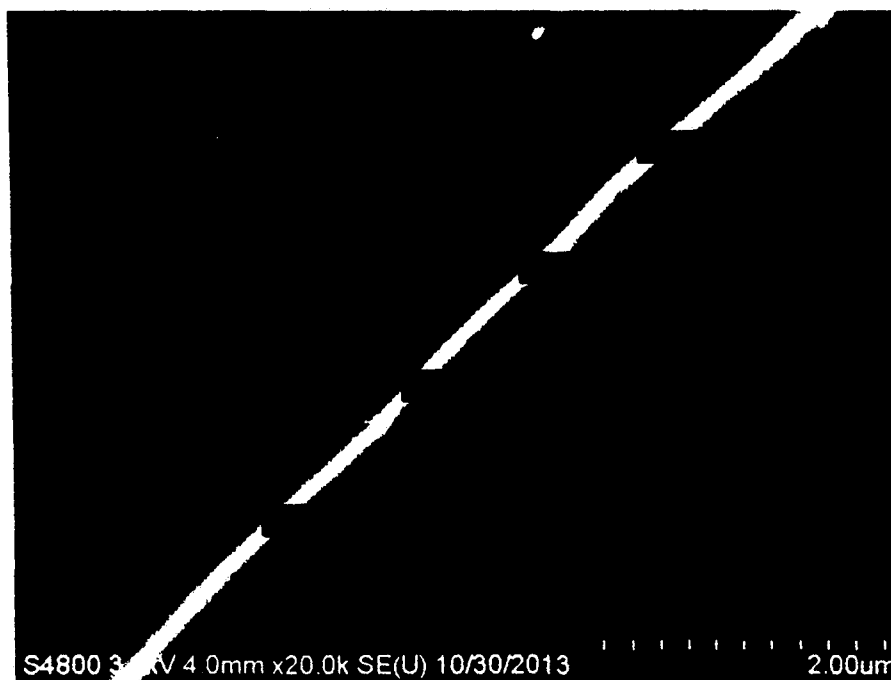


**Figure 3-6:** SEM image of the sharp end of PAN nanowires assembled with 2wt% PAN/DMF solution.

The size of PAN nanowires could also be tuned in some ranges, determined by the gas flow rate and the PAN concentration. PAN/DMF solutions of various solid contents (0.1-10 wt %) were tested. Blowing a too dilute solution (e.g., 0.1%) in the microchannels produced many broken nanowires though well aligned (Figure 3-7a). Continuous nanowires were obtained when assembled with a PAN solution as low as 0.5 wt% solid content (Figure 3-7b).

High quality PAN nanowires were consistently produced with PAN solutions of 1.0-4.0 wt% (Figure 3-7c). The use of a too concentrated solution (5-10 wt%) led to thick polymer bundles or even continuous, hollow thin PAN film, as shown in Figure 3-7d.

Note: too concentrated PAN solutions also require vacuum suction from the other end of the microchannels to assist fluid filling. Generally, a PAN solution of 1.0-2.0 wt% solid content seems optimal in terms of the assembly operation convenience (i.e., easy

filling, large blowing rate window) and the quality of produced nanowires (i.e., assembly reliability and defect tolerance). Besides the solid content, the  $N_2$  gas flow rate is another critical factor determining the integration and quality of nanowires in this flow-guided assembly process. Its contributions are complicated as the assembly process is closely coupled with the dynamic evaporation of the solvent. These two phenomena work together to affect the amount of polymer left along the microchannel wall. Nonetheless, a weak air flow resulted in a severe spread of PAN from the microchannel wall and the formation of thin-wall hollow microscale tubules, similar to the case with PAN solution with too high of a solid content (Figure 3-7d). A minimum flow rate (e.g.,  $\sim 1.0$  ml/h) was found necessary to guarantee good integration of the produced nanowires.

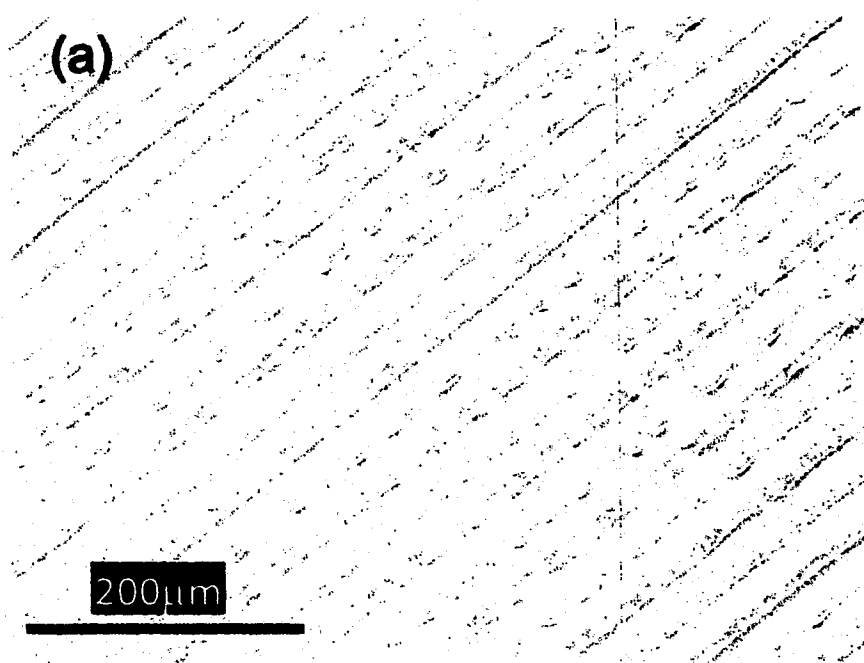


**Figure 3-7a:** The assembly quality of the nanowires with PAN solutions of various concentration: 0.1%, The  $N_2$  gas flow was fixed at  $\sim 1.0$  ml/h.





**Figure 3-7b:** The assembly quality of the nanowires with PAN solutions of various concentration: 0.5 %, The N<sub>2</sub> gas flow was fixed at ~1.0 ml/h.

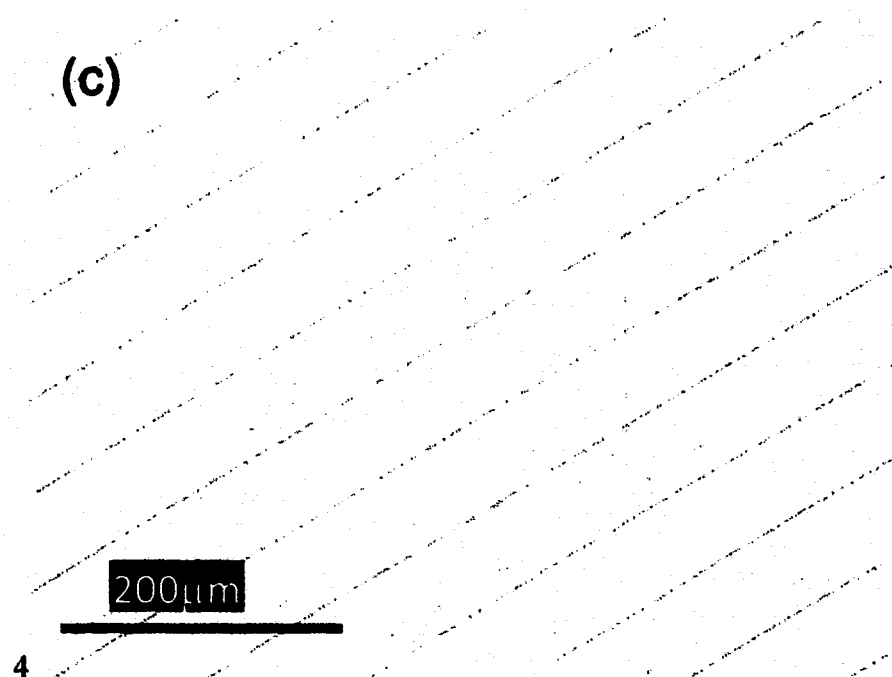


**Figure 3-7c:** The assembly quality of the nanowires with PAN solutions of various concentration: 1 %, The N<sub>2</sub> gas flow was fixed at ~1.0 ml/h.



**Figure 3-7d:** The assembly quality of the nanowires with PAN solutions of various concentration: 10 %, The N<sub>2</sub> gas flow was fixed at ~1.0 ml/h.

The gas flow rate and the PAN concentration affect not only the integration and quality of the produced nanowires, but also the dimensions of the nanowires. AFM was used to measure the height of the nanowires (Figure 3-8a).

As shown in Figure 3-8b, the height of the nanowire varies with the original concentration of PAN used in the flow guided assembly process and 200-600 nm high nanowires are obtained for PAN solutions with a 0.5 wt%- 4.0wt% solid content.

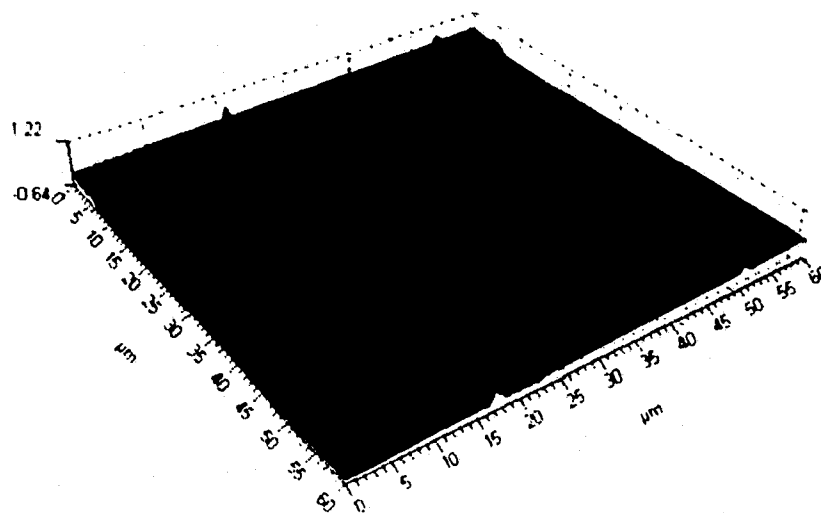


**Figure 3-8a:** An AFM image of PAN nanowires on a Si wafer produced with 2.0 wt% solid content.

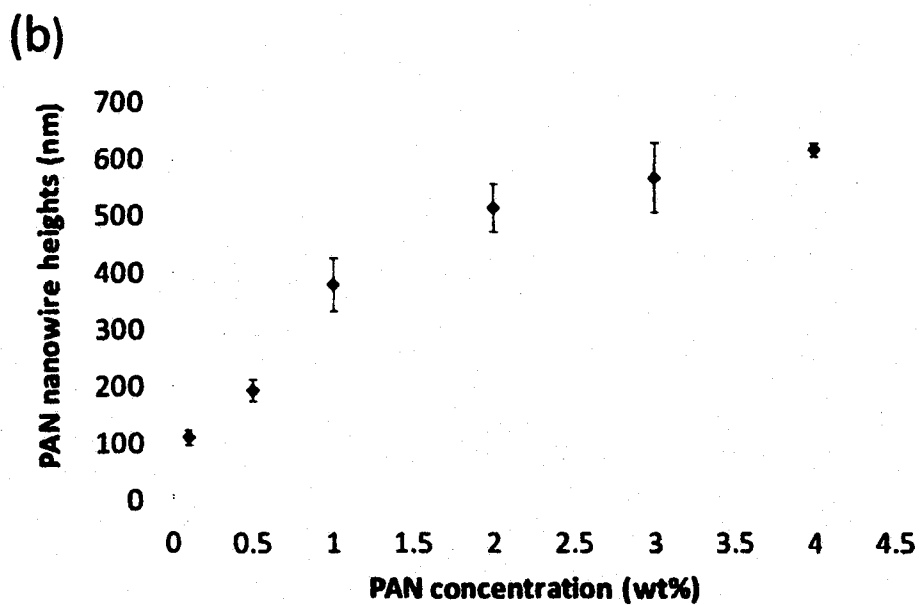


**Figure 3-8b:** The height of PAN nanowires produced with various PAN solution concentrations.

### 3.3.2 Characterization of Carbon Nanowires

To make nanowires become conductive, the patterned PAN nanowires were further converted to carbon nanowires. The carbonization was done following a common procedure which has been used for years in carbon nanofiber industry [143]. During this stabilization step, PAN went through complicated chemical processes, including oxidation, cyclization, dehydrogenation, aromatization, and cross-linking, as illustrated in Figure 3-9a. When comparing the SEM and AFM images of PAN nanowires (Figure 3-5 and Figure 3-10) and further carbonized nanowires (Figure 3-9b and Figure 3-11), the structure and pattern of the PAN nanowires retained well after carbonization, though some weight loss and size shrink occurred. The height of the produced nanowires shrank ~45%-65% of their original value after carbonization, as shown in Figure 3-12. Such dimension shrinkage varies with the original solid content of the PAN solution applied in the flow-guided assembly and a minimum shrinkage of 45% exhibited for a polymer solution of ~3% solid content under the given carbonization conditions.

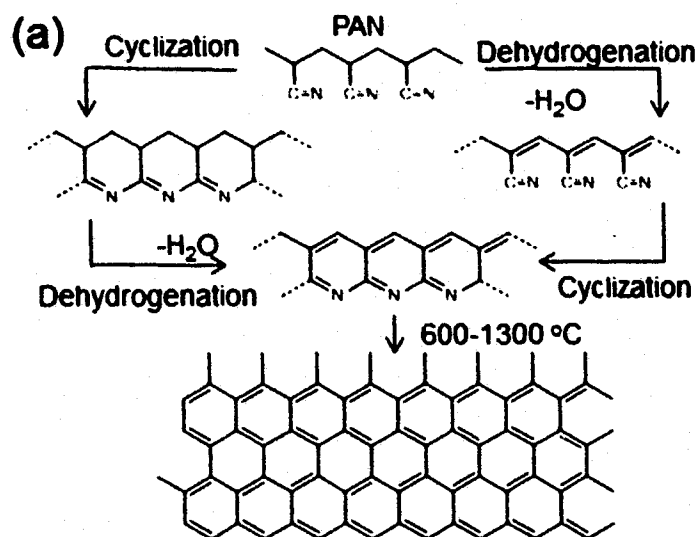


**Figure 3-9a:** A typical PAN carbonization procedure and involved structure evolution.

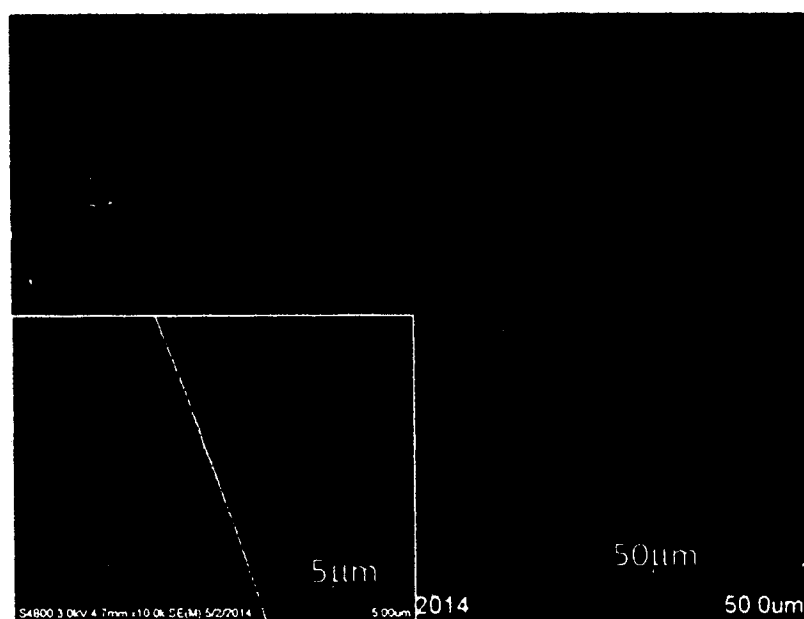


**Figure 3-9b:** SEM image of carbon nanowires after single-assembly.

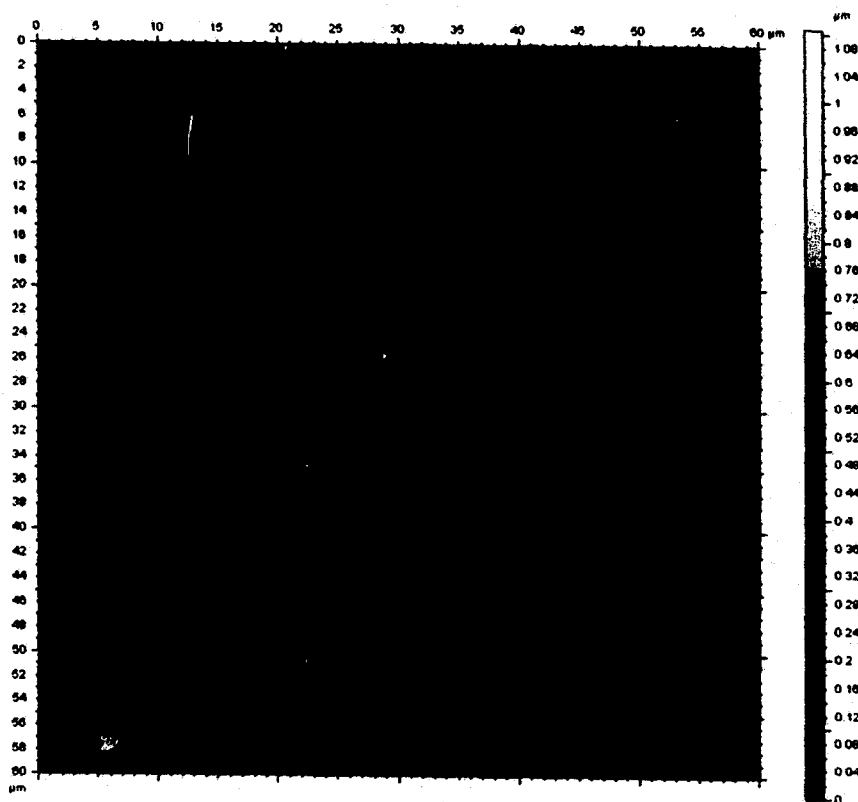


**Figure 3-10:** AFM images of PAN after single-assembly.

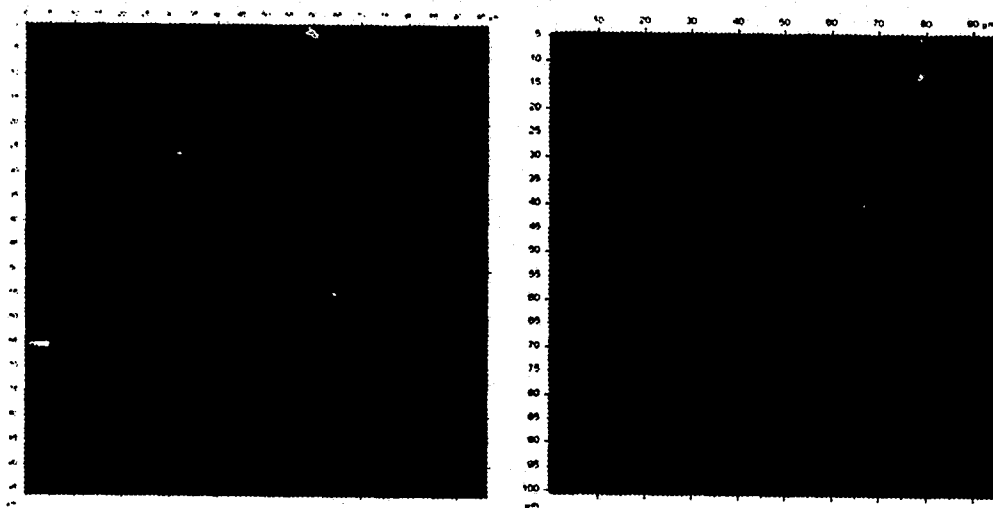


**Figure 3-11:** AFM images of carbon nanowires after the double-assembly process.

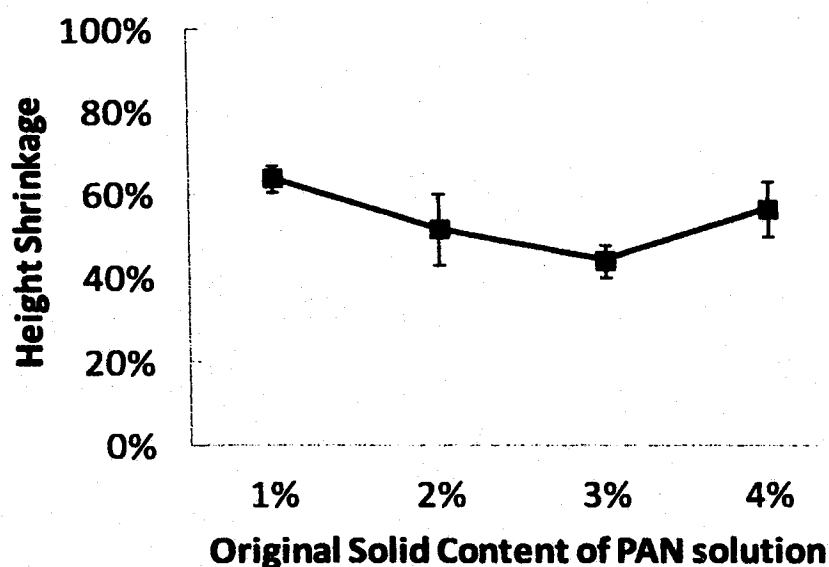


**Figure3-12:** The height shrinking percentage of nanowires before and after carbonization.

### 3.3.3 I-V Characteristic/ Sensor/ Conductivity Test

The produced carbon nanowires were further integrated into the electronic devices to evaluate their sensing performance. Briefly, the nanowire area was first covered by a layer of S1813 with a thickness of  $\sim 1.5 \mu\text{m}$ . A  $100\text{-}\mu\text{m}$  wide microchannel was then opened across the wafer perpendicularly to the nanowire orientation to allow exposure of carbon nanowires (Figure 3-13). This defines the actual window dimensions of the nanowire sensor as well as shortens its response time to the targeting probes. Carbon-based conductive paste was then applied to the far ends of the carbon nanowires to create contact electrodes. Bovine serum albumin (BSA) proteins were dissolved in phosphate buffered saline (PBS, 1X) and a drop of the prepared BSA solution ( $2 \mu\text{L}$ ) with appropriate concentration was loaded. When protein molecules are bond to the surface of the nanowires, charges accumulate there, leading to a jump of the conductance signal [144, 145].

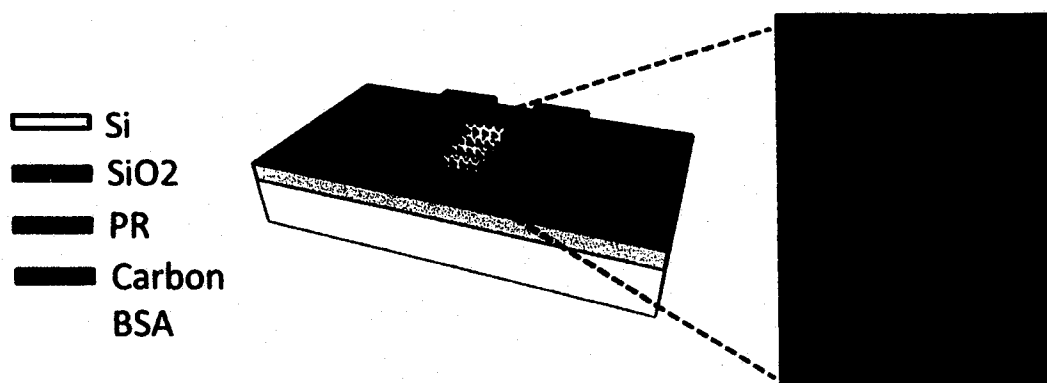
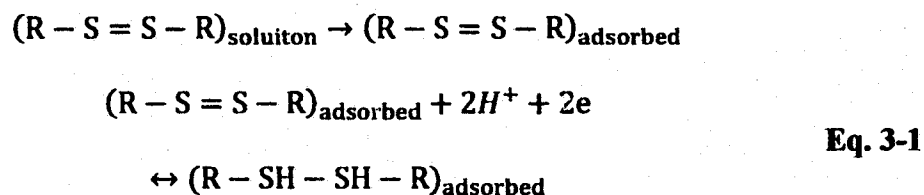


**Figure 3-13:** Schematic of the sensor integrated with the assembled carbon nanowires.

The redox reaction of BSA is expected to take place on the sulfur double bonds because BSA has no metal ions. The process may thus be written in Eq. 3-1 as follows [146]:



Four-probe measurement was done to record the conductance and conductance change from the current-voltage (I- V) characteristic curves. As shown in Figure 3-14, there is a significant jump in the time-dependent conductance measurement when switching from pure PBS to 1.0 pg/mL BSA solution. The appreciable detection of the conductance change gave a signal-to-noise ratio higher than 13. Such conductance increase was stabilized rapidly after the injection, attributed to the integration of the microfluidic channel. Stepwise conductance increase was found upon the increase of BSA concentration to 2, 4, 8, and 10 pg/mL. Further addition of protein exhibited a quick



slowdown on the growth of the conductance difference and the appearance of a conductance difference plateau at 25  $\mu\text{g}/\text{mL}$  (Figure 3-15).

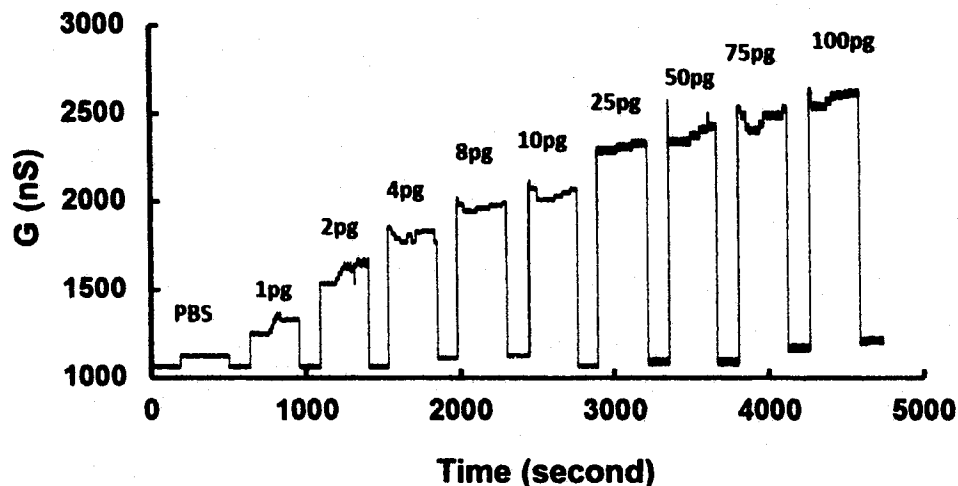


**Figure 3-14:** The conductance measurement of the produced nanowire sensors when adding BSA solutions of various concentrations.

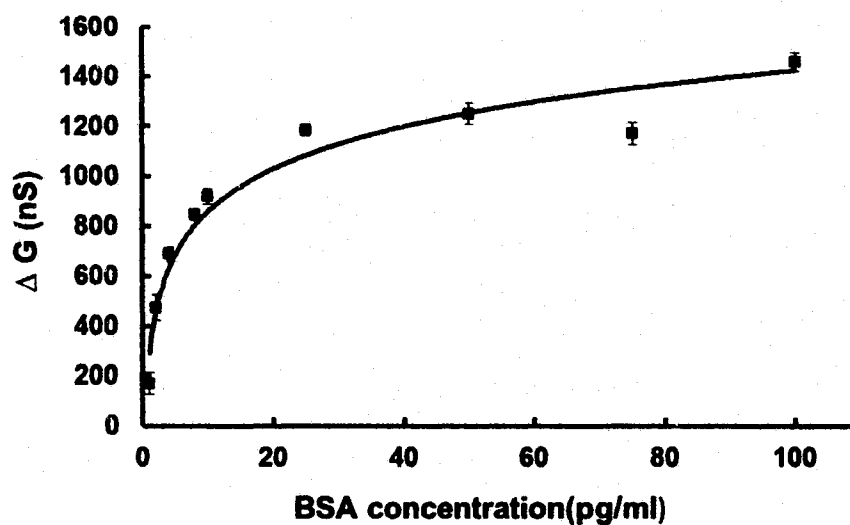


**Figure 3-15:** The relationship of the conductance difference of the nanowire sensor to the BSA concentration. A total of 35 nanowires patterned in parallel between two terminal electrodes were used in the tests.

This is due to the saturated negative charges near the surface of the nanowires. The sensitivity of this sensor is  $\sim 120$  mA/g, which is much higher than the current existing nanowire sensors [146].

#### 3.3.4 Characterization of “T” Shape and “Cross” Shape Nanowire

The nanowires have a slightly non-even surface, which is believed to be the result from the dynamic evaporation during gas blowing. Besides the simple “I” shape nanowire array, other important nanostructures such as “T” and “cross” shape nanowire lattice can also be produced when such flow-guided assembly process is applied twice. As shown in Figure 3-16, a second solution is introduced into the microchannels of the PDMS template which is orientated perpendicularly to the previous aligned polymer nanowires on the Si substrate. When a more diluted PAN solution or the solvent alone is used during this second assembly step, the fluid breaks up or dissolves part of the already aligned nanowires exposed in the microchannels.

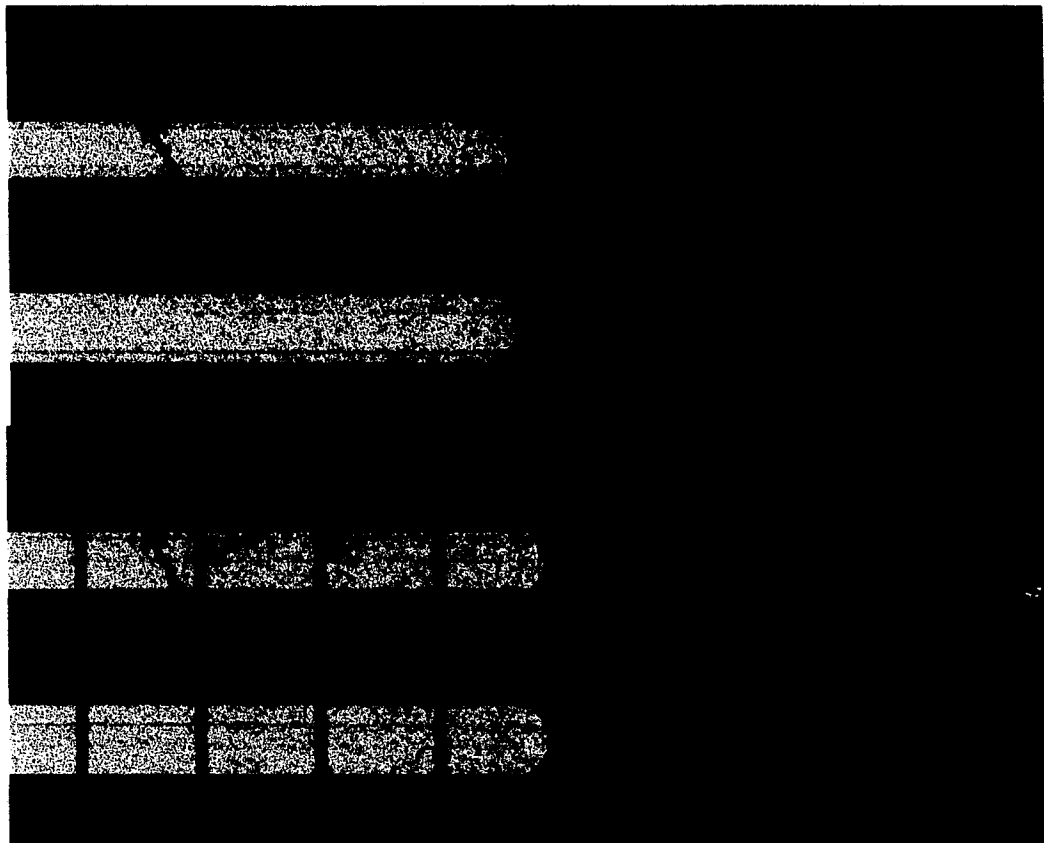


**Figure 3-16:** Schematic of double flow-guided assembly.

New nanowires are formed and aligned in the microchannels in this new orientation, meeting with the early produced nanowires to form “T” junctions (Figure 3-17). When the same or more concentrated polymer solution or the same solution but with an incompatible solvent is used in the second flow-guided assembly process, “cross” shape junctions formed (Figure 3-18).

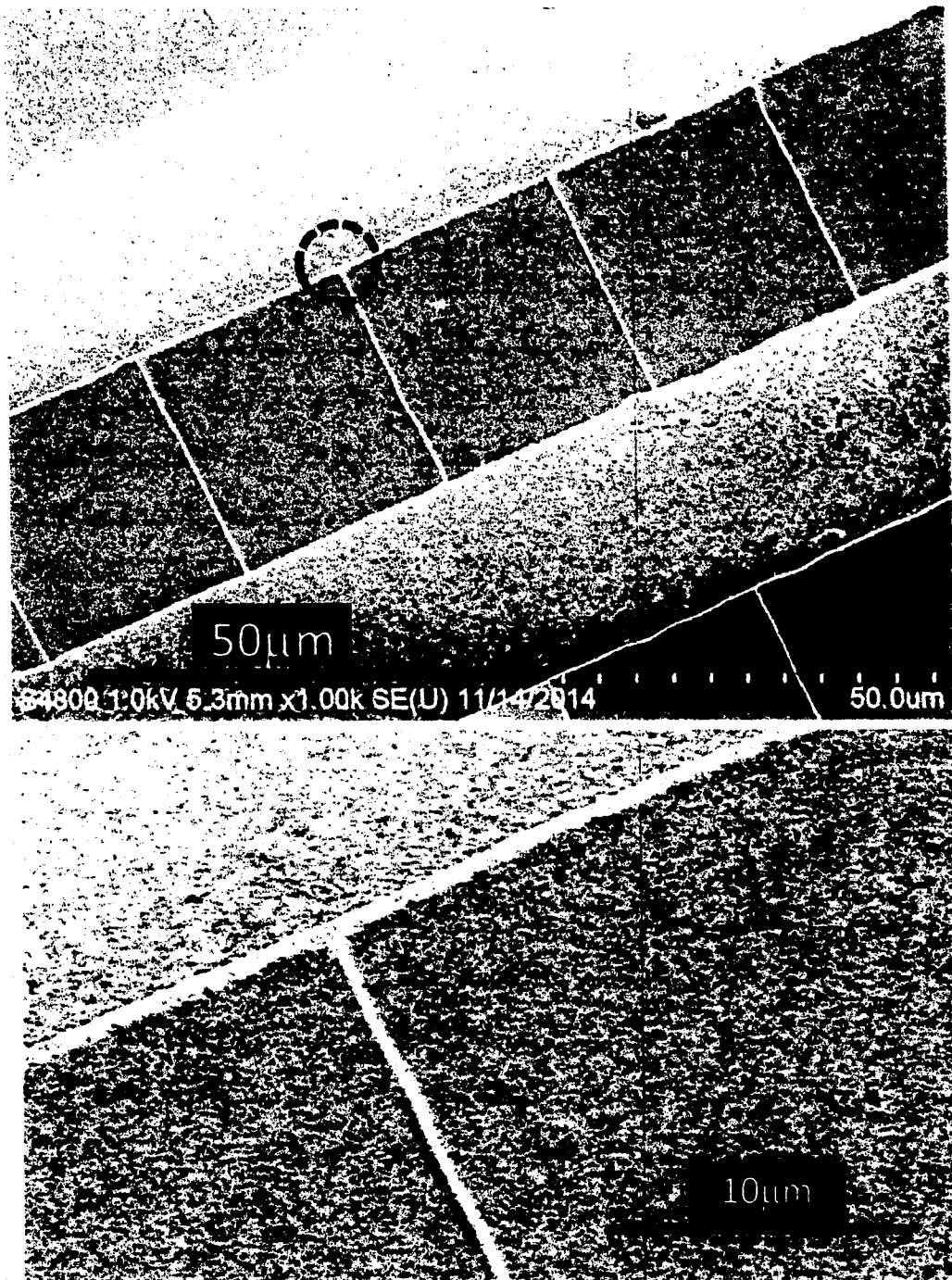


**Figure 3-17:** SEM images of produced polymer nanowires: "T" shape.

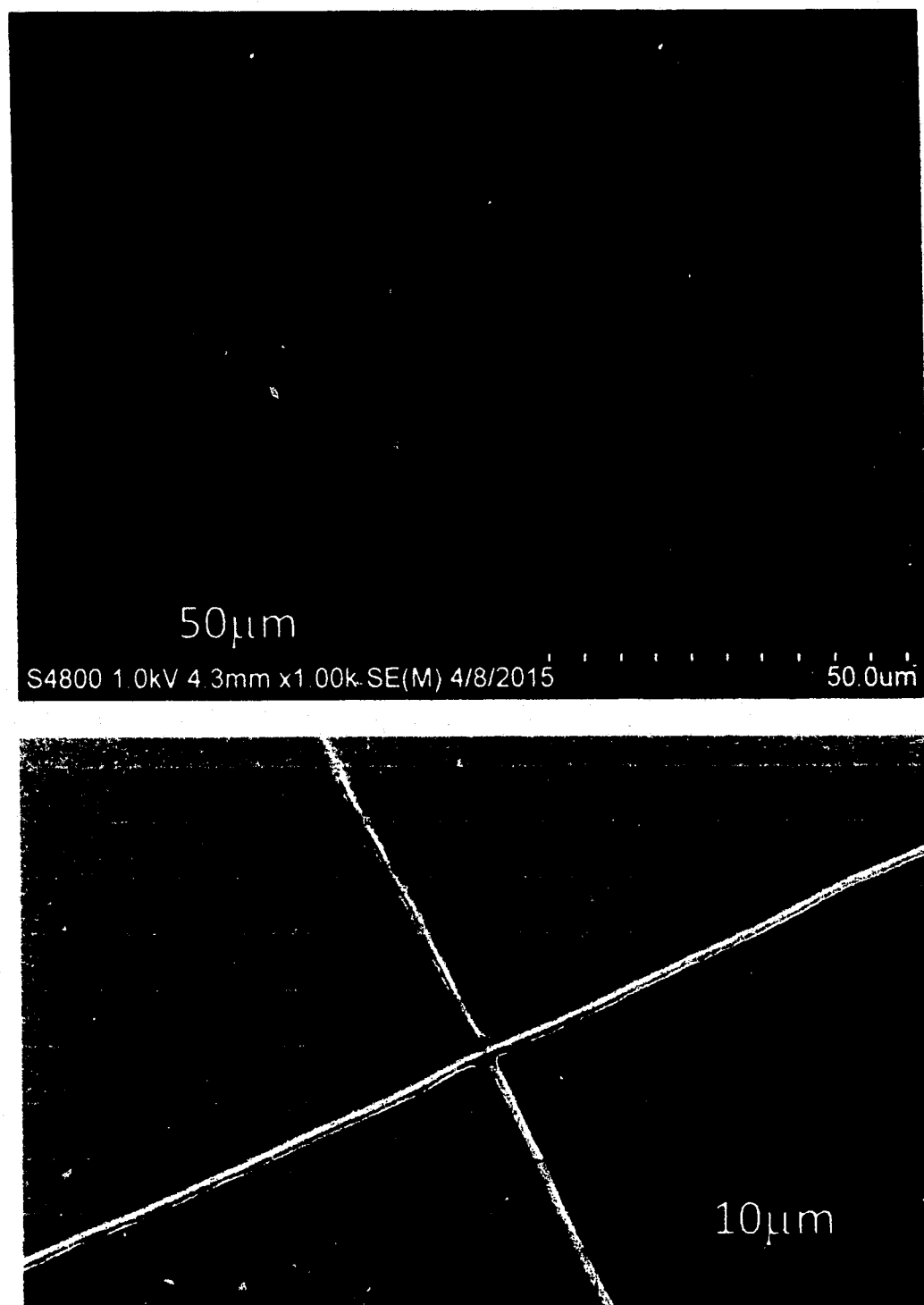


**Figure 3-18:** SEM images of produced polymer nanowires “cross” shape.

The cross-section of nanowires showed a typical “V” shape due to the fluid meniscus (Figure 3-19a), with the base width several hundred nanometers and the sharp end from several tens to over 100 nm. Because of that, the T-shape or cross nanowires shown in Figure 3-17 and Figure 3-18 were actually connected in the base at the intersection as the same polymer solution (or solvent) was used during the double assembly process (Figure 3-19b). Note: if incompatible solutions or different materials are used during the double assembly process, a bridge cross should be formed.

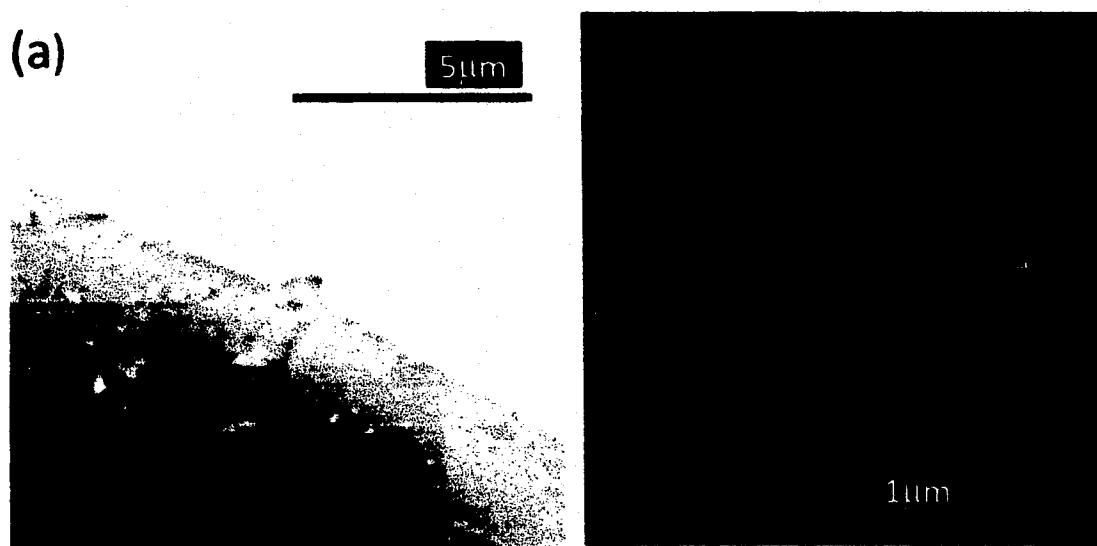


**Figure 3-19:** SEM images of (a) the cross-section of PDMS negative replica of a PAN nanowire; (b) intersection of cross nanowires.

### 3.3.5 Conclusions

In summary, we have patterned and aligned the nanowires to the desired locations with zero misalignment by using a microchannel-array based template and this flow guided assembly approach. This gas blowing process can help align and pattern the polymer along the walls of the microfluidic channels on both sides on a pre-defined PDMS template. By using these microchannels, highly ordered polymer nanowires can be produced in the arrays or lattice format with a tunable size.

## CHAPTER 4

### ELECTROSPINNING/FOAMING PRODUCTION OF POROUS SILICON/CARBON NANOFIBERS ANODE FOR LIB

#### 4.1 Introduction

This chapter is based on our published paper: “Foamed mesoporous carbon/silicon composite nanofiber anode for lithium ion batteries,” *Journal of Power Sources*, 2015. In this chapter, a new electrospinning/foaming process is presented to produce mesoporous Carbon/Silicon (C/Si) composite nanofibers. In our approach, a polyacrylonitrile (PAN)/silicon nanoparticles suspension solution was first electrospun to form PAN/silicon composite nanofibers. Aluminum acetylacetonate,  $(Al(C_5H_7O_2)_3)$ , AACA, with a sublimation temperature of 193°C [147]), was also dissolved in the PAN solution prior to the electrospinning process. The produced nanofibers first went through an oxidative stabilization step to create a conjugated ladder structure. Mesopores were created in PAN/silicon nanofibers during this thermal treatment when AACA was sublimated. The produced mesoporous composite nanofibers were then carbonized to form C/Si fibrous composites.

Unlike other pore formation processes (i.e., using immiscible polymer or sacrificial nanoparticles), no special treatment or care is needed during the electrospinning process or the later thermal treatment. The foaming agent, AACA, can be completely dissolved in the PAN/DMF solution and sublimated during the later thermal treatment. The produced mesoporous C/Si/AACA composite nanofibers, when used as



LIBs anode, showed higher energy and power density as well as better cycling performance when compared with those nonporous C/Si composite nanofibers and CNF alone which were processed in a similar way. The entire manufacturing process is illustrated in Figure 4-1.

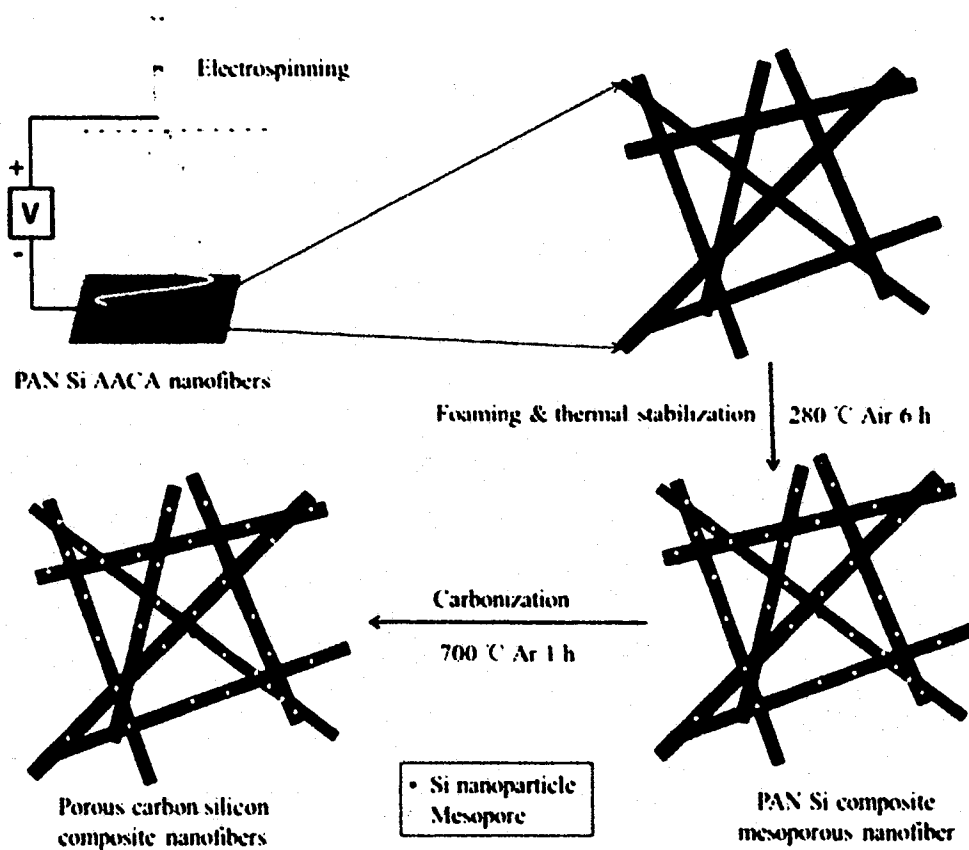


**Figure 4-1:** Schematic of the one-step foaming/electrospinning process in the manufacture of mesoporous C/Si/AACA composite nanofiber.

## 4.2 Experimental Methods

### 4.2.1 Chemicals

Polyacrylonitrile (PAN, average MW 150,000), N, N-dimethylformamide (DMF, 99.8%), aluminum acetylacetonate (AACA, 99%), lithium hexafluorophosphate ( $\text{LiPF}_6$ , 99.99%), ethylene carbonate (EC, 99%), and diethyl carbonate (DEC, 99%) were purchased from Sigma-Aldrich (St. Louis, MO). Si nanoparticles (99%, with an average diameter of  $\sim 100$  nm) were purchased from MTI Corporation (Richmond, CA). All chemicals were used without further purification unless specified.

### 4.2.2 Materials Preparation

The mesoporous C/Si composite nanofibers were prepared using a common electrospinning process, followed by carbonization. Typically, Si nanoparticles (30 wt%, with respect to PAN) and AACA (30 wt%, with respect to PAN) was dispersed in a 10 wt% PAN/DMF solution at  $80^\circ\text{C}$ . Strong mechanical stirring was applied for at least 72 h to ensure homogeneous dispersion. The suspension was then loaded in a plastic syringe and extruded through a 30 G stainless steel needle (from Nordson EFD Corporation) at a flow rate of 0.75 ml/h. A directional current electric bias (24 kV) was added between the needle end and a grounded aluminum pan collector with a needle-to-collector distance of 15 cm through Gamma ES-40P power supply (Gamma High Voltage Research, Inc.).

The electrospun composite nanofibers (denoted as PAN/Si/AACA) were then collected and stabilized in air at  $280^\circ\text{C}$  for 6 h (with a heating rate of  $5^\circ\text{C}/\text{min}$ ). During this stabilization step, AACA was sublimated to create pores in PAN/Si nanofibers. The resulting porous nanofibers were further carbonized at  $700^\circ\text{C}$  for 1 h in argon gas (with a heating rate of  $2^\circ\text{C}/\text{min}$ , following a common protocol as in Ref [148] ) to produce

porous carbon/silicon composite nanofibers (denoted as C/Si/AACA composite nanofibers in a later description). For comparison purpose, PAN nanofibers (without the addition of Si and AACA) and PAN/Si composite nanofibers (with Si, but no AACA) were also prepared and carbonized in the same process and denoted as CNFs and nonporous C/Si composite nanofibers, respectively.

#### 4.2.3 Characterization

Scanning electron microscopy (SEM) images were taken using a Hitachi S-4800 instrument at 1.0 kV. All samples were sputter coated with gold to reduce the potential charging effect. The energy-dispersive X-ray spectroscopy (EDX) was conducted by TEAM EDS analysis system installed on SEM at 20 kV.

Nitrogen adsorption isotherms were obtained at liquid N<sub>2</sub> temperature on a Quantachrome Instruments NOVA 2200 surface area analyzer. Before the measurements, the samples were degassed at 300°C for 3 h. The total surface area was calculated according to the Brunauer–Emmett–Teller (BET) method. The pore volume and size distribution was obtained by the Barrett–Joyner–Halenda (BJH) analysis of the desorption branch of the isotherm.

X-ray diffraction (XRD) patterns were recorded on a Bruker D8 Advance X-ray diffractometer using Cu K $\alpha$  radiation at room temperature at 40 kV and 40 mA. Data was collected with the 2 $\theta$  range of 10–90° at a step size of 0.02°.

#### 4.2.4 Electrochemical Evaluation

Electrochemical performance was evaluated using the standard 2032 button coin cells (MTI Corp). The produced nanofiber mats were directly used as the working electrode without adding any binder or conductor materials. These mats are mechanically

flexible and can be easily bent, folded, or rolled into spiral wound configuration (Figure 4-2). Lithium chips of 250  $\mu\text{m}$  in thickness (MTI Corp) and polypropylene membrane (Celgard, LLC) of 25  $\mu\text{m}$  in thickness were used as the counter electrode and separator, respectively. The electrolyte solution used in the tests was 1 M  $\text{LiPF}_6$  in 1:1 (v/v) EC:DEC. Coin cells were assembled in a high-purity argon-filled glove box. The galvanostatic charge/discharge characteristics were recorded with a MTI battery-testing system (model number BST8-WA) in a voltage range of 0.01-2.0 V with 50 mA/g current densities at room temperature.

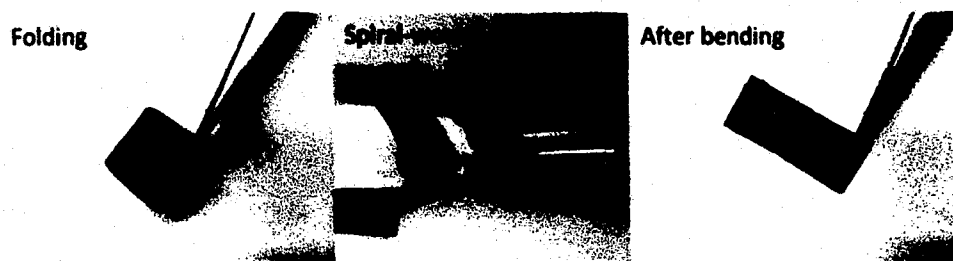


**Figure 4-2:** Optical images of the C/Si/AACA composite nanofibers under mechanical deformation (folding and spiral-wound bending) and after bending.

### 4.3 Results and Discussion

#### 4.3.1 Characterization of Porous C/Si/AACA Composites Nanofibers

The typical morphology of porous C/Si/AACA composites nanofibers, nonporous C/Si composites nanofibers, and CNFs alone were shown in Figure 4-3. In both Si-contained nanofibers (i.e., C/Si/AACA and C/Si composites nanofibers), the randomly distributed Si nanoparticle agglomerates were clearly seen on the nanofiber surface (Figures 4-3a-d). The pure CNFs and C/Si composite nanofibers show a taut and smooth surface structures (see Figures 4-3c-f) while the C/Si/AACA nanofibers have a rough and uneven surface. The wart like convex covered the entire surface of the composite

nanofibers (see Figure 4-3b). Many pores in the nanometer scale are clearly seen on the nanofibers when being checked under high magnification, which confirms the pore formation via AACA sublimation. To reveal the foaming occurrence moment, the morphology of PAN/Si/AACA nanofibers after the stabilization treatment was also examined and the results were shown in Figure 4-3g. Similar morphology (i.e., rough and uneven surface full of convex or pores) is also found there. Our additional AACA sublimation study on two dimensional PAN/Si/AACA composite thin films also confirms the presence of AACA coated Si nanoparticles before the thermal treatment and the pore formation after AACA sublimation. These evidences verify that the sublimation of AACA happened during the thermal stabilization step, and this sublimation-mediated foaming process successfully created the porous morphology in the nanofibers. Such foamed porous morphology also survived in the later carbonization step.

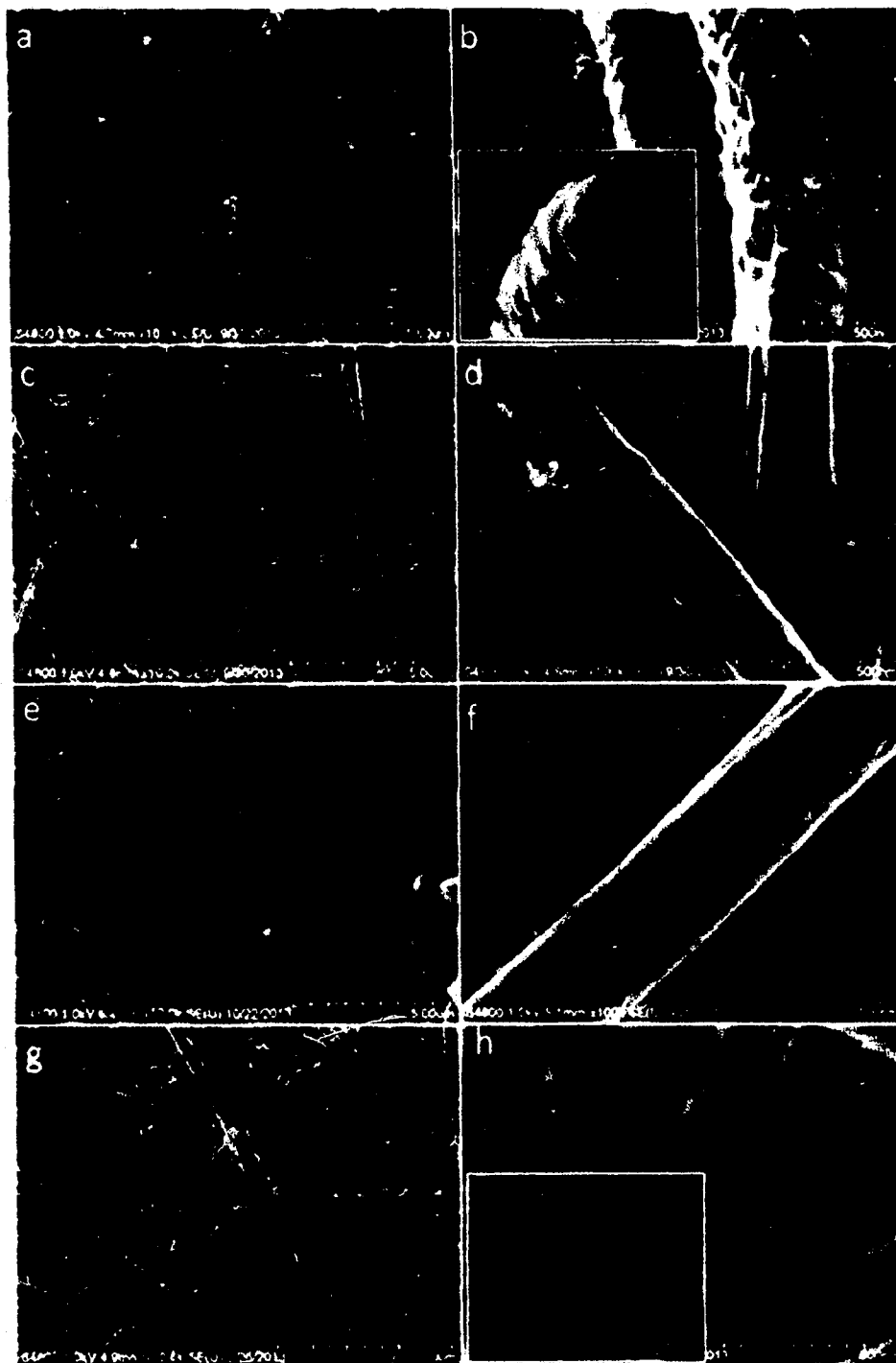


**Figure 4-3:** The SEM morphologies of porous C/Si/AACA composite nanofibers (a and b), nonporous C/Si composite nanofibers (c and d), pure CNFs (e and f), and PAN/Si/AACA composite nanofibers after the stabilization step (g and h).

The AACA sublimation was further confirmed by the TGA results. As shown in Figure 4-4, the TGA curve for PAN/Si/AACA composite nanofibers has a clear weight loss step between 150 and 200°C (close to the AACA sublimation temperature), which is not seen in the other two curves ( for PAN/Si composite nanofibers and pure PAN nanofibers, in which AACA is not present).

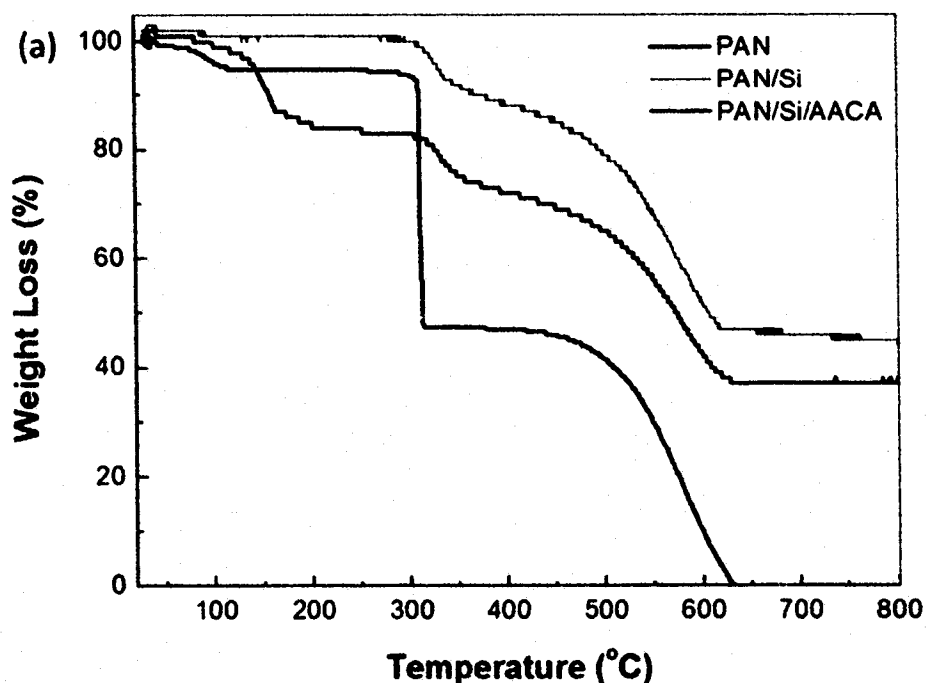


**Figure 4-4:** TGA results of PAN/Si/AACA composite nanofibers, nonporous PAN/Si/AACA composite nanofibers, and pure PAN nanofibers.

The weight loss percentage also matches closely enough to the weight of AACA introduced in the original PAN/Si/AACA electrospinning suspension. The nitrogen adsorption analysis provides further quantitative information on the surface and pore structure of these foamed composite nanofibers (Table 4-1).

**Table 4-1:** The surface and pore structure parameters of porous C/Si/AACA composite nanofibers, nonporous C/Si composite nanofibers and pure CNF.

| Sample | BET<br>Surface Area<br>(m <sup>2</sup> /g) | BJH Pore<br>Volume (ml/g) | BJH Pore<br>Diameter (nm) |
|--------|--|---------------------------|---------------------------|
| C/Si/A | 184  | 0.74                      | 2.9                       |
| C/Si   | 59   | 0.24                      | 2.4                       |
| C      | 56   | 0.12                      | 3.3                       |

The C/Si/AACA nanofibers has a BET surface area ~184 m<sup>2</sup>/g, which is three times high than that in C/Si nanofibers (59 m<sup>2</sup>/g) and pure CNFs (56 m<sup>2</sup>/g). The BJH pore volume of C/Si/AACA nanofibers was 0.74 ml/g, which is also much larger than that of C/Si nanofibers (0.24 ml/g) and pure CNFs (0.12 ml/g). Although BET method measures only the open pores while the foamed C/Si/AACA nanofibers should also contain many closed pores surrounding the embedded Si nanoparticles in the carbon matrix which are not accessible for BET measurement, these results, nonetheless, suggest that the sublimation of AACA effectively created more free volume and mesopores in the composite nanofibers.

Figure 4-5a showed the XRD patterns of the mesoporous C/Si/AACA composite nanofibers, nonporous C/Si composites nanofibers and CNFs alone. The diffraction peaks ( $2\theta = 28.4^\circ, 47.3^\circ, 56.1^\circ, 69.3^\circ, 76.5^\circ, \text{ and } 88.1^\circ$ ) are attributed to the Si cubic crystalline as detected in C/Si/AACA and C/Si composites nanofibers [114]. This confirmed that the crystalline structure is retained inside Si nanoparticles after carbonization. No clear graphene or crystalline carbon peaks are found in all nanofiber samples, indicating that carbon in nanofibers stays amorphous. The composition of C/Si/AACA nanofibers is



further measured by energy dispersive spectroscopy (EDS) microanalysis (Figure 4-5b). It shows strong signals of carbon and silicon (C: 69 wt%; Si: 24 wt%) with weak peaks of oxygen and aluminum (O: 4 wt%; Al: 2 wt%). Such composition analysis indicates that PAN nanofibers were carbonized completely and only residual AACA might be left in the final product. The ratio of carbon to silicon in composite nanofibers is about 2.9:1, slightly less than the original mixing ratio (i.e., 30%). As some weight loss is known to occur during the carbonization process, these results suggest the majority of Si nanoparticles were successfully encapsulated in carbon nanofibers during the electrospinning process. Our element mapping result on two-dimensional composite thin films further confirmed that Si nanoparticles dispersed well in polymer and later carbon matrix and no obvious aggregates of Si nanoparticles occurred during the carbonization process.

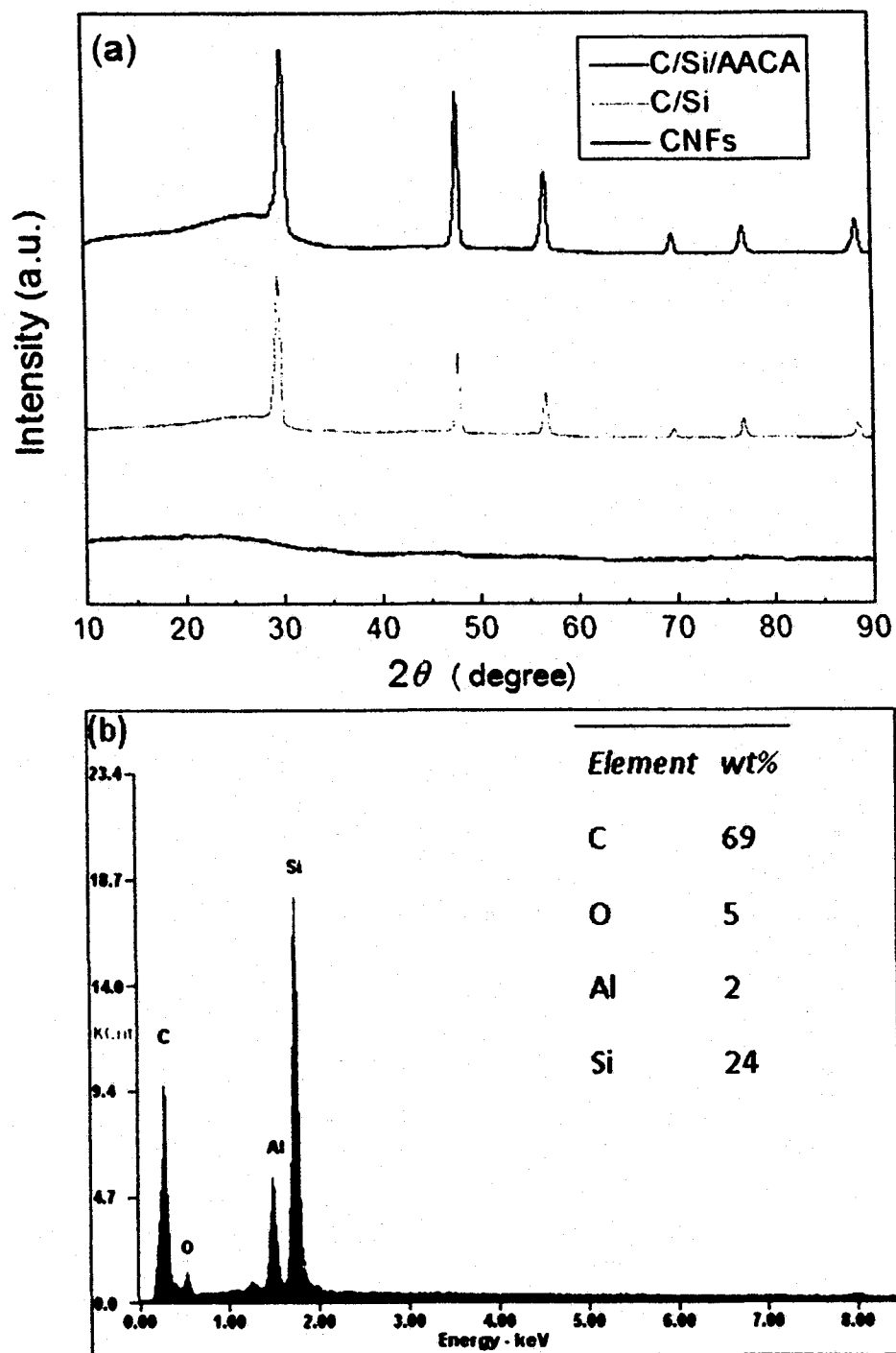


**Figure 4-5:** (a) XRD patterns of C/Si/AACA composite nanofibers along with nonporous C/Si composite nanofibers and pure CNFs; (b) EDS of porous C/Si/AACA composite nanofibers.

#### 4.3.2 Electrochemical Performance

The electrochemical performance of porous C/Si/AACA composite nanofibers, nonporous C/Si composite nanofibers and pure CNFs was done via galvanostatic charge/discharge experiments. Figure 4-6 shows the voltage profiles (plot of the potential against the capacity) at the end of the 1st, 2nd, 10th, and 20th galvanostatic charge/discharge cycles. Clearly, the presence of Si improves the Li storage capacity for anodes made of the composites nanofibers (both C/Si and C/Si/AACA nanofibers). For example, in the first cycle, the charge and discharge capacity of C/Si/AACA nanofibers reached 1961 mAh/g and 1639 mAh/g, respectively, with a coulombic efficiency (i.e., discharge capacity/charge capacity) of 83.6%. As a comparison, C/Si composites nanofibers anode showed 1856 mAh/g (charging) and 1532 mAh/g (discharging) and a coulombic efficiency of 82.5%. The anode made of pure CNFs had the lowest capacity, only 1310 mAh/g (charging)/823 mAh/g (discharging) and a coulombic efficiency of 62.8%. Here, the capacity is calculated based on the total mass of anode (i.e., including both carbon and Si).

Such capacity data in the first charge-discharge cycle is comparable to some early works using CNFs or C/Si composites as an anode (e.g. Ref. [134], in which the Si/C nanofiber anode with 15% Si was used and exhibited a charge and discharge capacity of 1541 mAh/g and 1281 mAh/g, respectively, and a coulombic efficiency of 83.1% when tested at a current density of 100 mAh/g). On the first charging curves for all three anodes, there is a small plateau around 0.75 V attributed to the decomposition of the electrolyte solution and the formation of solid electrolyte interface (SEI) [149, 150].

The second type of plateau appears on the charging-discharging curves from the second cycle. For the Si-contained anodes (C/Si and C/Si/AACA nanofibers), these plateaus show up at a charging voltage of  $\sim 0.25\text{V}$  and a discharging voltage of  $\sim 0.50\text{V}$ . It is attributed to the phase transformations between different Si-Li states during lithiation and delithiation processes[151, 152]. As carbon is amorphous in CNFs, their storage of Li mainly relies on the “adsorption” on the surface and inside the micropores of the carbon matrix. Therefore, this second plateau is not obvious for the CNFs sample in Figure 4-6. In addition, the current of the CNFs falls very close to the instrument limit of our battery-testing system ( $\sim 0.1\text{mA}$ ), which could quickly cut off the charge-discharge processes when they approach the common plateau potential of carbon materials ( $< 0.2\text{V}$ ). This makes the tails of galvanostatic charge-discharge curves for our CNFs samples shorter than some published data while their overall curve shape is similar[153].

Nonetheless, the anode made of pure CNFs has the fastest decay on this group of plateaus and the battery capacity, as clearly shown in Figure 4-6. Similar plateaus from the nonporous composite anode (i.e., C/Si nanofibers) also become much shorter after 10 cycles, while the ones from the porous composite anode (i.e., C/Si/AACA nanofibers) still retain the long, obvious plateau and a large percentage of capacity even after 20 cycles (which is even much better than that from the nonporous anode after only 10 cycles). This clearly shows the contribution of mesopores in the porous composite anode to the retention of Li storage capacity and the cycling stability of LIB.

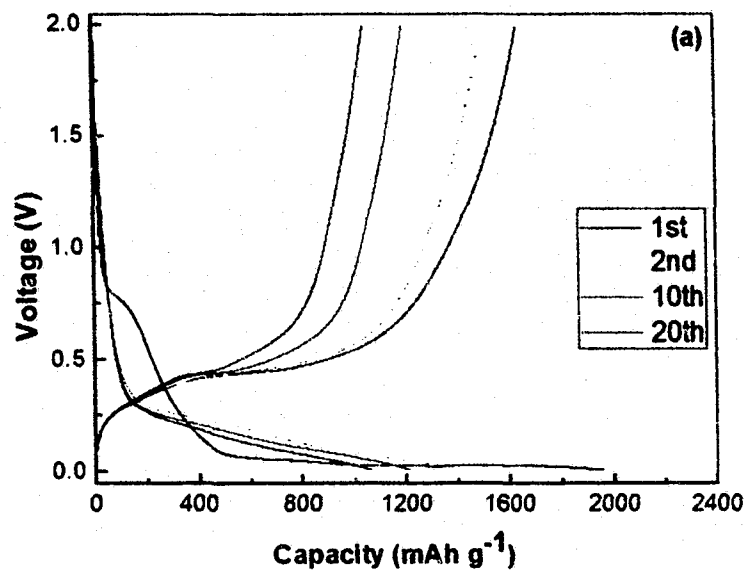


**Figure 4-6a:** The voltage profiles for the 1st, 2nd, 10th, and 20th galvanostatic charge-discharge cycles of porous C/Si/AACA composite nanofibers.

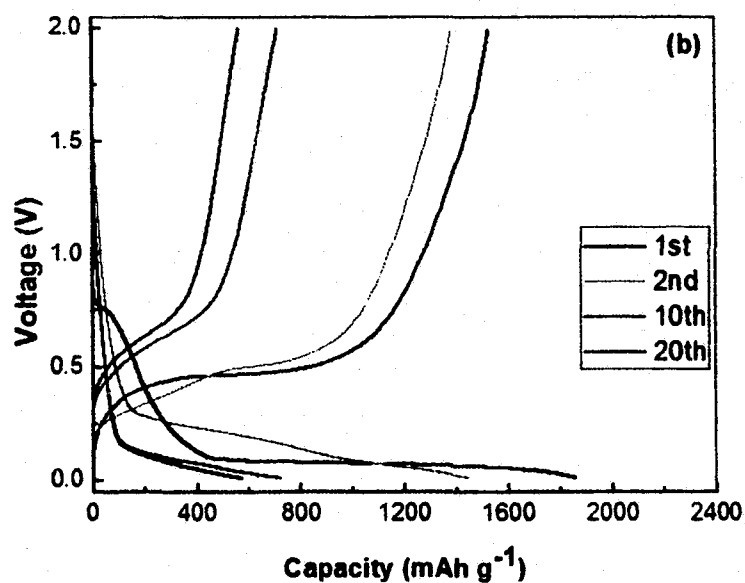


**Figure 4-6b:** The voltage profiles for the 1st, 2nd, 10th, and 20th galvanostatic charge-discharge cycles of nonporous C/Si composite nanofibers.

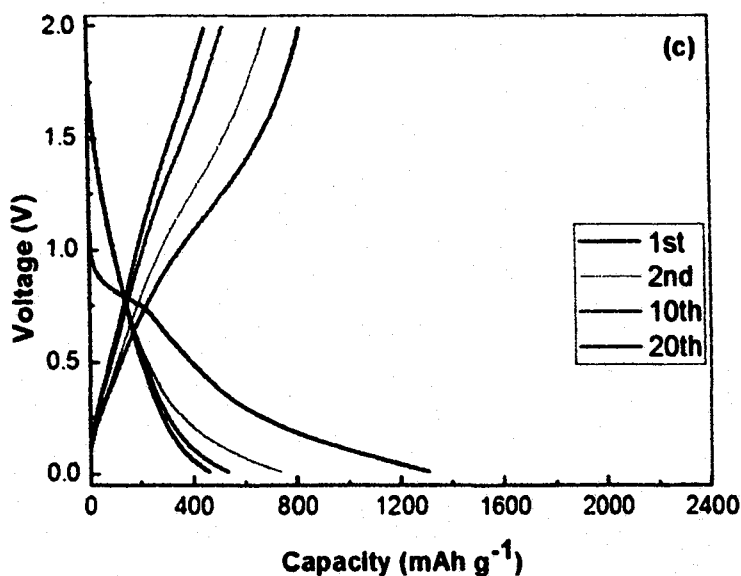


**Figure 4-6c:** The voltage profiles for the 1st, 2nd, 10th, and 20th galvanostatic charge-discharge cycles of porous pure CNFs.

The capacity loss can be better depicted in the cycling performance plots of LIBs, as shown in Figure 4-7. Like other carbon- or silicon-based anodes, gradual capacity loss is also found here for LIBs made from all three materials in the first few cycles. The pure CNFs LIBs has the capacity to fade fast as expected, reaching its stable discharging capacity of 594 mAh/g after only 5 cycles. The nonporous C/Si composites fiber LIBs follows as the second and their capacity reached stable after ~10 cycles. The porous C/Si/AACA composite nanofiber LIBs has the slowest decay rate after the initial capacity loss (with only 21% drop from cycle 3 to cycle 20). Over all cycles, the C/Si/AACA nanofiber LIB always retains the largest capacity among all three anode materials. For example, in the 10th cycle, the discharge capacity of C/Si/AACA composite nanofiber LIBs is 1119 mAh/g, ~73% of the maximum capacity while the pure CNFs and C/Si

composite nanofiber LIBs shows a discharge capacity of 526 mAh/g and 715 mAh/g, respectively.

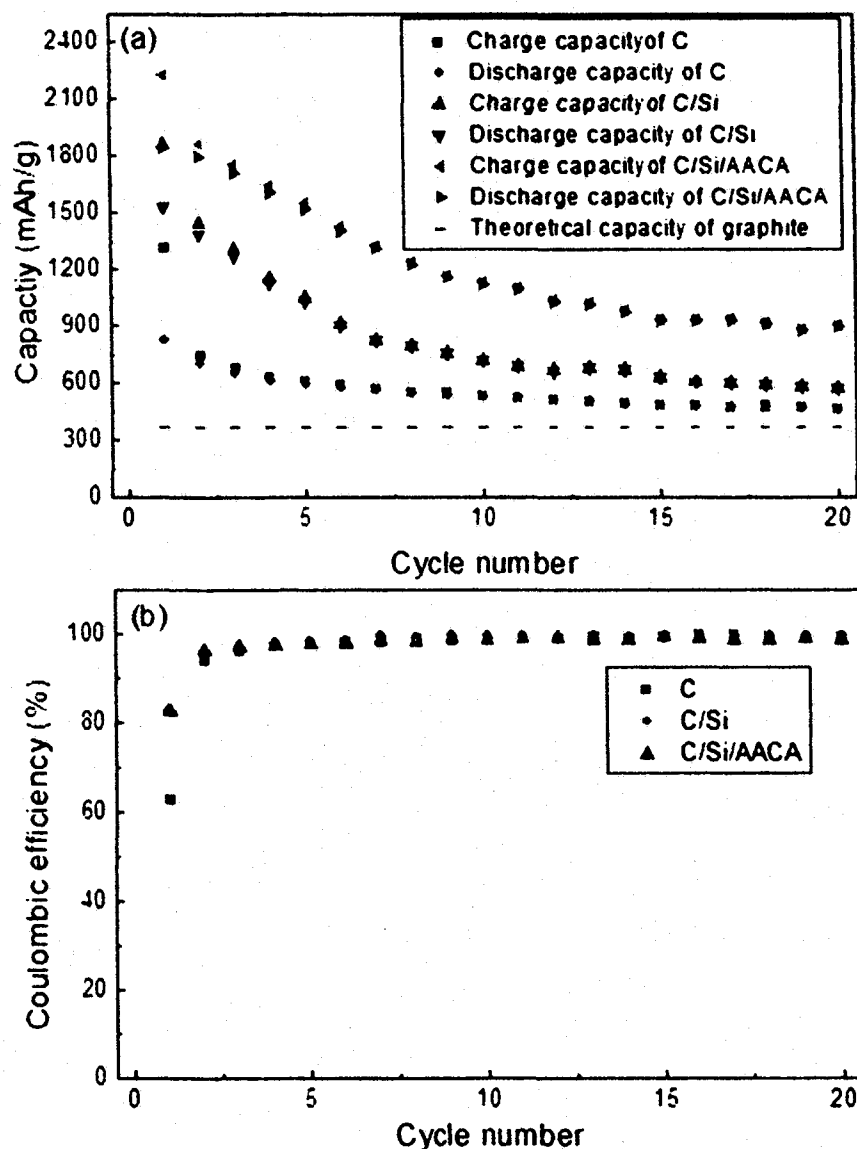


**Figure 4-7:** (a) The cycling performances of porous C/Si/AACA composite nanofibers, nonporous C/Si composite nanofibers, and pure CNFs. (b) The Coulombic efficiency of porous C/Si/AACA composite nanofibers, nonporous C/Si composite nanofibers, and pure CNFs.

After 20 cycles when all of these batteries reached a stable charging/discharging rate, the discharging capacity shows as 1045 mAh/g for porous C/Si/AACA composites

nanofibers, 569 mAh/g for nonporous C/Si composites nanofibers, and 438 mAh/g for pure CNFs, respectively. Low coulombic efficiency in several beginning cycles (cycle 1 in particular) is found due to the formation of solid electrolyte interface (SEI) over the electrode surface for the first time. The situation is more severe for pure CNFs anode with much lower coulombic efficiency than those made by composites nanofibers. This is consistent with observations in some pioneering investigations [154]. With the establishment of stable SEI, the coulombic efficiency quickly recovers to 99% and remained high afterwards for LIBs made of all three materials.

The presence of mesopores in C/Si/AACA composite nanofibers helps retain high reversible capacity as well as cycling stability. The discharging capacity of nonporous C/Si nanofiber LIBs settled on a value only slightly better than the pure CNFs, though both are still higher than the theoretical capacity of graphite (372 mAh/g).

As the Si content in C/Si composites nanofibers is confirmed to be nearly the same as their initial mixing ratio before the electrospinning process, this suggests that the introduction of Si nanoparticles alone does not efficiently improve the stable lithium intercalation capacity for carbon nanofiber based LIBs. The ineffectiveness lies on the compromise of nonporous nanofibers for higher capacity but worse for electrode pulverization. The situation gets significantly improved when mesopores are introduced in C/Si composite nanofiber anode because of their appropriate management of the volume expansion and induced stress during the alloying process. Only a very slow loss of capacity exists in these porous composite nanofiber LIBs, which is believed to be a mixed effect attributed to the slow increase of SEI thickness and the quality (non-uniform size) of dispersed silicon nanoparticles.



As many giant, micrometer sized particles present in our Si nanoparticle samples, their presence outside porous carbon nanofibers likely results in pulverization similar to those pure Si anode materials because of the big domain size. Heterogeneous pulverization situation could not be completely avoided here as the mesopores inside the nanofibers could not help mitigate all induced stress when Si particles are not embedded. Nonetheless, the electrochemical performance of C/Si/AACA nanofibers is superior to the nonporous C/Si nanofibers and pure CNFs because of their unique hybrid porous structure (Figure 4-8): the mesopores of CNFs provided buffering space to mitigate the induced stress in Si nanoparticles initialized by the volume change during the Li insertion and extraction; CNFs contributed the needed electrical conductivity during the charging/discharging process; macrovoids in the CNF mat promote Li ion transport between electrolytes and the active material surface[155-157]. As a result, both higher Li ion storage capacity and better cyclic stability are achieved with our porous C/Si/AACA composites nanofiber anode.

#### Buffering Volume Expansion During Li Insertion

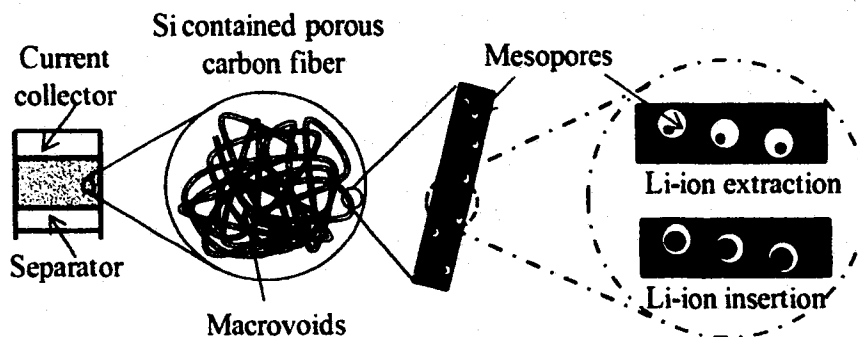


**Figure 4-8:** Accommodation mechanism of volume expansion and stress induction during Li ion insertion using incorporated mesopores.

The forming process adopted here offers a unique advantage in the production of C/Si composite nanofibers with desired porous structures. In polymer/clay composite foaming studies, it was found that silica filler nanoparticles served as the necessary nucleation sites during the foaming initialization [158, 159]. Therefore, we believe the Si nanoparticles in our C/Si composite nanofibers also play the same role (as the nucleation sites), particularly when AACA is sublimated, gas starts generating from the surface of Si nanoparticles, expands around particles, and eventually encapsulates them inside (Figure 4-8). Therefore, after foaming, Si nanoparticles are expected to be partially or completely shelled in the produced pores. Based on our own electrochemical results and other pioneer findings, Si surface when embedded in porous carbon is still accessible to Li-ions [160].

Therefore, our mesoporous C/Si composite nanofibers allow efficient Li insertion; while simultaneously provide buffering space for the lithiated silicon to expand their volume. Such unique porous structure design (i.e., having Si particles encapsulated in closed mesopores) not only helps manage the induced stress of Si particles during the lithiation process, but also avoids their direct contact to electrolytes to minimize undesired electrolyte decomposition and maintain stable SEI thickness. This is quite different from some other approaches in porous composite nanofiber production, in which pores are created from the space left by the randomly dispersed immiscible polymer or inorganic nanoparticles and their accessibility to Si is largely set on a random basis (i.e., when both materials happen to stay together).

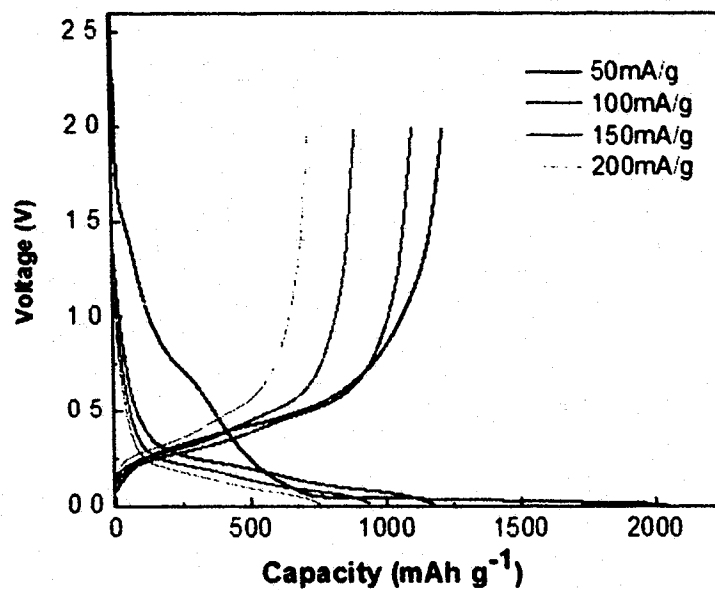
As foaming is allowed to start from the surface of every nanoparticle, the generated “gas cushion” could separate Si nanoparticles away from each other in

nanofibers. This helps avoid the formation of Si particle aggregates (i.e., large silicon domains) in carbon matrix that often results in capacity loss (Figure 4-8). Moreover, as some AACA are pre-coated on Si nanoparticles, its good compatibility (Note: AACA can be dissolved in DMF) to the PAN solution caused less impact to the viscosity of the electrospinning fluid when Si nanoparticles are introduced, beneficial for no addition of manufacturing challenges. Its sublimation foaming mechanism also keeps the pore formation a very simple process and no need for further removal of the sacrificial nanomaterials (polymer or inorganic nanoparticles). The appropriate sublimating temperature of AACA, close to that used in electrospun nanofiber stabilization, also conveniently avoids possible collapsed nanofibers or nanofibers with reduced mechanical strength. All of these facts make this foaming and electrospinning a good manufacturing process (GMP) for C/Si composite nanofiber production.

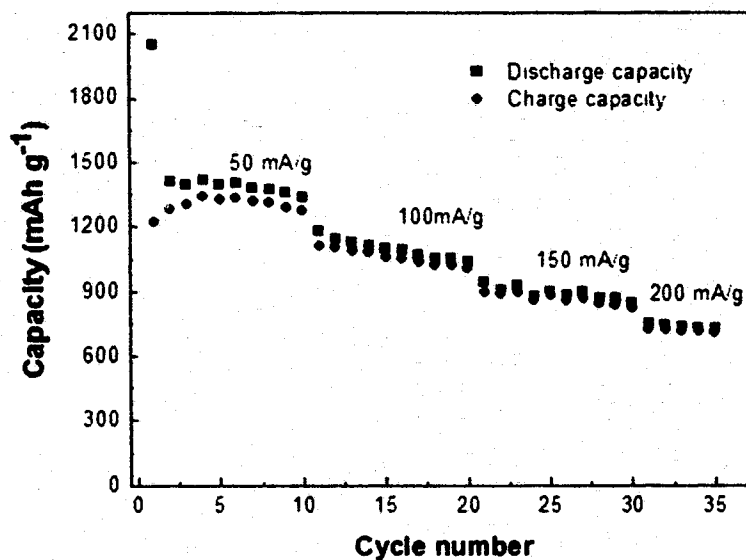
#### 4.3.3 Measurement at Different Current Density

Figure 4-9a shows the voltage profiles for anodes made by composites nanofibers (C/Si/AACA nanofibers) at different current density. It could be clearly found that at 50 mA current density, the battery performed the maximum capacity. For example, at 50 mA current density, the charge and discharge capacity of C/Si/AACA nanofibers reached above 2000 mAh/g and 1200 mAh/g, respectively. As a comparison, at other current density, the anode showed below 1200 mAh/g (charging) and 1100 mAh/g (discharging). There was a small plateau on the charging curve around 0.75 V for the 50 mA current density, which is attributed to the irreversibly reductive decomposition of the electrolyte solution when the solid electrolyte interface (SEI) formed over electrode surface for the first time and Li ions were intercalated into electrodes [149, 150]. The

cycling performance of LIBs made of these nanofibers at different current density is shown in Figure 4-9b. Besides the obvious capacity loss at 50 mA current density in the first few cycles, the capacity fading are almost stable over all cycles at different current density.



**Figure 4-9a:** Voltage profiles for anodes made by composites nanofibers (C/Si/AACA nanofibers) at different current density.



**Figure 4-9b:** The cycling performance of LIBs made of these nanofibers at different current density.

#### 4.4 Conclusions

Mesoporous polymer/Si composite nanofibers were successfully produced by electrospinning polyacrylonitrile (PAN)/silicon nanoparticles suspension solution, followed by sublimation of AACA coated on silicon nanoparticles during later thermal treatment. After carbonization at 700°C, C/Si fibrous composites were formed. Compared with those nonporous C/Si composite nanofibers and CNFs alone which were prepared in a similar way, these mesoporous C/Si/AACA composite nanofibers showed higher energy, higher power density and better cycling performance when used as the anode of LIBs.

## **CHAPTER 5**

### **CONCLUSIONS AND FUTURE WORK**

#### **5.1 Conclusions**

In this dissertation, PAN solutions of various concentrations were used to produce long, continuous nanofibers and nanowires with two different flow-guided assembly processes. PAN was chosen here because of the existing well-developed technology for its conversion to conductive carbon, which is the active materials of the two applications explored in this dissertation: electrochemical sensors and electrode for lithium-ion batteries.

In the first project, a gas-blowing based flow guided assembly process was successfully developed to pattern and well align polymer nanowires accurately in desired locations on a large scale. The actual nanowire quality and dimensions depend on the used polymer concentration and the applied gas flow rate. After further carbonization, the electrochemical sensors built on the produced nanowires showed pico-gram sensitivity of BSA protein. With this new approach, the synthesis, alignment, and patterning of nanowire arrays can be done in a reliable manner with high throughput. This would be of great engineering value to nanowire manufacturing community and may open the door to many important nanowire-based detection applications in clinical diagnosis, environmental monitoring, security screening, and biowarfare caution.

In the second project, the same polymer materials, PAN was used to produce mesoporous carbon/silicon fibrous composites as the anode materials of LIBs. By introducing sublimable forming agent, aluminum acetylacetonate AACA, into PAN/Si solution, mesoporous C/Si/AACA composites nanofibers were prepared through a low-cost and high-throughput electrospinning/foaming process. As AACA can concurrently sublimate during the later thermal stabilization process, no additional chemical or physics treatments are required in the production of pores in composite nanofibers. The resulting mesopores provide free space to accommodate the volume expansion and the consequent stress within electrode materials during the alloying process so that issues like electrode pulverization could be mitigated effectively.

The unique porous structure with embedded Si nanoparticles further prevents their direct exposure to electrolytes to minimize undesired decomposition and the macrovoids in carbon matrix promotes Li ion transport between electrolytes and the active materials. The resulting porous C/Si/AACA nanofibers exhibited larger lithium capacity and better cycling stability when compared with the nonporous C/Si composite nanofibers and pure CNFs as the LIBs anode. The combination of foaming and electrospinning process offers a new scalable route to manufacture porous nanomaterial anode for LIBs with promising electrochemical performance to help move forward their commercialization.

## 5.2 Future Work

For flow-guided assembly carbon nanowire project, our results have shown that the FET sensors made by perfectly aligned and well-patterned nanowire strands have high sensitivity for model protein, BSA. We expect the same high detecting sensitivity on other proteins and a variety of other biological probes. For example, it is worthy to



investigate the sensing performance of our nanowire FET sensors on the identification or quantification of some cancer marker proteins at ultralow concentrations. For example, prostate specific antigen (PSA), such as PSA-a-antichymotrypsin (PSA-ACT) complex and carcinoembryonic antigen (CEA), are two important ones for prostate cancers [161] and are suggested for testing in our nanowire-FET devices. These PSA proteins are importance for early diagnosis of cancers, which in return could help increase the survival rate of patient. Besides protein detection, the same sensor setup might be useful in the detection of nucleic acids, viruses, glucose and other biologically relevant molecules as long as there are some electron concentration changes in the electrical double layer when they are attached or present on the surface of nanowire array.

For nanowire with more sophisticated “T shape” and “Cross shape” junctions, they should also be integrated into sensing devices to evaluate their unique I-V curves and characteristic conductance and conductance gradient. They can also be used as an excellent model system to study the cross-talk issues or the misalignment degree in common nanowire sensors.

For the project on porous C/Si/AACA nanofibers, the maximum allowed weight percentage of silicon content in PAN/Si/AACA solution is ~30% due to the strong interactions of PAN and silicon and the rapid increase on the viscosity of the processing fluid when adding more silicon nanoparticles. Other polymers such as Poly (vinyl alcohol) or PVA can be used as PAN replacement due to their high allowing silicon content (>70%) and similar nanofiber quality after carbonization. With PVA, the Si/C ratio can vary in a broad range in the produced mesoporous C/Si/AACA composite nanofibers. Besides the Si/C ratio, the coating quality and quantity of AACA on silicon nanoparticles

will also be investigated. The relationship of the addition of AACA and the resulting pore size and porosity will be established. The optimal ratios of Si-to-AACA, Si-to-polymer in solution and the appropriate process window will be identified based on their electrochemical performance in later battery tests.

## BIBLIOGRAPHY

1. Banks, C.E. and R.G. Compton, *Edge plane pyrolytic graphite electrodes in electroanalysis: an overview*. Analytical Sciences, 2005. **21**(11): p. 1263-1268.
2. Janata, J. and M. Josowicz, *Conducting polymers in electronic chemical sensors*. Nature Materials, 2003. **2**(1): p. 19-24.
3. Kang, G., J. Park, S. Kim, J. Koo, J. Park, Y.-S. Sohn, and Y. Kim, *Fabrication and characterisation of CMOS compatible silicon nanowire biosensor*. Electronics Letters, 2008. **44**(16): p. 953-955.
4. Sondheimer, E.H., *The mean free path of electrons in metals*. Advances in physics, 2001. **50**(6): p. 499-537.
5. Patolsky, F., G. Zheng, and C.M. Lieber, *Nanowire-based biosensors*. Analytical Chemistry, 2006. **78**(13): p. 4260-4269.
6. Chen, R.J., S. Bangsaruntip, K.A. Drouvalakis, N.W.S. Kam, M. Shim, Y. Li, W. Kim, P.J. Utz, and H. Dai, *Noncovalent functionalization of carbon nanotubes for highly specific electronic biosensors*. Proceedings of the National Academy of Sciences, 2003. **100**(9): p. 4984-4989.
7. Star, A., E. Tu, J. Niemann, J.-C.P. Gabriel, C.S. Joiner, and C. Valcke, *Label-free detection of DNA hybridization using carbon nanotube network field-effect transistors*. Proceedings of the National Academy of Sciences of the United States of America, 2006. **103**(4): p. 921-926.
8. Minetti, C.A., D.P. Remeta, H. Miller, C.A. Gelfand, G.E. Plum, A.P. Grollman, and K.J. Breslauer, *The thermodynamics of template-directed DNA synthesis: Base insertion and extension enthalpies*. Proceedings of the National Academy of Sciences, 2003. **100**(25): p. 14719-14724.
9. St-Antoine, B.C., D. Ménard, and R. Martel, *Photothermoelectric effects in single-walled carbon nanotube films: Reinterpreting scanning photocurrent experiments*. Nano Research, 2012. **5**(2): p. 73-81.
10. Favier, F., E.C. Walter, M.P. Zach, T. Benter, and R.M. Penner, *Hydrogen sensors and switches from electrodeposited palladium mesowire arrays*. Science, 2001. **293**(5538): p. 2227-2231.

11. Murray, B.J., E.C. Walter, and R.M. Penner, *Amine vapor sensing with silver mesowires*. Nano Letters, 2004. 4(4): p. 665-670.
12. Cui, Y., Q. Wei, H. Park, and C.M. Lieber, *Nanowire nanosensors for highly sensitive and selective detection of biological and chemical species*. Science, 2001. 293(5533): p. 1289-1292.
13. Cheng, G. and L. Zhang, *hen, Y. Li, L. Li, XG Zhu, Y. Zhu, GT Fei and YQ Mao*. J. Mater. Res, 2000. 15: p. 137.
14. Xia, Y., P. Yang, Y. Sun, Y. Wu, B. Mayers, B. Gates, Y. Yin, F. Kim, and H. Yan, *One-dimensional nanostructures: synthesis, characterization, and applications*. Advanced Materials, 2003. 15(5): p. 353-389.
15. Ren, Z., Z. Huang, D. Wang, J. Wen, J. Xu, J. Wang, L. Calvet, J. Chen, J. Klemic, and M. Reed, *Growth of a single freestanding multiwall carbon nanotube on each nanonickel dot*. Applied Physics Letters, 1999. 75(8): p. 1086-1088.
16. Spatz, J.P., B. Lorenz, K. Weishaupt, H.D. Hochheimer, V. Menon, R. Parthasarathy, C.R. Martin, J. Bechtold, and P.-H. Hor, *Observation of crossover from three-to two-dimensional variable-range hopping in template-synthesized polypyrrole and polyaniline*. Physical Review B, 1994. 50(20): p. 14888.
17. Liang, L., J. Liu, C.F. Windisch Jr, G.J. Exarhos, and Y. Lin, *Direct assembly of large arrays of oriented conducting polymer nanowires*. Angewandte Chemie International Edition, 2002. 41(19): p. 3665-3668.
18. Che, G., B.B. Lakshmi, E.R. Fisher, and C.R. Martin, *Carbon nanotubule membranes for electrochemical energy storage and production*. Nature, 1998. 393(6683): p. 346-349.
19. Wagner, R. and W. Ellis, *Vapor - liquid - solid mechanism of single crystal growth*. Applied Physics Letters, 1964: p. 89-90.
20. Huang, J., X. Luo, I. Lee, Y. Hu, X.T. Cui, and M. Yun, *Rapid real-time electrical detection of proteins using single conducting polymer nanowire-based microfluidic aptasensor*. Biosensors and Bioelectronics, 2011. 30(1): p. 306-309.
21. Tao, A., F. Kim, C. Hess, J. Goldberger, R. He, Y. Sun, Y. Xia, and P. Yang, *Langmuir-Blodgett silver nanowire monolayers for molecular sensing using surface-enhanced Raman spectroscopy*. Nano Letters, 2003. 3(9): p. 1229-1233.
22. Fan, Z., J.C. Ho, T. Takahashi, R. Yerushalmi, K. Takei, A.C. Ford, Y.L. Chueh, and A. Javey, *Toward the development of printable nanowire electronics and sensors*. Advanced Materials, 2009. 21(37): p. 3730-3743.

23. Smith, P.A., C.D. Nordquist, T.N. Jackson, T.S. Mayer, B.R. Martin, J. Mbindyo, and T.E. Mallouk, *Electric-field assisted assembly and alignment of metallic nanowires*. Applied Physics Letters, 2000. 77(9): p. 1399.
24. Duan, X., Y. Huang, Y. Cui, J. Wang, and C.M. Lieber, *Indium phosphide nanowires as building blocks for nanoscale electronic and optoelectronic devices*. Nature, 2001. 409(6816): p. 66-69.
25. Hangarter, C.M. and N.V. Myung, *Magnetic alignment of nanowires*. Chemistry of materials, 2005. 17(6): p. 1320-1324.
26. Huang, Y., X. Duan, Q. Wei, and C.M. Lieber, *Directed assembly of one-dimensional nanostructures into functional networks*. Science, 2001. 291(5504): p. 630-633.
27. Yu, G., A. Cao, and C.M. Lieber, *Large-area blown bubble films of aligned nanowires and carbon nanotubes*. Nature Nanotechnology, 2007. 2(6): p. 372-377.
28. Chen, J., Y. Zu, K.K. Rajagopalan, and S. Wang, *Scalable Nanomanufacturing of Nanowire based Sensing Systems from Integrating Flow-guided Assembly and Synthesis*. Nanotechnology, 2015. 26(23)
29. Yao, J., H. Yan, and C.M. Lieber, *A nanoscale combing technique for the large-scale assembly of highly aligned nanowires*. Nature Nanotechnology, 2013. 8(5): p. 329-335.
30. Guan, J. and L.J. Lee, *Generating highly ordered DNA nanostrand arrays*. Proceedings of the National Academy of Sciences of the United States of America, 2005. 102(51): p. 18321-18325.
31. Guan, J., B. Yu, and L.J. Lee, *Forming highly ordered arrays of functionalized polymer nanowires by dewetting on micropillars*. Advanced Materials, 2007. 19(9): p. 1212-1217.
32. Wang, S., J. Guan, and L.J. Lee, *Flow - Guided Assembly Processes*. Chem Phys Chem, 2008. 9(7): p. 967-973.
33. Arsenault, A. and G.A. Ozin, *Nanochemistry: A chemical approach to nanomaterials*. RSC, Cambridge, 2005.
34. Wang, D., M.P. Gil, G. Lu, and Y. Lu, *Nanostructured systems from low-dimensional building blocks*. Nanofabrication Towards Biomedical Applications: Techniques, Tools, Applications, and Impact, 2005. 26: p. 28.
35. Yu, G., X. Li, C.M. Lieber, and A. Cao, *Nanomaterial-incorporated blown bubble films for large-area, aligned nanostructures*. Journal of Materials Chemistry, 2008. 18(7): p. 728-734.

36. Rogers, J.A., *Stamping techniques for micro and nanofabrication: methods and applications*, in *Springer Handbook of Nanotechnology*. 2004, Springer. p. 185-202.
37. Yerushalmi, R., Z.A. Jacobson, J.C. Ho, Z. Fan, and A. Javey, *Large scale, highly ordered assembly of nanowire parallel arrays by differential roll printing*. *Applied Physics Letters*, 2007. **91**(20): p. 203104.
38. Bae, S., H. Kim, Y. Lee, X. Xu, J.-S. Park, Y. Zheng, J. Balakrishnan, T. Lei, H.R. Kim, and Y.I. Song, *Roll-to-roll production of 30-inch graphene films for transparent electrodes*. *Nature Nanotechnology*, 2010. **5**(8): p. 574-578.
39. Fan, Z., J.C. Ho, Z.A. Jacobson, R. Yerushalmi, R.L. Alley, H. Razavi, and A. Javey, *Wafer-scale assembly of highly ordered semiconductor nanowire arrays by contact printing*. *Nano Letters*, 2008. **8**(1): p. 20-25.
40. Fan, Z., J.C. Ho, Z.A. Jacobson, H. Razavi, and A. Javey, *Large-scale, heterogeneous integration of nanowire arrays for image sensor circuitry*. *Proceedings of the National Academy of Sciences*, 2008. **105**(32): p. 11066-11070.
41. Kim, Y.-K., S.J. Park, J.P. Koo, D.-J. Oh, G.T. Kim, S. Hong, and J.S. Ha, *Controlled direct patterning of V2O5 nanowires onto SiO2 substrates by a microcontact printing technique*. *Nanotechnology*, 2006. **17**(5): p. 1375.
42. Kim, Y.-K., S.J. Park, J.P. Koo, G.T. Kim, S. Hong, and J.S. Ha, *Control of adsorption and alignment of V2O5 nanowires via chemically functionalized patterns*. *Nanotechnology*, 2007. **18**(1): p. 015304.
43. Hannon, J., A. Afzali, C. Klinke, and P. Avouris, *Selective placement of carbon nanotubes on metal-oxide surfaces*. *Langmuir*, 2005. **21**(19): p. 8569-8571.
44. Ahn, J.-H., H.-S. Kim, K.J. Lee, S. Jeon, S.J. Kang, Y. Sun, R.G. Nuzzo, and J.A. Rogers, *Heterogeneous three-dimensional electronics by use of printed semiconductor nanomaterials*. *Science*, 2006. **314**(5806): p. 1754-1757.
45. Javey, A., S. Nam, R.S. Friedman, H. Yan, and C.M. Lieber, *Layer-by-layer assembly of nanowires for three-dimensional, multifunctional electronics*. *Nano Letters*, 2007. **7**(3): p. 773-777.
46. Yang, P., *Nanotechnology: Wires on water*. *Nature*, 2003. **425**(6955): p. 243-244.
47. Whang, D., S. Jin, Y. Wu, and C.M. Lieber, *Large-scale hierarchical organization of nanowire arrays for integrated nanosystems*. *Nano Letters*, 2003. **3**(9): p. 1255-1259.

48. Jin, S., D. Whang, M.C. McAlpine, R.S. Friedman, Y. Wu, and C.M. Lieber, *Scalable interconnection and integration of nanowire devices without registration*. Nano Letters, 2004. 4(5): p. 915-919.
49. Wang, D., Y.-L. Chang, Z. Liu, and H. Dai, *Oxidation resistant germanium nanowires: Bulk synthesis, long chain alkanethiol functionalization, and Langmuir-Blodgett assembly*. Journal of the American Chemical Society, 2005. 127(33): p. 11871-11875.
50. Li, X., L. Zhang, X. Wang, I. Shimoyama, X. Sun, W.-S. Seo, and H. Dai, *Langmuir-Blodgett assembly of densely aligned single-walled carbon nanotubes from bulk materials*. Journal of the American Chemical Society, 2007. 129(16): p. 4890-4891.
51. Park, J., G. Shin, and J.S. Ha, *Thickness and density controllable pattern transfer of DODAB/V2O5 nanowire hybrid film*. Nanotechnology, 2007. 18(40): p. 405301.
52. Kim, F., S. Kwan, J. Akana, and P. Yang, *Langmuir-Blodgett nanorod assembly*. Journal of the American Chemical Society, 2001. 123(18): p. 4360-4361.
53. Messer, B., J.H. Song, and P. Yang, *Microchannel networks for nanowire patterning*. Journal of the American Chemical Society, 2000. 122(41): p. 10232-10233.
54. Wang, D., R. Tu, L. Zhang, and H. Dai, *Deterministic One - to - One Synthesis of Germanium Nanowires and Individual Gold Nanoseed Patterning for Aligned Nanowire Arrays*. Angewandte Chemie International Edition, 2005. 44(19): p. 2925-2929.
55. Xin, H. and A.T. Woolley, *Directional orientation of carbon nanotubes on surfaces using a gas flow cell*. Nano Letters, 2004. 4(8): p. 1481-1484.
56. Meitl, M.A., Y. Zhou, A. Gaur, S. Jeon, M.L. Usrey, M.S. Strano, and J.A. Rogers, *Solution casting and transfer printing single-walled carbon nanotube films*. Nano Letters, 2004. 4(9): p. 1643-1647.
57. Myung, S., J. Im, L. Huang, S.G. Rao, T. Kim, D.J. Lee, and S. Hong, *"Lens" effect in directed assembly of nanowires on gradient molecular patterns*. The Journal of Physical Chemistry B, 2006. 110(21): p. 10217-10219.
58. Wang, Y., D. Maspoch, S. Zou, G.C. Schatz, R.E. Smalley, and C.A. Mirkin, *Controlling the shape, orientation, and linkage of carbon nanotube features with nano affinity templates*. Proceedings of the National Academy of Sciences of the United States of America, 2006. 103(7): p. 2026-2031.
59. Rao, S.G., L. Huang, W. Setyawan, and S. Hong, *Nanotube electronics: large-scale assembly of carbon nanotubes*. Nature, 2003. 425(6953): p. 36-37.

60. Kang, J., S. Myung, B. Kim, D. Oh, G.T. Kim, and S. Hong, *Massive assembly of ZnO nanowire-based integrated devices*. *Nanotechnology*, 2008. **19**(9): p. 095303.
61. Boote, J., K. Critchley, and S. Evans, *Surfactant mediated assembly of gold nanowires on surfaces*. *Journal of Experimental Nanoscience*, 2006. **1**(2): p. 125-142.
62. Lee, M., J. Im, B. Lee, S. Myung, J. Kang, L. Huang, Y.-K. Kwon, and S. Hong, *Linker-free directed assembly of high-performance integrated devices based on nanotubes and nanowires*. *Nature Nanotechnology*, 2006. **1**(1): p. 66-71.
63. Thomas, K.G., S. Barazzouk, B.I. Ipe, S.S. Joseph, and P.V. Kamat, *Uniaxial plasmon coupling through longitudinal self-assembly of gold nanorods*. *The Journal of Physical Chemistry B*, 2004. **108**(35): p. 13066-13068.
64. Caswell, K., J.N. Wilson, U.H. Bunz, and C.J. Murphy, *Preferential end-to-end assembly of gold nanorods by biotin-streptavidin connectors*. *Journal of the American Chemical Society*, 2003. **125**(46): p. 13914-13915.
65. Gole, A. and C.J. Murphy, *Polyelectrolyte-coated gold nanorods: synthesis, characterization and immobilization*. *Chemistry of Materials*, 2005. **17**(6): p. 1325-1330.
66. Nikoobakht, B. and M.A. El-Sayed, *Evidence for bilayer assembly of cationic surfactants on the surface of gold nanorods*. *Langmuir*, 2001. **17**(20): p. 6368-6374.
67. Gole, A. and C.J. Murphy, *Biotin-streptavidin-induced aggregation of gold nanorods: tuning rod-rod orientation*. *Langmuir*, 2005. **21**(23): p. 10756-10762.
68. Gole, A., C.J. Orendorff, and C.J. Murphy, *Immobilization of gold nanorods onto acid-terminated self-assembled monolayers via electrostatic interactions*. *Langmuir*, 2004. **20**(17): p. 7117-7122.
69. Orendorff, C.J., P.L. Hankins, and C.J. Murphy, *pH-triggered assembly of gold nanorods*. *Langmuir*, 2005. **21**(5): p. 2022-2026.
70. Pan, B., D. Cui, C. Ozkan, P. Xu, T. Huang, Q. Li, H. Chen, F. Liu, F. Gao, and R. He, *DNA-templated ordered array of gold nanorods in one and two dimensions*. *The Journal of Physical Chemistry C*, 2007. **111**(34): p. 12572-12576.
71. Hu, X., W. Cheng, T. Wang, E. Wang, and S. Dong, *Well-ordered end-to-end linkage of gold nanorods*. *Nanotechnology*, 2005. **16**(10): p. 2164.
72. Li, L.-s. and A.P. Alivisatos, *Semiconductor nanorod liquid crystals and their assembly on a substrate*. *Advanced Materials*, 2003. **15**(5): p. 408-411.



73. Nikoobakht, B., Z. Wang, and M. El-Sayed, *Self-assembly of gold nanorods*. The Journal of Physical Chemistry B, 2000. **104**(36): p. 8635-8640.
74. Jana, N.R., L.A. Gearheart, S.O. Obare, C.J. Johnson, K.J. Edler, S. Mann, and C.J. Murphy, *Liquid crystalline assemblies of ordered gold nanorods*. J. Mater. Chem., 2002. **12**(10): p. 2909-2912.
75. Guerrero - Martínez, A., J. Pérez - Juste, E. Carbó - Argibay, G. Tardajos, and L.M. Liz - Marzán, *Gemini - Surfactant - Directed Self - Assembly of Monodisperse Gold Nanorods into Standing Superlattices*. Angewandte Chemie International Edition, 2009. **48**(50): p. 9484-9488.
76. Chen, M., L. Guo, R. Ravi, and P.C. Searson, *Kinetics of receptor directed assembly of multisegment nanowires*. The Journal of Physical Chemistry B, 2006. **110**(1): p. 211-217.
77. Dumestre, F., B. Chaudret, C. Amiens, M. Respaud, P. Fejes, P. Renaud, and P. Zurcher, *Unprecedented Crystalline Super - Lattices of Monodisperse Cobalt Nanorods*. Angewandte Chemie International Edition, 2003. **42**(42): p. 5213-5216.
78. Li, L.-s., J. Walda, L. Manna, and A.P. Alivisatos, *Semiconductor nanorod liquid crystals*. Nano Letters, 2002. **2**(6): p. 557-560.
79. Chang, Y. and H.C. Zeng, *Controlled synthesis and self-assembly of single-crystalline CuO nanorods and nanoribbons*. Crystal Growth & Design, 2004. **4**(2): p. 397-402.
80. Park, S., J.-H. Lim, S.-W. Chung, and C.A. Mirkin, *Self-assembly of mesoscopic metal-polymer amphiphiles*. Science, 2004. **303**(5656): p. 348-351.
81. Chen, D. and L. Gao, *Large-scale growth and end-to-end assembly of silver nanorods by PVP-directed polyol process*. Journal of Crystal Growth, 2004. **264**(1): p. 216-222.
82. Wang, M.-H., Y.-J. Li, Z.-X. Xie, C. Liu, and E.S. Yeung, *Fabrication of large-scale one-dimensional Au nanochain and nanowire networks by interfacial self-assembly*. Materials Chemistry and Physics, 2010. **119**(1): p. 153-157.
83. Li, Y.J., W.J. Huang, and S.G. Sun, *A Universal Approach for the Self - Assembly of Hydrophilic Nanoparticles into Ordered Monolayer Films at a Toluene/Water Interface*. Angewandte Chemie International Edition, 2006. **45**(16): p. 2537-2539.
84. Xie, J., Q. Zhang, J.Y. Lee, and D.I. Wang, *General method for extended metal nanowire synthesis: ethanol induced self-assembly*. The Journal of Physical Chemistry C, 2007. **111**(46): p. 17158-17162.

85. Yun, S., Y.-K. Park, S.K. Kim, and S. Park, *Linker-molecule-free gold nanorod layer-by-layer films for surface-enhanced Raman scattering*. *Analytical Chemistry*, 2007. **79**(22): p. 8584-8589.
86. Reincke, F., S.G. Hickey, W.K. Kegel, and D. Vanmaekelbergh, *Spontaneous assembly of a monolayer of charged gold nanocrystals at the water/oil interface*. *Angewandte Chemie International Edition*, 2004. **43**(4): p. 458-462.
87. Murphy, C.J. and C.J. Orendorff, *Alignment of gold nanorods in polymer composites and on polymer surfaces*. *Advanced Materials*, 2005. **17**(18): p. 2173-2176.
88. Correa - Duarte, M.A., J. Pérez - Juste, A. Sánchez - Iglesias, M. Giersig, and L.M. Liz - Marzán, *Aligning Au nanorods by using carbon nanotubes as templates*. *Angewandte Chemie International Edition*, 2005. **44**(28): p. 4375-4378.
89. Huang, J., R. Fan, S. Connor, and P. Yang, *One - Step Patterning of Aligned Nanowire Arrays by Programmed Dip Coating*. *Angewandte Chemie*, 2007. **119**(14): p. 2466-2469.
90. Mclean, R.S., X. Huang, C. Khripin, A. Jagota, and M. Zheng, *Controlled two-dimensional pattern of spontaneously aligned carbon nanotubes*. *Nano Letters*, 2006. **6**(1): p. 55-60.
91. Duggal, R., F. Hussain, and M. Pasquali, *Self - Assembly of Single - Walled Carbon Nanotubes into a Sheet by Drop Drying*. *Advanced Materials*, 2006. **18**(1): p. 29-34.
92. Shim, B.S. and N.A. Kotov, *Single-walled carbon nanotube combing during layer-by-layer assembly: from random adsorption to aligned composites*. *Langmuir*, 2005. **21**(21): p. 9381-9385.
93. Ko, H. and V.V. Tsukruk, *Liquid-crystalline processing of highly oriented carbon nanotube arrays for thin-film transistors*. *Nano Letters*, 2006. **6**(7): p. 1443-1448.
94. Whittingham, M.S., *Lithium batteries and cathode materials*. *Chemical Reviews*, 2004. **104**(10): p. 4271-4302.
95. Tarascon, J.-M. and M. Armand, *Issues and challenges facing rechargeable lithium batteries*. *Nature*, 2001. **414**(6861): p. 359-367.
96. Scrosati, B. and J. Garche, *Lithium batteries: Status, prospects and future*. *Journal of Power Sources*, 2010. **195**(9): p. 2419-2430.
97. Thackeray, M.M., C. Wolverton, and E.D. Isaacs, *Electrical energy storage for transportation—approaching the limits of, and going beyond, lithium-ion batteries*. *Energy & Environmental Science*, 2012. **5**(7): p. 7854-7863.

98. Park, C.-M., J.-H. Kim, H. Kim, and H.-J. Sohn, *Li-alloy based anode materials for Li secondary batteries*. Chemical Society Reviews, 2010. **39**(8): p. 3115-3141.
99. Zhang, X.-W., P.K. Patil, C. Wang, A.J. Appleby, F.E. Little, and D.L. Cocke, *Electrochemical performance of lithium ion battery, nano-silicon-based, disordered carbon composite anodes with different microstructures*. Journal of Power Sources, 2004. **125**(2): p. 206-213.
100. Kasavajjula, U., C. Wang, and A.J. Appleby, *Nano-and bulk-silicon-based insertion anodes for lithium-ion secondary cells*. Journal of Power Sources, 2007. **163**(2): p. 1003-1039.
101. Hwang, T.H., Y.M. Lee, B.-S. Kong, J.-S. Seo, and J.W. Choi, *Electrospun core-shell fibers for robust silicon nanoparticle-based lithium ion battery anodes*. Nano Letters, 2012. **12**(2): p. 802-807.
102. Ji, L., Z. Lin, M. Alcoutlabi, O. Toprakci, Y. Yao, G. Xu, S. Li, and X. Zhang, *Electrospun carbon nanofibers decorated with various amounts of electrochemically-inert nickel nanoparticles for use as high-performance energy storage materials*. Rsc Advances, 2012. **2**(1): p. 192-198.
103. Szczech, J.R. and S. Jin, *Nanostructured silicon for high capacity lithium battery anodes*. Energy & Environmental Science, 2011. **4**(1): p. 56-72.
104. Ruffo, R., S.S. Hong, C.K. Chan, R.A. Huggins, and Y. Cui, *Impedance analysis of silicon nanowire lithium ion battery anodes*. The Journal of Physical Chemistry C, 2009. **113**(26): p. 11390-11398.
105. Chan, C.K., H. Peng, G. Liu, K. McIlwrath, X.F. Zhang, R.A. Huggins, and Y. Cui, *High-performance lithium battery anodes using silicon nanowires*. Nature Nanotechnology, 2008. **3**(1): p. 31-35.
106. Park, M., X. Zhang, M. Chung, G.B. Less, and A.M. Sastry, *A review of conduction phenomena in Li-ion batteries*. Journal of Power Sources, 2010. **195**(24): p. 7904-7929.
107. Kaskhedikar, N.A. and J. Maier, *Lithium storage in carbon nanostructures*. Advanced Materials, 2009. **21**(25 - 26): p. 2664-2680.
108. Claye, A.S., J.E. Fischer, C.B. Huffman, A.G. Rinzler, and R.E. Smalley, *Solid - State Electrochemistry of the Li Single Wall Carbon Nanotube System*. Journal of the Electrochemical Society, 2000. **147**(8): p. 2845-2852.
109. Raffaele, R., B. Landi, J. Harris, S. Bailey, and A. Hepp, *Carbon nanotubes for power applications*. Materials Science and Engineering: B, 2005. **116**(3): p. 233-243.

110. Ng, S.H., J. Wang, D. Wexler, K. Konstantinov, Z.P. Guo, and H.K. Liu, *Highly Reversible Lithium Storage in Spheroidal Carbon - Coated Silicon Nanocomposites as Anodes for Lithium - Ion Batteries*. *Angewandte Chemie International Edition*, 2006. **45**(41): p. 6896-6899.
111. Hu, Y.S., R. Demir - Cakan, M.M. Titirici, J.O. Müller, R. Schlögl, M. Antonietti, and J. Maier, *Superior Storage Performance of a Si@ SiO<sub>x</sub>/C Nanocomposite as Anode Material for Lithium - Ion Batteries*. *Angewandte Chemie International Edition*, 2008. **47**(9): p. 1645-1649.
112. Yin, Y.-X., S. Xin, L.-J. Wan, C.-J. Li, and Y.-G. Guo, *Electrospray synthesis of silicon/carbon nanoporous microspheres as improved anode materials for lithium-ion batteries*. *The Journal of Physical Chemistry C*, 2011. **115**(29): p. 14148-14154.
113. Verma, P., P. Maire, and P. Novák, *A review of the features and analyses of the solid electrolyte interphase in Li-ion batteries*. *Electrochimica Acta*, 2010. **55**(22): p. 6332-6341.
114. Zhang, T., J. Gao, L. Fu, L. Yang, Y. Wu, and H. Wu, *Natural graphite coated by Si nanoparticles as anode materials for lithium ion batteries*. *Journal of Materials Chemistry*, 2007. **17**(13): p. 1321-1325.
115. Cakan, R., *Hydrothermal carbon spheres containing silicon nanoparticles: synthesis and lithium storage performance*. *Chemical Communications*, 2008(32): p. 3759-3761.
116. Wang, G., J. Ahn, J. Yao, S. Bewlay, and H. Liu, *Nanostructured Si-C composite anodes for lithium-ion batteries*. *Electrochemistry Communications*, 2004. **6**(7): p. 689-692.
117. Ji, L., Z. Lin, M. Alcoutlabi, and X. Zhang, *Recent developments in nanostructured anode materials for rechargeable lithium-ion batteries*. *Energy & Environmental Science*, 2011. **4**(8): p. 2682-2699.
118. Li, Y., B. Guo, L. Ji, Z. Lin, G. Xu, Y. Liang, S. Zhang, O. Toprakci, Y. Hu, and M. Alcoutlabi, *Structure control and performance improvement of carbon nanofibers containing a dispersion of silicon nanoparticles for energy storage*. *Carbon*, 2013. **51**: p. 185-194.
119. Xue, L., K. Fu, Y. Li, G. Xu, Y. Lu, S. Zhang, O. Toprakci, and X. Zhang, *Si/C composite nanofibers with stable electric conductive network for use as durable lithium-ion battery anode*. *Nano Energy*, 2013. **2**(3): p. 361-367.

120. Kim, Y.S., K.W. Kim, D. Cho, N.S. Hansen, J. Lee, and Y.L. Joo, *Silicon - Rich Carbon Hybrid Nanofibers from Water - Based Spinning: The Synergy Between Silicon and Carbon for Li - ion Battery Anode Application*. Chem Electro Chem, 2014. 1(1): p. 220-226.
121. Deng, D. and J.Y. Lee, *One-step synthesis of polycrystalline carbon nanofibers with periodic dome-shaped interiors and their reversible lithium-ion storage properties*. Chemistry of Materials, 2007. 19(17): p. 4198-4204.
122. Wang, W., M.K. Datta, and P.N. Kumta, *Silicon-based composite anodes for Li-ion rechargeable batteries*. Journal of Materials Chemistry, 2007. 17(30): p. 3229-3237.
123. Ji, L. and X. Zhang, *Fabrication of porous carbon nanofibers and their application as anode materials for rechargeable lithium-ion batteries*. Nanotechnology, 2009. 20(15): p. 155705.
124. Liu, H., C.-Y. Cao, F.-F. Wei, Y. Jiang, Y.-B. Sun, P.-P. Huang, and W.-G. Song, *Fabrication of macroporous/mesoporous carbon nanofiber using CaCO<sub>3</sub> nanoparticles as dual purpose template and its application as catalyst support*. The Journal of Physical Chemistry C, 2013. 117(41): p. 21426-21432.
125. Nan, D., J.-G. Wang, Z.-H. Huang, L. Wang, W. Shen, and F. Kang, *Highly porous carbon nanofibers from electrospun polyimide/SiO<sub>2</sub> hybrids as an improved anode for lithium-ion batteries*. Electrochemistry Communications, 2013. 34: p. 52-55.
126. Tran, C. and V. Kalra, *Fabrication of porous carbon nanofibers with adjustable pore sizes as electrodes for supercapacitors*. Journal of Power Sources, 2013. 235: p. 289-296.
127. Zhang, X., L. Ji, O. Toprakci, Y. Liang, and M. Alcoutlabi, *Electrospun nanofiber-based anodes, cathodes, and separators for advanced lithium-ion batteries*. Polymer Reviews, 2011. 51(3): p. 239-264.
128. Teki, R., M.K. Datta, R. Krishnan, T.C. Parker, T.M. Lu, P.N. Kumta, and N. Koratkar, *Nanostructured silicon anodes for lithium ion rechargeable batteries*. Small, 2009. 5(20): p. 2236-2242.
129. Ji, L., Z. Lin, A.J. Medford, and X. Zhang, *Porous carbon nanofibers from electrospun polyacrylonitrile/SiO<sub>2</sub> composites as an energy storage material*. Carbon, 2009. 47(14): p. 3346-3354.
130. Ji, L. and X. Zhang, *Manganese oxide nanoparticle-loaded porous carbon nanofibers as anode materials for high-performance lithium-ion batteries*. Electrochemistry Communications, 2009. 11(4): p. 795-798.

131. Wu, H. and Y. Cui, *Designing nanostructured Si anodes for high energy lithium ion batteries*. Nano Today, 2012. 7(5): p. 414-429.
132. Wu, X.F., A. Rahman, Z. Zhou, D.D. Pelot, S. Sinha - Ray, B. Chen, S. Payne, and A.L. Yarin, *Electrospinning core - shell nanofibers for interfacial toughening and self - healing of carbon - fiber/epoxy composites*. Journal of Applied Polymer Science, 2013. 129(3): p. 1383-1393.
133. Wu, H., G. Chan, J.W. Choi, Y. Yao, M.T. McDowell, S.W. Lee, A. Jackson, Y. Yang, L. Hu, and Y. Cui, *Stable cycling of double-walled silicon nanotube battery anodes through solid-electrolyte interphase control*. Nature Nanotechnology, 2012. 7(5): p. 310-315.
134. Ji, L. and X. Zhang, *Evaluation of Si/carbon composite nanofiber-based insertion anodes for new-generation rechargeable lithium-ion batteries*. Energy & Environmental Science, 2010. 3(1): p. 124-129.
135. Ji, L. and X. Zhang, *Electrospun carbon nanofibers containing silicon particles as an energy-storage medium*. Carbon, 2009. 47(14): p. 3219-3226.
136. Chang, G. and J. Shen, *Fabrication of Microropes via Bi - electrospinning with a Rotating Needle Collector*. Macromolecular Rapid Communications, 2010. 31(24): p. 2151-2154.
137. Ji, L., K.-H. Jung, A.J. Medford, and X. Zhang, *Electrospun polyacrylonitrile fibers with dispersed Si nanoparticles and their electrochemical behaviors after carbonization*. Journal of Materials Chemistry, 2009. 19(28): p. 4992-4997.
138. Yao, H., G. Zheng, W. Li, M.T. McDowell, Z. Seh, N. Liu, Z. Lu, and Y. Cui, *Crab shells as sustainable templates from nature for nanostructured battery electrodes*. Nano Letters, 2013. 13(7): p. 3385-3390.
139. Peresin, M.S., Y. Habibi, J.O. Zoppe, J.J. Pawlak, and O.J. Rojas, *Nanofiber composites of polyvinyl alcohol and cellulose nanocrystals: manufacture and characterization*. Biomacromolecules, 2010. 11(3): p. 674-681.
140. Liang, Y., L. Ji, B. Guo, Z. Lin, Y. Yao, Y. Li, M. Alcoutlabi, Y. Qiu, and X. Zhang, *Preparation and electrochemical characterization of ionic-conducting lithium lanthanum titanate oxide/polyacrylonitrile submicron composite fiber-based lithium-ion battery separators*. Journal of Power Sources, 2011. 196(1): p. 436-441.
141. Jung, H.-R., D.-H. Ju, W.-J. Lee, X. Zhang, and R. Kotek, *Electrospun hydrophilic fumed silica/polyacrylonitrile nanofiber-based composite electrolyte membranes*. Electrochimica Acta, 2009. 54(13): p. 3630-3637.

142. Kovalenko, I., B. Zdyrko, A. Magasinski, B. Hertzberg, Z. Milicev, R. Burtovyy, I. Luzinov, and G. Yushin, *A major constituent of brown algae for use in high-capacity Li-ion batteries*. *Science*, 2011. **334**(6052): p. 75-79.
143. Rahaman, M., A.F. Ismail, and A. Mustafa, *A review of heat treatment on polyacrylonitrile fiber*. *Polymer Degradation and Stability*, 2007. **92**(8): p. 1421-1432.
144. Stern, E., R. Wagner, F.J. Sigworth, R. Breaker, T.M. Fahmy, and M.A. Reed, *Importance of the Debye screening length on nanowire field effect transistor sensors*. *Nano Letters*, 2007. **7**(11): p. 3405-3409.
145. Stankovich, M.T. and A.J. Bard, *The electrochemistry of proteins and related substances part III. bovine serum albumin*. *Journal of Electroanalytical Chemistry and Interfacial Electrochemistry*, 1978. **86**(1): p. 189-199.
146. Shao, M.-W., H. Yao, M.-L. Zhang, N.-B. Wong, Y.-Y. Shan, and S.-T. Lee, *Fabrication and application of long strands of silicon nanowires as sensors for bovine serum albumin detection*. *Applied Physics Letters*, 2005. **87**(18): p. 3106.
147. Nakajima, A., K. Hashimoto, T. Watanabe, K. Takai, G. Yamauchi, and A. Fujishima, *Transparent superhydrophobic thin films with self-cleaning properties*. *Langmuir*, 2000. **16**(17): p. 7044-7047.
148. Zhu, D., C. Xu, N. Nakura, and M. Matsuo, *Study of carbon films from PAN/VGCF composites by gelation/crystallization from solution*. *Carbon*, 2002. **40**(3): p. 363-373.
149. Wu, H., G. Zheng, N. Liu, T.J. Carney, Y. Yang, and Y. Cui, *Engineering empty space between Si nanoparticles for lithium-ion battery anodes*. *Nano Letters*, 2012. **12**(2): p. 904-909.
150. Lee, J.K., K.W. An, J.B. Ju, B.W. Cho, W.I. Cho, D. Park, and K.S. Yun, *Electrochemical properties of PAN-based carbon fibers as anodes for rechargeable lithium ion batteries*. *Carbon*, 2001. **39**(9): p. 1299-1305.
151. Obrovac, M. and L. Krause, *Reversible cycling of crystalline silicon powder*. *Journal of The Electrochemical Society*, 2007. **154**(2): p. A103-A108.
152. Hatchard, T. and J. Dahn, *In situ XRD and electrochemical study of the reaction of lithium with amorphous silicon*. *Journal of The Electrochemical Society*, 2004. **151**(6): p. A838-A842.
153. Wu, Y., M. Reddy, B. Chowdari, and S. Ramakrishna, *Long-term cycling studies on electrospun carbon nanofibers as anode material for lithium ion batteries*. *ACS Applied Materials & Interfaces*, 2013. **5**(22): p. 12175-12184.

154. Kim, C., K.S. Yang, M. Kojima, K. Yoshida, Y.J. Kim, Y.A. Kim, and M. Endo, *Fabrication of Electrospinning - Derived Carbon Nanofiber Webs for the Anode Material of Lithium - Ion Secondary Batteries*. *Advanced Functional Materials*, 2006. **16**(18): p. 2393-2397.
155. Qiao, L., X. Sun, Z. Yang, X. Wang, Q. Wang, and D. He, *Network structures of fullerene-like carbon core/nano-crystalline silicon shell nanofibers as anode material for lithium-ion batteries*. *Carbon*, 2013. **54**: p. 29-35.
156. Cheng, F., Z. Tao, J. Liang, and J. Chen, *Template-Directed Materials for Rechargeable Lithium-Ion Batteries†*. *Chemistry of Materials*, 2007. **20**(3): p. 667-681.
157. Lee, K.T., J.C. Lytle, N.S. Ergang, S.M. Oh, and A. Stein, *Synthesis and Rate Performance of Monolithic Macroporous Carbon Electrodes for Lithium - Ion Secondary Batteries*. *Advanced Functional Materials*, 2005. **15**(4): p. 547-556.
158. Zeng, C., X. Han, L.J. Lee, K.W. Koelling, and D.L. Tomasko, *Polymer-clay nanocomposite foams prepared using carbon dioxide*. *Advanced Materials*, 2003. **15**(20): p. 1743-1747.
159. Tomasko, D.L., H. Li, D. Liu, X. Han, M.J. Wingert, L.J. Lee, and K.W. Koelling, *A review of CO2 applications in the processing of polymers*. *Industrial & Engineering Chemistry Research*, 2003. **42**(25): p. 6431-6456.
160. Yao, Y., M.T. McDowell, I. Ryu, H. Wu, N. Liu, L. Hu, W.D. Nix, and Y. Cui, *Interconnected silicon hollow nanospheres for lithium-ion battery anodes with long cycle life*. *Nano Letters*, 2011. **11**(7): p. 2949-2954.
161. Wanekaya, A.K., W. Chen, N.V. Myung, and A. Mulchandani, *Nanowire-based electrochemical biosensors*. *ELECTROANALYSIS-WEINHEIM-*, 2006. **18**(6): p. 533.